Molten Salt Thermophysical Properties Characterization: Understanding the Mechanisms of Structural Formation in Halide Salts for Molten Salt Advanced Nuclear Reactor Fuel Qualification & Safety

by

Nathanael Gardner

A dissertation submitted in partial satisfaction of the

requirements for the degree of

Doctor of Philosophy

in

Nuclear Engineering

in the

Graduate Division

of the

University of California, Berkeley

Committee in charge:

Professor Raluca O. Scarlat, Chair
Professor Mark Asta,
Professor Massimiliano Fratoni,
Professor Peter Hosemann,

Spring 2026

ABSTRACT

Molten Salt Thermophysical Properties Characterization: Understanding the Mechanisms of Structural Formation in Halide Salts for Molten Salt Advanced Nuclear Reactor Fuel Qualification & Safety

By

Nathanael Gardner

Doctor of Philosophy in Nuclear Engineering

University of California, Berkeley

Professor Raluca O. Scarlat, Chair

Molten actinide containing halide salts are used to fuel molten salt nuclear reactors. Before these reactors can be deployed, it is necessary to characterize the thermophysical properties of these fuel salts for fuel qualification, licensing, and technological applications on the front end (supply chain), reactor operations (maintenance), and back end (end of life) of their fuel cycles. To connect experimental property measurements to simulation and thermodynamic predictions, it is also necessary to understand the mechanisms behind this thermophysical property behavior. In this dissertation, internal structure is used to understand macroscopic properties to better understand how occurrences in a fuel system may affect reactor behavior.

Activation energy of viscosity in halide molten salts is shown to scale with increasing concentration of strong complex-forming cation species. This amount by which this parameter scales is dependent on the degree of polymerization and coordination number, which in turn depend on oxidation state of each species, of each complex-forming cation and resulting size of the oligomeric species present. This behavior is demonstrated in beryllium and uranium containing fluoride and chloride fuel and heat transfer salts. Coordination number and network formation are used to predict the viscosity behavior of a molten chloride fuel salt system at an equilibrium state in the reactor with fission and transmutation products present.

Ideal thermal expansivity, calculated through molar volume additivity, is shown to be better fitted by a linear density assumption rather than a linear molar volume assumption. For fuel salt systems containing uranium fluoride or chloride, the redox potential of the salt, and thus the U^{3+}/U^{4+} ratio can affect the measured density. This sensitivity is demonstrated through ideal density trend calculation of NaCl-UCl_3 and NaCl-UCl_4 melts.

Similar to observations of the Molten Salt Reactor Experiment fuel salt, FLiBe is measured to have a ~3% volume shrinkage upon freezing. Imaging of solid FLiBe also revealed strong preferred orientation in its internal structure of its unit cell axes. This results in anisotropy and directionally varied strain during thermal expansion.

The molten salt characterization in this work reports new data regarding the properties of fuel and heat transfer salts for advanced molten salt reactor fuel qualification and operation. The thermophysical property uncertainty propagation calculated as well as the sensitivity analysis of fuel salt properties provides information for nuclear reactor safety systems and parameters such as freeze valves and tolerance ranges. The fundamental science exploration of the structural mechanisms of molten salt thermophysical properties deepens the understanding of molten salt behavior and provides validation data for simulated predictions.

I. TABLE OF CONTENTS

II. TABLE OF FIGURES

III. TABLE OF TABLES

IV. ACRONYMS AND ABBREVIATIONS

FLiBe: Li2BeF4

FHR: Fluoride Salt-Cooled High Temperature Reactor

MSR: Molten Salt Reactor

BNL: Brookhaven National Laboratory

ORNL: Oak Ridge National Laboratory

LANL: Los Alamos National Laboratory

CIF: Crystallographic Information File

VESTA: Visualization for Electronic and Structural Analysis

ICSD: Inorganic Crystal Cell Database

NOMAD: Nanoscale-Ordered Materials Diffractometer

HIPPO: High-Pressure Preferred Orientation

SNS: Spallation Neutron Source

GSAS: General Structure Analysis System

AIMD: Ab-Initio Molecular Dynamics

LANSCE: Los Alamos Neutron Science Center

PDF: Pair Distribution Function

NSLS-II: National Synchrotron Light Source II

MD: Molecular Dynamics

MSRE: Molten Salt Reactor Experiment

MRD: Multiples of random density

f(T): lattice parameter a, b, or c or unit cell volume V, written as a function of temperature to describe thermal expansion behavior

f0: lattice parameter a, b, c or unit cell volume V at T0

T0: 293 K, room temperature

αf: linear coefficient of thermal expansion term

βf : quadratic coefficient of thermal expansion term

ρsolid : density of solid

c/a ratio: ratio of the c to a lattice parameters,

pdf: Pair Distribution Function

S(q): Structure Factor

AIMD: ab-initio molecular dynamics

MAUD: Materials Analysis Using Diffraction

ODF: orientation distribution function

MSR: molten salt reactor

GEN-IV: Generation IV

FHR: Fluoride Salt-Cooled High-Temperature Reactor

MCFR: Molten Chloride Fast Reactors

MCRE: Molten Chloride Reactor Experiment

ICP-OES: Inductively Coupled Plasma-Optical Emission Spectroscopy

ICP-MS: Inductively Coupled Plasma- Mass Spectroscopy

TC: thermocouple

MCR: Modular Compact Rheometer

DSC: differential scanning calorimeter

TGA: thermogravimetric analysis

V. VARIABLES

V: Unit Cell Volume

a, c: lattice parameters

$\boldsymbol{\beta}_f$: quadratic thermal expansion coefficient

$\boldsymbol{\alpha}_f$: linear thermal expansion coefficient

ρ: density

γ: shear rate

τ: shear stress

μ: dynamic viscosity

ν: kinematic viscosity

ΔM: mass difference

G^I: Storage Modulus

G^{II}: Loss Modulus

G: Complex Modulus

τ: Shear Stress

γ: Shear Strain

$\dot{\gamma}$: Shear Rate

μ: Dynamic Viscosity

tan (δ): Loss factor

τ_A: Shear Stress Amplitude

γ_A: Strain Amplitude

VI. ACKNOWLEDGEMENTS

Thank you to the Reactor Safety and Inorganic Chemistry of Light Elements and Other Critical Minerals at High Temperature (SALT) Research Group for creating a positive learning and researching environment; Haley Williams, Michael Borrello, Sasha Kennedy, Ryan Hayes, Timothy Pickarski, Maksim Pecherskiy, Lorenzo Vergari, David Park, Yusuf Shehata, Sarah Heagy, Chirstian Sclafani, Nicole Johnson, Momoka Imoto, Louis Pointreau, Maximilien Denis, Sander Ratso, and Randall Chiu.

Thank you to Raluca Scarlat, my principal investigator, for helping me to become an independent researcher. I appreciate you taking a chance on a chemical engineer with no nuclear background, and for dealing with all the issues that we find/create in the lab.

Thank you to my undergraduate researchers who have helped me to become a better research mentor; Tatiana Lindahl, Zachary Falkowski, Gabriel Holesinger, Qiye Hu, Marilyn Li, and Augustina Jolly.

Thank you to my national laboratory collaborators and mentors: from Los Alamos National Laboratory, Sven Vogel and Marisa Monreal; from Oak Ridge National Laboratory Joerg Neuefeind and Michelle Everette; from Brookhaven National Laboratory Dan Olds. And to the national laboratory user facilities including the HIPPO beamline at LANSCE at Los Alamos National Laboratory, and the NOMAD beamline at SNS at Oak Ridge National Laboratory.

Thank you to my university collaborators Sean Fayfar, Andrea Hwang, Shivani Shrivastava, Boris Khaykovich, and David Sprouster. And to my committee members Mark Asta, Massimiliano Fratoni, and Peter Hoseman.

Thank you to the radiation safety officers at UC Berkeley who have worked with me to safely complete this actinide salt work in a beryllium lab; Dan Hibbing, Phil Broughton, Alan Bolind, and Ian Baldridge

Thank you to the members of the UC Berkeley Graduate Division, Martha Chavez, and Sarah Acosta, and from the UC Berkeley College of Engineering, Meltem Erol.

Thank you to the my funding sources, including DOE-NE UNLP Fellowship, the NSF-GRFP Fellowship, and the GEM Fellowship, and my projects, including the Hellman Fellows Fund, the Speciation of Light Elements at High Temperatures NEUP, and the Bridging the gap between experiments and modeling to improve the design of molten salt reactors IRP for funding me and my research.

Thank you to my Berkeley friends (Jacob, Mahek, Nya, Ja'Nya, Alexandra, Michael, Minerva, Sumukhi, James, Salim, Chad), Facetime friends (Kyle, Angie, Ngozi, Ammad, Jenna, Kiera, Patricia, Sharina), nuclear brothers (Grey and Rasheed), family (Ms. Mariem Abadir ❤️‍🩹, Saraniesha, Isaac, Arianna, Mom, and Dad), and organizations (BGESS, Aunties & Uncs IM Basketball championship team, Dissertation Writing Group) that have been around to motivate me during my PhD.

Thank you to LC Tech and Anton Paar for teaching me patience and for helping me to develop my problem-solving skills.

Finally, thank you to God for everything.

VII. CURRICULUM VITAE

David "Nathanael" Gardner ORCID: 0000-0001-8780-6004 Email: Nathanael_gardner@berkeley.edu

Career Objective: A career in the area of research, development, safety, licensing, and operation of advanced nuclear reactor fuel systems.

Education

2021-Present: PhD Candidate Nuclear Engineering, *University of California Berkeley*

2021: B.S. Chemical Engineering, Summa Cum Laude, *Howard University*

Awards

- GEM Fellowship 2021
- Nuclear Energy University Programs UNLP Fellowship 2022
- National Science Foundation GRFP Fellowship 2022
- 2024-2025 Stanley Prussin Award for High Achieving Nuclear Engineering Graduate Student
- 2025 UC Berkeley Nuclear Engineering Best Paper Award: Chemistry

Research Experience

SALT Research Group-UC Berkeley (August 2021- Present)

- Measure the thermophysical and structural properties of beryllium, uranium, and fission product containing molten fluoride and chloride salts for applications in nuclear reactor technology.
- Conduct high temperature experimentation and post-experiment data analysis to determine values and uncertainty of melting point, density, and viscosity for molten salts. Utilize SEM and optical microscopy to analyze nuclear materials including metal alloys, metallic uranium, TRISO particles, frozen salt, and graphite powder.
- Lead experimental testing portion of two 3-million-dollar DOE-NE research projects. Manage multiple private nuclear company, national laboratory, and university collaborations. Prepare and give research presentations to technical and non-technical government, academic, and industrial audiences. Design and review experimental test plans.
- Author technical quarterly reports and papers for the DOE, industry, national laboratory, and university collaborators, and technical journals. Assist with funding and experimental user facility proposal writing. Authored 2 funded proposals with the NSF and the DOE-NE.
- Perform laboratory manager duties including mentoring researchers, performing monthly radiation and beryllium surveys, procuring supplies and equipment, and safety training. Maintain and repair laboratory instruments, gloveboxes, and pressurized gas lines.

Los Alamos National Laboratory (May 2023-August 2023)

- Performed 3 neutron and 1 X-ray diffraction experiments with national lab collaborators on solid salt samples to extract the coefficient of thermal expansion for molten salt reactor coolant applications and published manuscript on findings.

The Boeing Company Research and Technology Intern (May 2020-August 2020)

- Created catalog of corrosion prevention methods and materials for the 747, 767, and 777 freighters through plant and laboratory research. Evaluated fuselage coatings for the 787 Dreamliner and optimized coating selection method to increase manufacturing efficiency.

Leadership and Outreach Experience

University of California Berkeley Graduate Division (June 2022-June 2025)

- Organize prospective graduate student visit days for over 400 students to improve university

recruitment and retention. Traveled to prospective graduate students at 4 Lead workshop series for over 200 undergraduate students on preparing for and applying to graduate school.

Expanding Your Horizons (2024)

- Designed and hosted a hands-on nuclear energy summer school session for elementary and middle schoolers, by conducting public experiments demonstrating fission, salt chemistry, and radiation detection

Teaching and Mentorship

Undergraduate and Research Mentoring (August 2021-Present)

- G. Holesinger (UCB Ne ’23) Viscosity studies in beryllium fuel salts
- J. Xu (UCB NE ’24) Machining of components for FLiBe density measurements
- T. Lindahl (UCB ChemE ’27) Viscosity of actinide containing chloride molten salts
- Z. Falkowski (UCB Chem ’23) Calorimetry of actinide containing molten salts
- Q. Hu (UCSB ChemE ’23) Cell design for graphite oxidation experiments
- M. Li (UCB ChE ’27) Sensitivity of chloride nuclear fuel salt viscosity to fission products
- Jolly (UCB NE ’26) Sensitivity of chloride nuclear fuel salt density to fission products

UC Berkeley IE Summer Research Experience (May 2024-August 2024)

- Designed and Directed summer research program for 20 visiting undergraduate students. Taught classes on the graduate school application process, conducting research, writing research statements, giving research presentations, and technical writing. Organized an end-of-summer technical talk session for students to present their research results.

SALT Research Group Undergraduate Research Coordinator (June 2024-June 2025)

- Taught seminar for class Nuclear Engineering-199. Assisted in all aspects of SALT research group undergraduate student research including student recruiting, research mentor and project placement, and final report and presentation review.

Publications

- “Safety Analysis on Fission Induced Thermophysical Property Alterations of MCFR Fuel Salt.” **D. Nathanael Gardner** *et al,* ANS Winter Conference Paper 2025. ans.org/pubs/transactions/article-59827/
- “Molten salt fuels and coolants for Molten Chloride Fast Nuclear Reactors (MCFR): density, viscosity, and melting point of NaCl binaries with KCl, MgCl2, and UCl3.” **D. Nathanael Gardner**, *et al* ACS Journal of Chemical & Engineering Data (In Review)
- “Round Robin Measurements of Molten Salt Properties for LiF-NaF-KF (FLiNaK) and NaCl-KCl Mixtures.” T. Munro, R. Chiu, M. Rose, O. Benes, M. Boca, **D. Nathanael Gardner**, *et al* Journal of Chemical Engineering Data 2025 10.1021/acs.jced.5c00421
- “The Effect of Complex Forming Cations on the Thermophysical Properties of Beryllium and Uranium Fluoride Salts for Nuclear Reactor Applications.” **D. Nathanael Gardner**, *et al* ACS Physical Chemistry Au 2025 10.1021/acsphyschemau.5c00043
- “Solid structure of Li2BeF4 (FLiBe) from room temperature to melting studied by neutron and X-ray diffraction.” **D. Nathanael Gardner,** et al. Journal of Applied Crystallography 2025. 10.1107/S1600576725000548
- “Complex Structure of Molten FLiBe ($2LiF\text{-}BeF_2$) Examined by Experimental Neutron Scattering, X-Ray Scattering, and Deep-Neural-Network Based Molecular Dynamics.” S. Fayfar, R. Chahal, H. Williams, **D. Nathanael Gardner,** *et al* PRX Energy 2024. 10.1103/PRXEnergy.3.013001

- "Sources of Error in the Measurement of Thermophysical Properties of Molten Salts", **D. Nathanael Gardner** *et al,* ANS Winter Conference Paper 2023. ans.org/meetings/wm2023/session/view-2097/#paper_5943
- "Probing Speciation of Light Elements in Molten Salts by Electrochemistry, High Temperature Liquid NMR, and Neutron Diffraction." Haley Williams, **D. Nathanael Gardner**, et al. 2022 ANS Annual Meeting. doi.org/10.13182/T126-38488

Conference Presentations

- D. Nathanael Gardner, *Yusuf Shehata (Speaker)*, *et al*, "Molten Chloride Fast Reactor Fuel Salt Redox Potential at Equilibrium." The Minerals, Metals, and Materials Conference. San Diego, CA. March 2026
- D. Nathanael Gardner, *et al*, "Safety Analysis on Fission Induced Thermophysical Property Alterations of MCFR Fuel Salt." American Nuclear Society Winter Conference. Washington, DC. November 2025
- D. Nathanael Gardner, Raluca O. Scarlat, "Effect of fission products on the thermophysical properties of actinide containing chloride fuel salts." American Chemical Society. Washington, DC. August 2025
- D. Nathanael Gardner, "Thermophysical Property Measurement of Molten Salts." Poster, American Institute of Chemical Engineers Annual Meeting. San Diego, CA. October 2024
- D. Nathanael Gardner, *et al*, "Thermophysical Property Measurement of Uranium Containing Fluoride and Chloride Salts." American Institute of Chemical Engineers Annual Meeting. San Diego, CA. October 2024
- D. Nathanael Gardner *et al*, "Sources of Uncertainty in Thermophysical Properties Measurement." American Nuclear Society Winter. Washington, DC. November 2023
- D. Nathanael Gardner *et al*, "Thermophysical Properties of Actinide Containing Molten Salts." Materials in Nuclear Energy Systems. New Orleans, LA. December 2023
- D. Nathanael Gardner *et al*, "Solute Effects on Solid Li_2BeF_4 (FLiBe) Thermal Expansion." American Chemical Society. San Francisco, CA. August 2023
- D. Nathanael Gardner, *et al*, "FLiBe Thermodynamic and Physical Properties Validation." The Minerals, Metals, and Materials Conference. San Diego, CA. March 2023
- D. Nathanael Gardner *et al*, "Probing Speciation of Light Elements in Molten Salts by Electrochemistry, High Temperature Liquid NMR, and Neutron Diffraction." Molten Salt NEUP PI Meeting. Chicago, IL. April 2023
- Haley Williams, D. Nathanael Gardner, *et al* "Probing Speciation of Light Elements in Molten Salts by Electrochemistry, High Temperature Liquid NMR, and Neutron Diffraction. American Nuclear Society. Anaheim, CA. June 2022

Relevant Skills

- **Software:** ChemDraw, GnuPlot, OlexSys, MAUD, VESTA, MATLAB, OriginPro
- **Laboratory:** Rheology, UV-Vis, Neutron/X-ray Diffraction, SEM, Optical Microscopy
- **Miscellaneous:** Data analysis, Beryllium & Radiation Safety, Nuclear Technology
- **Hazardous Materials:** Depleted Uranium, Beryllium, Irradiated graphite, Neutron activated samples, High temperature, High pressure

Organizations

- American Chemical Society Member (2023-Present)
- American Nuclear Society Member (2022 – Present)
- BGESS Financial Chair (2022 - Present)

1 INTRODUCTION TO MOLTEN FUEL SALT UTILIZATION

With rising world energy needs, the necessity of the development of nuclear energy as economic and resilient energy source is evident. To address this, the International Generation IV Initiative Forum was established in 2000 to research and develop novel advanced nuclear reactor systems with an emphasis on safety, non-proliferation, economic feasibility, fuel efficiency, and waste management[1], [2], [3], [4]. This agreement signed by the United States, Canada, China, the European Atomic Energy Community, France, Japan, South Korea, Switzerland identified six advanced nuclear reactor technologies including the Sodium-Cooled Fast Reactor (SFR), the Supercritical-Water-Cooled Reactor (SCWR), the Gas-Cooled Fast Reactor (GFR), the Lead-Cooled Fast Reactor (LFR), the Very-High Temperature Reactor (VHTR), and finally the Molten Salt Reactor (MSR) [1], [2], [3], [4].

Molten salt reactors (MSR) can either be solid fueled, where the molten salt is used as a heat transfer fluid, or utilize the salt as an actinide fuel solvent as in liquid fueled reactors[5]. In solid fueled reactors such as Kairos Powers Fluoride Salt-Cooled High-Temperature Reactor (FHR), solid uranium fuel is contained in Tri-structural ISOtropic (TRISO) particle fuel pellets, preventing the majority of fission products from speciating in the circulating molten salt[6]. However in liquid fueled designs such as TerraPower's NaCl-UCl_3, ThorCon Power's NaF-BeF_2-UF_4-ZrF_4, FLiBe Energy's LiF-BeF-UF_4, Natura Resources's LiF-BeF-UF_4 fueled molten salt reactors, as the fissile material is dissolved in the the molten salt, fission products across the periodic table can potentially be present in the molten salt[7]. During burnup, these soluble and insoluble fission products accumulate in the reactor potentially resulting in negative effects on the reactor behavior including but not limited to pipe fouling due to plating out of insoluble material, thermophysical property alterations due to structural or colloidal particle effects from soluble and insoluble fission products, inaccurate calculated source term predictions, and corrosion due to shifting the redox potential[8], [9], [10], [11]. Concurrently, due to the burnup of the fissile material inside of the molten salt during the natural operation of these reactors, the molar concentration of uranium in the melt shifts as well[8].

Therefore, it is vital to the operation, design, and licensing of molten salt nuclear fission reactors to understand the mechanisms behind the thermophysical properties of molten halide fuel salt components, fission, and transmutation products and how their respective mechanisms impact their relative contribution to the melt's behavior. By understanding the mechanisms impacting properties such as viscosity, density, and thermal expansivity, this work will allow for the grouping of salt components and solutes by characteristics for better prediction of fuel behaviors. To understand how molten fuel salt thermophysical properties change over the course of reactor operation due to the shift in fuel salt composition and the accumulation of fission product salt solutes for reactor design, operation, and licensing applications, this works seeks to understand the ways in which internal salt structure is tied to properties through three components; each examining a structural aspect of advanced reactor fuel and heat transfer salts.

1.1 Background & Motivation

Research on the potential of molten salt reactors began in the mid-20th century with the Aircraft Reactor Experiment (ARE), which utilized a molten fluoride based fuel salt containing NaF, ZrF_4, and UF_4 and beryllium oxide moderators[12], [13]. The potential of molten salt was further explored at Oak Ridge National Laboratory (ORNL) in the 1960's during the Molten Salt Reactor Experiment (MSRE)[13]. This reactor design consisted of a lithium 7 enriched ^{7}LiF-BeF_2-ZrF_4-UF_4 (65.0-29.1-5.0-0.9) fuel salt and ^{7}LiF-BeF_2 (66-34) secondary coolant salt[14]. Research and development into molten fuel salt technology continued into the 21st century. In the 2020's, similar to the MSRE, the Molten Chloride Reactor Experiment (MCRE), a collaboration between TerraPower, Southern Company, and Idaho National Laboratory (INL), is a currently ongoing research project testing the feasibility of a fast spectrum NaCl-UCl_3 fueled molten salt reactor[15]. Another 2020's molten salt research collaboration between Natura Resources and Abilene Christian University as well as Georgia Institute of Technology, Texas A&M

University, and the University of Texas has resulted in the Natura-MSR-1, an advanced university test molten salt reactor fueled by LiF-BeF_2-UF_4 and cooled by LiF-BeF_2. Additionally, Thorcon Power U.S. and Thorcon Power Indonesia are currently designing a shipyard built molten salt reactor that can be deployed to areas of need, fueled by NaF-BeF_2-UF_4-ZrF_4 and cooled by NaF-BeF_2. An image of the fuel salt can be seen in Figure 1.

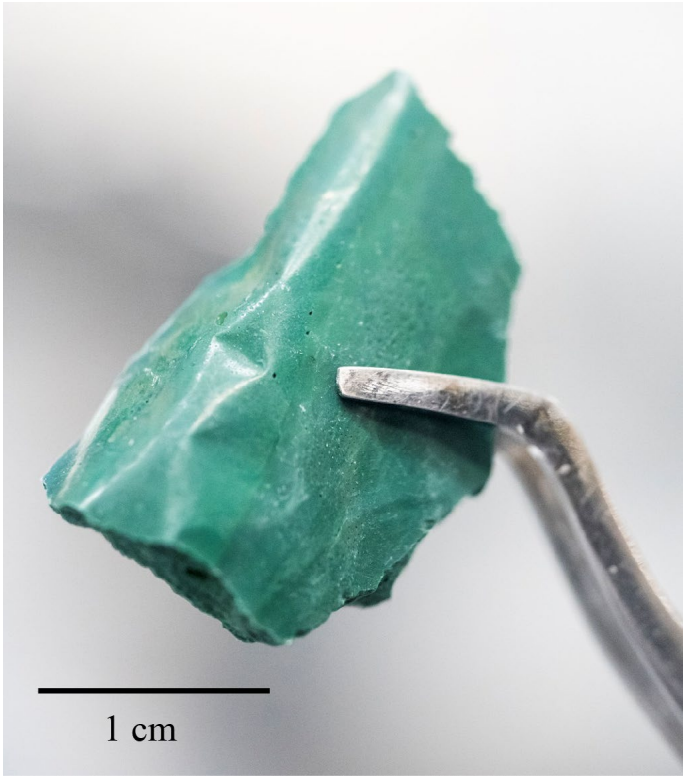

Figure 1. Frozen shard of NaF-BeF_2-UF_4-ZrF_4 (UZrFNaBe) salt used by ThorCon Power and provided by the Nuclear Materials and Fuel Cycle Center at Virginia Tech, held by tweezers for imaging inside of an Argon glovebox.

For the successful commercial deployment of these molten salt reactor designs, multiple liquid fuel qualification, licensing, and technological questions on the front end (supply chain), reactor operations (maintenance), and back end (end of life) of the fuel cycle require answers[10], [16], [17], [18]. Specific topics requiring further study for the qualification and deployment of molten salt reactor fuel systems include [10], [16], [17]

- Fission product solubility, speciation, and removal
- Thermophysical property sensitivity to composition, temperature, and redox
- Safeguards
- Purification
- Synthesis
- Waste management

This work focuses on the effect of thermophysical properties on nuclear molten salt reactor operation. According to the Nuclear Regulatory Commission (NRC), to qualify a nuclear fuel salt, in addition to operational functions, the salt must fulfill the fundamental safety functions (FSF's) of 1. Limiting the release of radioactive materials, 2. Removing heat from the reactor and waste stores, and 3. Controlling the reactivity[19]. Characterization of the thermophysical properties of the fuel salt (density, thermal expansivity, viscosity, melting point) is directly connected to accomplishing these functions (e.g. thermal hydraulic parameters for calculating heat removal, melting point and thermogravimetric analysis for

prediction of vaporization of fuel salt or fission product components)[19]. The NRC report NUREG/CR-7299 summarizes the significance of different thermophysical properties on fulfilling these FSF's under normal operations, anticipated operational occurrences, and design basis events.[19]. The significance ratings from this report of the properties examined in this work are detailed below[19].

- Viscosity
  - Normal Operation and Anticipated Operational occurrences: Minor importance to limiting release of radioactive materials, major importance to heat removal, negligible impact to reactivity control
  - Design Basis Events: Minor importance to limiting release of radioactive materials, major importance to heat removal, minor impact to reactivity control
- Density
  - Normal Operation and Anticipated Operational Occurrences: Minor importance to limiting release of radioactive materials, major importance to heat removal, major importance to reactivity control
  - Design Basis Events: Minor importance to limiting release of radioactive materials, major importance to heat removal, major importance to reactivity control
- Liquidus Temperature
  - Normal Operation and Anticipated Operational Occurrences: Minor importance to limiting release of radioactive materials, negligible impact to heat removal, negligible impact to reactivity control
  - Design Basis Events: Varying importance to limiting release of radioactive materials, varying importance to heat removal, negligible impact to reactivity control
- Elemental Composition
  - Normal Operation and Anticipated Operational Occurrences: Major importance to limiting release of radioactive materials, major importance to heat removal, negligible importance to reactivity control
  - Design Basis Events: Major importance to limiting release of radioactive materials, major importance to heat removal, negligible importance to reactivity control

Therefore, it is necessary to characterize fuel salt properties across temperature and composition with bounded uncertainties, and to measure how they can be altered due to normal reactor operations, transients, or accident scenarios[19]. To better connect experimental property measurements to simulation and thermodynamic prediction techniques, it is also vital to understand the mechanisms behind the thermophysical property behavior. This work seeks to connect these techniques through the measurement of solid and liquid salt internal structure and interactions.

The goal of this work is to characterize the ways in which structure in a molten actinide salt affect its thermophysical properties to then provide better understanding on how fission and transmutation product propagation solvated inside the salt can change its behavior. This goal is accomplished through three components.

The first is **1. Confirming and quantifying presence of structure in well characterized fluoroberyllate salt samples through diffraction experiments.** Starting from the solid state, neutron and X-ray diffraction methods were used to examine the structural parameters of the (Li_2BeF_4) unit cell lattice from room temperature to the melting point to measure the lattice thermal expansion and thermal strain. As temperature increased, to evaluate the structural changes during phase change, this diffraction data was then used to evaluate the change in the molar volume between the solid and liquid phases. After melting, to understand the extent to which oligomers and polymeric species are present in FLiBe, diffraction based structural studies were completed through measurement of the melt's structure factor (S(q)) and Pair Distribution Function (PDF). To determine how the changing concentration of complex forming

components in LiF-BeF_2 melts changes the length and quantity of oligomers present, increasing concentrations of BeF_2, from the nominal FLiBe composition to 100% BeF_2, were characterized using high temperature neutron diffraction, and their S(q)s and PDFs extracted.

After utilizing diffraction experiments to measure the increase in structural presence due to increasing BeF_2 content, to assess how fuel salt components affect structure, the second component consists of **2. Measuring the thermophysical properties of actinide containing fluoroberyllate salts to understand the effects of varying oligomer formation behavior of fuel salt melt components.** In this work, two NaF-BeF_2 fluoroberyllate salts are compared, one a fuel salt containing UF_4, and one a heat transfer salt containing only BeF_2 as a coordinating cation. Thermophysical properties of both salts including density, thermal expansivity, and viscosity are quantified. This chapter also evaluates trends in thermophysical properties across the compositional range of beryllium and uranium containing fluoride salts by comparing multiple ideal density calculation methods as well as plotting the activation energy of viscosity across composition to measure complex formation.

Then, to determine the relationship between structure and thermophysical properties in non-fluoride molten fuel salts, the third component is **3. Measuring the thermophysical properties of actinide and non-actinide chloride salt binaries.** In this chapter, two heat transfer NaCl based chloride salts and one depleted uranium fuel salt are characterized regarding their melting points, density, thermal expansivity, and viscosity. Sensitivity to composition to composition and redox are investigated using molar volume additivity calculations.

Each chapter of this work explains the methods and evaluates the findings of the investigation of each of these components.

2 UNDERSTANDING SOLID AND LIQUID MOLTEN SALT STRUCTURE

2.1 Chapter Summary

Molten fluoride salts such as Li_2BeF_4 (FLiBe) are used in molten salt reactors and fluoride salt cooled high temperature reactors and fusion reactors as a fuel solvent, tritium breeding medium, and coolant. In engineered systems that use molten salt, solid-state material will be present during melting and freezing scenarios, and, therefore, the temperature-dependent properties of the solid and solid/liquid phase transition merit investigation. To observe the behavior of the solid state of Li_2BeF_4 from room temperature to melting, this work used neutron and X-ray diffraction to measure the changes in the lattice parameters and volume of the crystalline unit cell and compared the results with prior low temperature data for Li_2BeF_4 solid. From neutron diffraction data it is also possible to identify anisotropy: centimeter-scaled crystals align preferentially with the a axes parallel to the direction of freezing front propagation and the c axes expand 54% more than the a axes. This work provides the lattice constants as a function of temperature, quantifies the thermal expansion, and determines the equation describing the change in density for solid Li_2BeF_4 from room temperature to 459 °C to be $\rho_{solid}[kg/m^3]=2184.8(4)-0.115(2)T$ [°C] and the volume expansion upon melting to be 3.8(4)% at 459 °C and 2.9(4)% if supercooling at 400 °C.

Additional liquid structure characterization of FLiBe can be found in Ref.[20]

2.2 Solid Structural Studies of Li_2BeF_4; A Well Characterized Fluoride Salt

Li_2BeF_4 (FLiBe), a 2:1 molar ratio of lithium fluoride (LiF) and beryllium fluoride (BeF_2), is a salt of renewed research interest due to its potential as a fuel solvent, coolant, and tritium breeding blanket in advanced nuclear reactors. Companies such as Commonwealth Fusion Systems and Kairos Power utilize Li_2BeF_4 in their ARC fusion concept and fluoride salt-cooled high temperature reactor (FHR), respectively, and national laboratories such as Oak Ridge National Laboratory (ORNL) have been involved in the study of Li_2BeF_4 for over seventy years [14], [21], [22], [23]. With the further development of molten salt reactors (MSRs), a detailed understanding of the evolution of Li_2BeF_4's structure under different chemical and physical conditions is required. Most experimental and computational fluoride salt structure research for reactor applications focuses on the molten state, as this is the main temperature region of interest for power generation. A structural model of molten Li_2BeF_4 was first proposed by ref. [24], and numerous modern molecular dynamics studies have followed [25], [26], [27], [28], [29], [30], [31]. Most recently, molecular dynamics (MD) studies have been combined with machine learning potentials to capture longer-range structural features in the molten state [32], [33]. Experiments probing the molten structure include neutron and X-ray scattering studies [20], [34] and vibrational spectroscopy (infrared and Raman) [35], [36], [37], [38]. A model of the crystalline structure of solid state Li_2BeF_4 was analyzed by [39], related to the MD calculations of liquid structure by [25] and compared to the X-ray diffraction studies in [40]. In addition to this model, four other studies of solid Li_2BeF_4 at room temperature are known [30], [40], [41], [42]. These studies, however, are limited to single-temperature measurements. There exists no characterization of Li_2BeF_4 thermal behavior over solid/liquid phase transition temperatures or over a temperature range in the solid.

Despite the current lack of thorough treatment of the solid state, there are several reactor applications of solid-state fluoride salt data. For example, initial melting of the salt during reactor start-up, cracking and recrystallization of Li_2BeF_4 during routine and emergency changes in heat load, and modeling of these scenarios for reactor safety analysis. Additionally, the interaction of salt with reactor materials, such as structural metals and graphite, at solid/liquid transitions is relevant, since salt melting/freezing may lead to thermal stresses in the surrounding environment. This study seeks to add to the body of literature by characterizing Li_2BeF_4 thermal behavior at temperatures relevant to reactor startup, shutdown, and freezing incidents, on which data are currently not available.

2.3 Background

Using a crystallographic information file (cif) created with Li_2BeF_4 X-ray diffraction data collected by Seiler [41] at 81 K, a model of the crystal structure of Li_2BeF_4 was created using the program Visualization for Electronic and Structural Analysis (VESTA) [43] (Figure 2).

Li_2BeF_4 is constructed of a rhombohedral symmetry hexagonal lattice and belongs to the crystal structure class phenakite, in the space group R-3H containing *a* and *c* perpendicular axes. This space group and structure is denoted as Number 148 in the International Tables for Crystallography [44]. Of the 62 entries in Inorganic Crystal Structure Database (ICSD) recorded under the phenakite structure designation, two are nitrides, fifty-five are oxides, and five are Li_2BeF_4 fluorides [45], [46]. Since Li_2BeF_4 is trigonal rhombohedral, its symmetry is such that its crystal lattice is described solely by the a and c lattice parameters.

Table 1 provides bond lengths, atom distances, and bond angles from the existing studies of solid crystalline Li2BeF4.

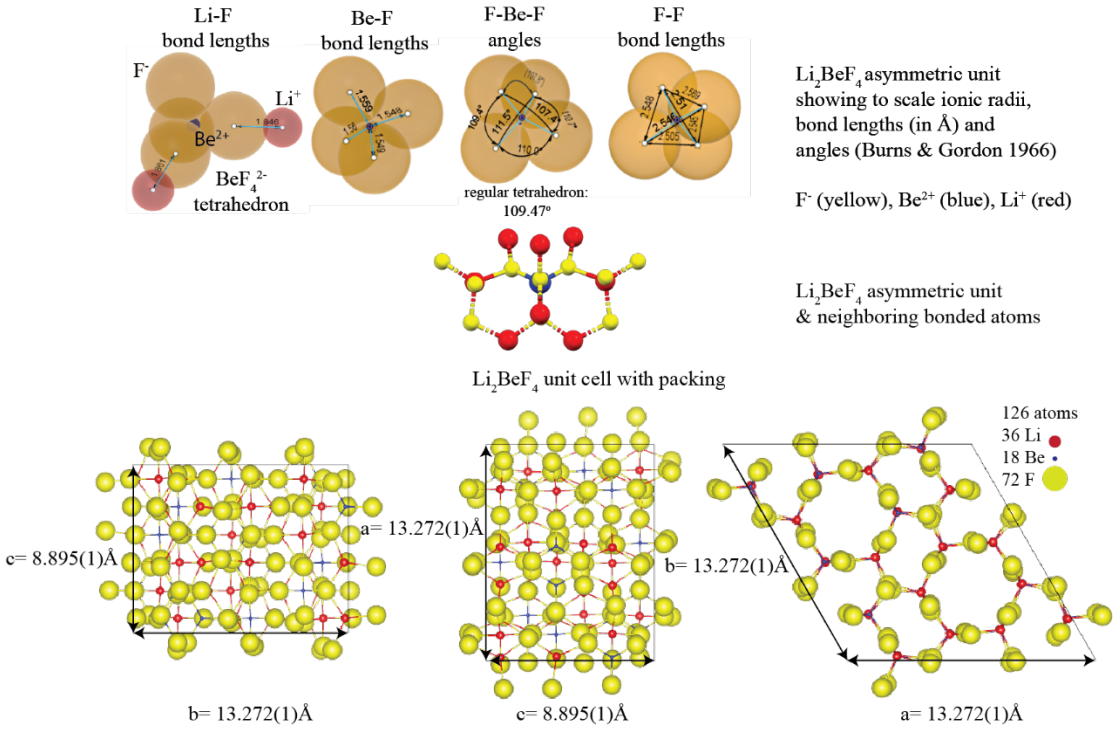

Figure 2. Structure diagram of the Li_2BeF_4. Illustration of ionic sizes in the fluoroberyllate tetrahedron. (CAD model by Sebastian Barnes) and VESTA ball and stick of unit cell model (126 atoms) along the a, b, and c crystallographic axes, respectively. Red: lithium, yellow: fluorine, blue: beryllium. Data from [40], [41], [43].

Table 1. Select coordination numbers, bond distances, and angles inside the solid crystalline Li2BeF4 unit cell [40], [41], [42]

Atoms Involved	Coordination Number	Seiler, Paul 1993 (81K)	Burns & Gordon 1966 (293K)	Collins, Mahar, & Whitehurst 1983 (293K)
Bond Length (Å): Be-F	4	1.559, 1.550, 1.550, 1.561	1.559, 1.560, 1.548, 1.549	1.548, 1.561, 1.560, 1.552
Bond Length (Å): Li1-F	4	1.859, 1.851, 1.889, 1.882	1.861, 1.855, 1.899, 1.887	1.885, 1.860, 1.894, 1.868
Bond Length (Å): Li2-F	4	1.865, 1.863, 1.854, 1.846	1.867, 1.849, 1.856, 1.871	1.869, 1.869, 1.854, 1.859
Atom Distance (Å): Be-Be	0	4.209, 3.971	4.217, 3.972	4.221, 3.980
Atom Distance (Å): F-F (Be)	0	2.513, 2.569, 2.549, 2.547, 2.548, 2.508	2.546, 2.505, 2.545, 2.548, 2.510, 2.569	2.548, 2.549, 2.568, 2.512, 2.550, 2.510
Bond Angle (°): F-Be-F		109.47, 111.33, 110.58, 107.55, 109.96, 107.84	109.40, 109.97, 110.69, 107.40, 107.76. 111.51	109.45, 111.33, 107.84, 109.93, 107.52, 110.66

Li_2BeF_4 thermal expansion behavior is particularly useful to reactor applications that involve phase transitions of the coolant. Freeze valves in MSRs present one such example. In some reactor designs, to avoid problems caused by use of mechanical valves in salt, flow to the drain tanks is stopped by freezing salt inside a flattened section of piping [47], [48]. If flow to the drain tanks is then needed, the salt inside the freeze valve plug is heated, thawing the salt and allowing for flow. As freezing and thawing the salt inside the freeze valve can lead to stress in the piping, it is relevant to have data regarding the direction and magnitude of the expansion of the Li_2BeF_4 crystal structure. Experimental data on the crystal lattice thermal evolution of Li_2BeF_4 are not currently available in the present literature. A computational study on amorphous Li_2BeF_4 by ref. [30] estimated the structural parameters as well as other temperature dependent properties using ab-initio molecular dynamics simulations (AIMD); using a 504-atom amorphous structural model, it was calculated that the *a* and *c* lattice vectors expand isotropically by 6.5% in between from -273°C to 1727°C [30]. Bond length results were stated to be slightly overestimated and hypothesized to cause simulated cell lengths to disagree with experiments [30].

Although there are no entries on the ICSD on the solid-state thermal evolution of Li_2BeF_4, there are studies that have been completed on the lattice parameter thermal evolution of other compounds belonging to the same class [45], [46]. Hazen and Finger showed that phenakite [Be_2SiO_4] expands slightly anisotropically from ambient temperature to 690°C [49]. In their study, from high temperature X-ray diffraction it was calculated that the lattice's *c* cell length expanded 20% more than its *a* cell length as the temperature increased [49]. The coefficient of thermal expansion of phenakite was reported to be 64×10^{-7} cm per cm per C (20-1000°C) by [50] who cites the unpublished thesis of R.A. Morgan (1948).

While previous studies have reported the thermal expansion of other materials in the same crystal class of phenakite, and that of liquid Li_2BeF_4, this work is the first known to have experimentally observed the full evolution of Li_2BeF_4's structural behavior from its solid to liquid state. By using neutron and X-ray diffraction to analyze samples from ambient conditions to 470°C, this work observed the changes of the lattice and unit cell volume parameters over a wide range of temperatures and determined the thermal expansion of each of the two crystallographic axes in the hexagonal unit cell of Li_2BeF_4 from its solid crystal state to its molten form. Additionally, using the unit cell volume extracted from Rietveld analysis

of the neutron diffraction data and the number of atoms per unit cell, the solid density of Li_2BeF_4 has been calculated, compared to liquid density values for Li_2BeF_4 [51], and the observations with regards to volume change upon freezing discussed. Thus, this work seeks to fill the gap of experimental studies of the thermal behavior of pure Li_2BeF_4 in solid-state literature. This work's characterization of pure Li_2BeF_4 establishes a baseline for future studies with added solutes such as fission and corrosion products.

2.4 Materials & Methods

2.4.1 Sample Preparation

Samples for the neutron diffraction experiments were prepared at the University of California, Berkeley using LiF, BeF_2, and LiH. Natural isotopic compositions of beryllium and fluorine were used in the synthesis of the salt. The isotopic composition of lithium in lithium fluoride varied across the samples. Sample isotopic compositions and suppliers are given in Table 2. Inside of an inert argon glove box (<5 ppm O_2, <1 ppm H_2O), the salt was loaded into the vanadium sample cans as shown in Figure 2**.** Using a Phoenix GH-252 analytical balance, approximately 2.5 g of salt was weighed and added to each can using a funnel. One mole percent of LiH was added to the HIPPO 2022 sample to observe the effect on the Li_2BeF_4 when the neutron activation product tritium (hydrogen serving as its surrogate) is solvated in the salt. The loaded, unsealed cans were then placed in a cylindrical furnace inside of a stainless-steel crucible and held at 600℃ until the contents were fully melted. After cooling, the surface of the samples appeared flat. Melting was ensured by visual inspection that no Li_2BeF_4 dust particles remained inside the cans and that the salt had solidified into one solid piece. The 6 mm internal diameter cans contained a salt fill height of around 15 mm. To seal the cans, a 3 mm thick precut graphite foil gasket was added to the can and the top flange was replaced and tightened with wrenches.

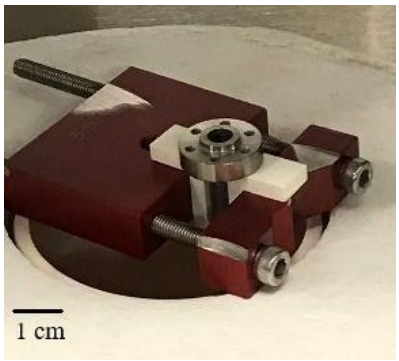

Figure 3. Melting powdered Li_2BeF_4 into a vanadium can, suspended over a cylindrical furnace by a vise. This sample was studied by neutron diffraction at room temperature on the HIPPO instrument at LANL.

Table 2. Li_2BeF_4 samples run as part of this work including the container and temperature collection range.

Sample Name	Composition and materials	Experiment temperature	Containment	$^7Li/^6Li$ Ratio
NOMAD 2022	Enriched Li^7F (ORNL) melted with BeF_2	Ambient to 700°C	Vanadium can and lid with graphite gasket	Stock material assumed to be at least 99(1)
HIPPO 2021	Hydro-fluorinated Li_2BeF_4 with 1 mol% LiH prepared in an argon environment in a nickel crucible [52]	Ambient	Vanadium can with titanium 64 alloy lid	13.544(4)
HIPPO 2022	Natural enrichment LiF (Fisher Scientific, 99.9% purity) & BeF_2 (Materion, 97.55% purity)	Ambient	Vanadium can with aluminum lid	12.17(5)
PDF 2021	Enriched $2Li^7F$- BeF_2 (ORNL, from the MSRE, repurified as reported in [53])	Ambient to 700°C	Capped graphite crucible inside of flame-sealed quartz NMR tube	10555(555)

2.4.2 Beryllium safety

As beryllium is a dermal and inhalation hazard, after sealing, the cans were thoroughly cleaned using Ghost Wipes, then placed in separate bags and stored to await clearance from beryllium surface contamination. To determine the surface level of beryllium contamination present on each can, each was swiped with a Ghost Wipe measuring 100 cm^2 in surface area. These swipes were then sent out for digestion and elemental analysis to determine the level of beryllium present in the units $\mu g/100\ cm^2$.

2.4.3 Neutron Diffraction

Neutron diffraction experiments were completed using the Nanoscale-Ordered Materials Diffractometer (NOMAD) at the Spallation Neutron Source (SNS) [54] and the High-Pressure-Preferred Orientation time-of-flight diffractometer (HIPPO) [55], [56] at the pulsed neutron spallation source at the Los Alamos Neutron Science Center (LANSCE) [57].

NOMAD utilizes intense neutron pulses at 60 Hz for a beam spot of approximately 9 mm diameter, generated by 1 GeV protons directed into a liquid mercury target [54], [58]. NOMAD consists of six banks of ^3He linear position sensitive detectors arranged in groups of eight detectors each distributed around the vanadium sample container. This 10 mm sample container is located 19.5 meters away from the moderator active surface, which is composed of poisoned decoupled supercritical hydrogen. At NOMAD, the filled vanadium sample cans were loaded into the standard Institute Laue Langevin (ILL) vanadium furnace and nitrogen gas lines were connected for sample temperature control [54]. Using a ramp rate of 10 °C/min, the samples were heated from room temperature to 700°C to allow for a complete transition of the Li_2BeF_4 from solid to liquid (the melting point of Li_2BeF_4 is 459.1 ± 0.2 °C) [51], [59]. Thermocouples located in the cryostat furnace above the vanadium can provide temperature readings. Diffraction data in the solid state of the sample was collected during heating at a constant ramp rate for a count time of five minutes per temperature data point.

Ambient condition bulk texture analysis was done on High-Pressure-Preferred Orientation (HIPPO), a neutron time-of-flight powder diffractometer [55], [60] at LANSCE which utilizes neutron pulses at 20 Hz generated through spallation by 800 MeV protons [57]. The combination of an 8.9 m initial flight path between the sample and high-flux/moderate-resolution water moderator and detectors covering 22.4% of 4π allow for short integration times to generate data suitable for Rietveld refinement. The detector system consists of 1200 ^{3}He detector tubes covering 4.8 m^2 of detector area covering 40°-150° in scattering angles. The detector tubes are arranged on five rings around the incident neutron beam. The beam spot size for the 9 mm sample can was 10 mm in diameter. The sample was held by the HIPPO robotic sample changer [61], and data was collected for a count time equivalent to 90 minutes at 100 microamp proton current minutes at sample rotations around the cylindrical axis of the vanadium can at 0°, 67.5°, and 90°.

2.4.4 X-Ray Diffraction

In this work, X-ray diffraction experiments were performed using the Pair Distribution Function (PDF) beamline (28-ID-1) at the National Synchrotron Light Source II (NSLS-II) [62]. The PDF beamline uses an amorphous-silicon-based flat-panel detector which is set orthogonal to the beam path [20]. The X-ray energy used to collect XRD patterns was 74 keV. A LaB_6 powder standard was used to calibrate the sample to detector distance and to aid in the two-dimensional to one-dimensional data reduction.

The sample, which was melted from a powder inside a graphite crucible using the same method as described in Section 3.1, was contained within a graphite crucible with lid, placed inside of a quartz tube sealed under argon. To collect lattice parameters' and thermal expansion values, the sample was heated with a ramp rate of 5 °C/min using a hot air blower [20] and data was collected with an exposure time of 30 s for each measurement [20].

2.4.5 Data Analysis

To analyze the data generated by NOMAD and PDF, the program General Structure Analysis System (GSAS) was used to perform analysis using the Rietveld Method [63]. For automated analysis of multiple datasets, a script written in gsaslanguage was used to automate the Rietveld analysis. The Rietveld method is a refinement method used for crystal structure determination [64]. Refined parameters include background and lattice parameters. Structural parameters such as thermal motion parameters and atomic positions were not refined due to the samples being resolidified powders with strong preferred orientations [65], [65], [66]. The crystal structure as reported by Seiler was used as the starting parameters for refinement [41].

For the bulk texture analysis from the HIPPO data, the Rietveld code Materials Analysis Using Diffraction (MAUD) was used following procedures as described in [67]. The 135 diffraction patterns resulting from the 45 HIPPO detector panels and the three sample rotations were refined simultaneously using the crystal structure as reported by [41]. The orientation distribution function (ODF) was represented by the E-WIMV method [58] using a resolution of one degree of the ODF.

2.4.6 Coefficient of Thermal Expansion Fitting

To describe the evolution of Li_2BeF_4's unit cell dimensions from room temperature to its melting point, the thermal expansion of the unit cell volume (i.e., molar volume), and the *a* and *c* parameters are fit to an equation to extract the coefficient of thermal expansion (CTE) for each.

$$f(T) = f_0(1 + \alpha_f(T - T_0) + \beta_f(T - T_0)^2)$$

Equation 1

In Equation 1, for the *a* parameter, *c* parameter, and unit cell volume (V), *f(T)* is the value of the lattice parameter or unit cell volume at a specific temperature (T), f_0 is the initial value at the room temperature T_0 of 293 K, α_f is the linear coefficient of thermal expansion term, and β is the quadratic coefficient of thermal

expansion term. Dilatometry extracted CTE values from literature can then in turn be compared to the experimental values of α_f and if necessary β_f CTE values extracted from the unit cell volume thermal expansion. To the best of our knowledge, no previous literature on CTE values for solid Li_2BeF_4 is available.

2.5 Results

2.5.1 Room Temperature Literature and Experimental Validation

The lattice parameter results from NOMAD, HIPPO, and PDF on Li_2BeF_4 for *a* and *c* as well as the *c/a* ratio at room temperature are shown in Figure 4 along with literature values for comparison.
The NOMAD 2022 experiment took place as a room temperature measurement that was then ramped to and held at 510°C and 700°C for PDF data collection. Note the differences in isotopic enrichment of lithium-7, as described in Table 2. Two measurements at room temperature were also run at the HIPPO instrument. Also note the differences in composition in Table 2 (namely, the addition of 1 mol% LiH in the HIPPO 2021 sample).

Using the International Crystal Structure Database (ICSD), crystallographic information from three separate experiments is found from [40], [41], [42], [44]. These experiments, unlike the experiments undergone as part of this work, utilized X-ray diffraction measurements on single crystal samples. Finally, the results from this work are also compared to the simulation studies using ab-initio molecular dynamics (AIMD) by [30] and the Born-Mayer-Huggins Model by [39].

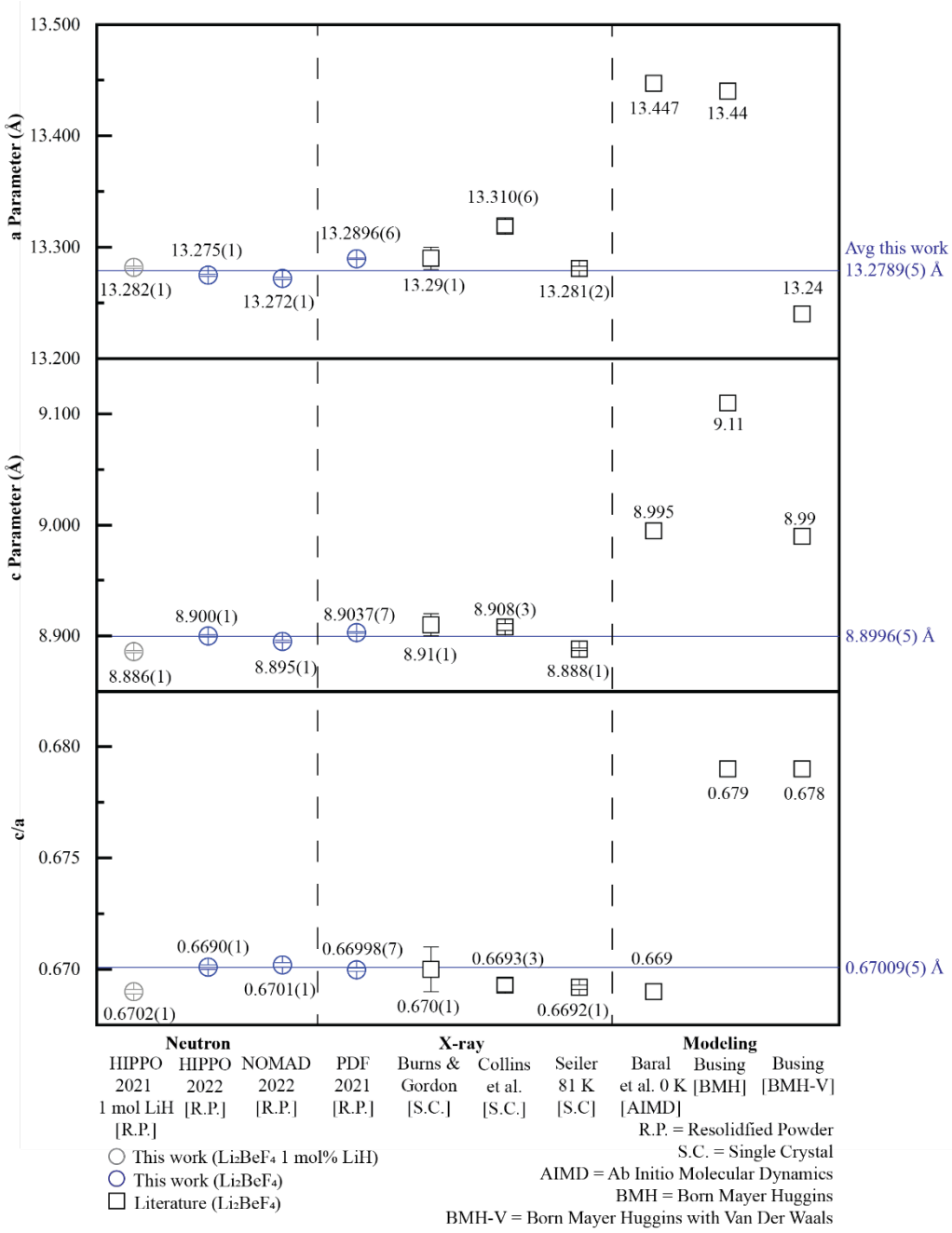

Figure 4. Comparison of Li_2BeF_4 lattice parameters from this work and literature at room temperature. The sample types are denoted as R.P. for resolidified powder, S.C. for single crystal, AIMD for Ab-Initio Molecular Dynamics, BMH for Born-Mayer-Huggins model, an BMH-V for Born Mayer Huggins model with Van Der Waals Parameters.

2.5.2 *Temperature Dependence of Lattice Evolution*

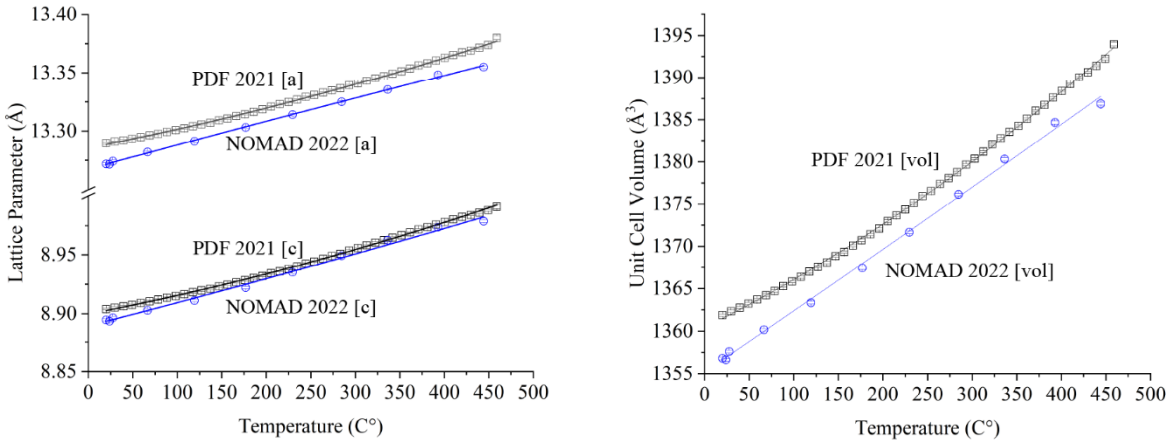

Figure 5. NOMAD 2022 and 28-ID-1 PDF thermal expansion measured of Li_2BeF_4 lattice parameters *a*, *c*, and unit cell volume fit to Equation 1 using the values reported in Table 3.

Table 3. Equations for the polynomial fit of lattice parameter *a* and *c* and relative change thermal evolution fit to the form $f(T) = f_0(1 + \alpha_f(T-T_0) + \beta_f(T-T_0)^2)$ where f_0 is lattice parameter *a*, *c*, and the unit cell volume V and T_0 is 293 K for Li_2BeF_4 with 126 atoms in the solid unit cell.

		Lattice Parameter *a*	Lattice Parameter *c*	Unit Cell Volume (V)
Neutron Diffraction (NOMAD)	f_0	13.2718(5) Å	8.8935(6) Å	1356.65(8) Å^3
	α_f	1.55(5) ×10^{-5} K^{-1}	2.19(9) ×10^{-5} K^{-1}	5.27(9) ×10^{-5} K^{-1}
	β_f	-1(1) ×10^{-9} K^{-2}	3(2) ×10^{-9} K^{-2}	3(2) ×10^{-9} K^{-2}
X-ray Diffraction (PDF)	f_0	13.2886(3) Å	8.9026(3) Å	1361.48(5) Å^3
	α_f	1.14(2) ×10^{-5} K^{-1}	1.70(4) ×10^{-5} K^{-1}	3.98(4) ×10^{-5} K^{-1}
	β_f	8.5(5) ×10^{-9} K^{-2}	1.38(8) ×10^{-8} K^{-2}	3.19(9) ×10^{-8} K^{-2}

The results of the Rietveld analysis on the NOMAD 2022 neutron diffraction and the PDF 2021 X-ray diffraction data values for the *a* parameter, *c* parameter, and unit cell volume V against temperature are shown in Figure 5. NOMAD 2022 and 28-ID-1 PDF thermal expansion measured of Li_2BeF_4 lattice parameters *a*, *c*, and unit cell volume fit to Equation 1 using the values reported in Table 3.Figure 5. Using Gnuplot, the unit cell data is fit to Equation 1 [68]**.** The resulting coefficients with uncertainties are reported in Table 3**.** For the neutron diffraction results, the quadratic coefficients β_f**'s** $_{\text{uncertainty}}$ is above 50% in all three cases, indicating that the thermal expansion behavior is well described by a linear function. For the X-ray diffraction results, the error on the quadratic term is lower and ranges from around 3 to 6%. The linear α_f coefficient for both datasets for the *c* parameter is around 1.4 times larger than that for the *a* parameter indicating significant anisotropic thermal expansion between the axes.

2.5.3 *Thermal Strain and Anisotropy*

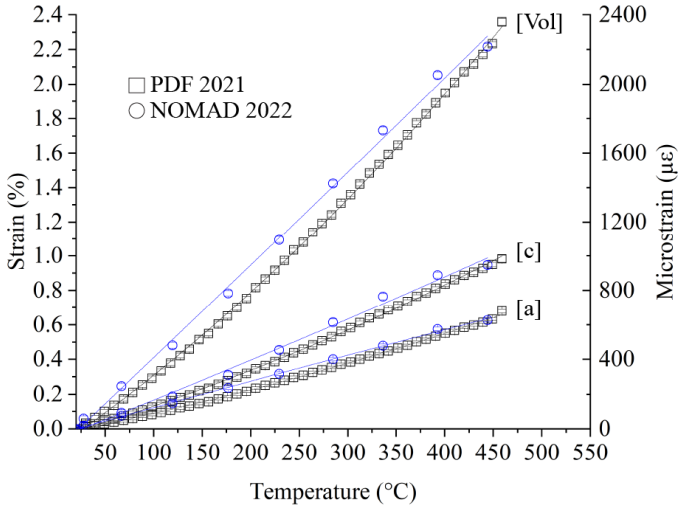

Figure 6. The thermal lattice strain of the *a* and *c* axes as well as the unit cell volume expansion of Li_2BeF_4 for NOMAD 2022 and PDF 2021 as a function of temperature from room temperature to melting point.

To quantify the anisotropy of the lattice expansion, the absolute lattice parameters as a function of temperature were converted to thermal strains by dividing each by the room temperature value followed by fitting the thermal strains to Equation 1. The results are shown in Figure 6**.**

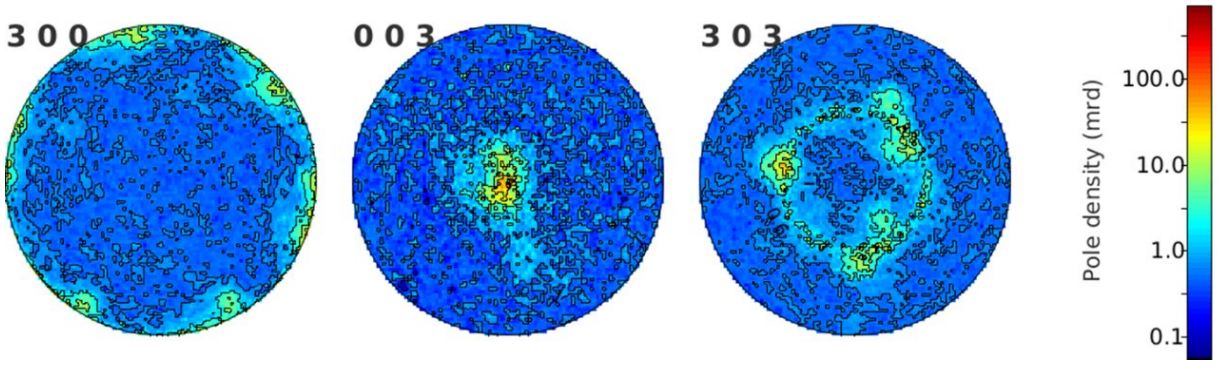

Figure 7. Pole figure of solid room temperature Li_2BeF_4 + 1mol% LiH measured along the longitudinal axis of the cylindrical can on the HIPPO instrument at LANL from HIPPO 2021. Note that the pole density in multiples of random distribution (mrd) is on logarithmic scale.

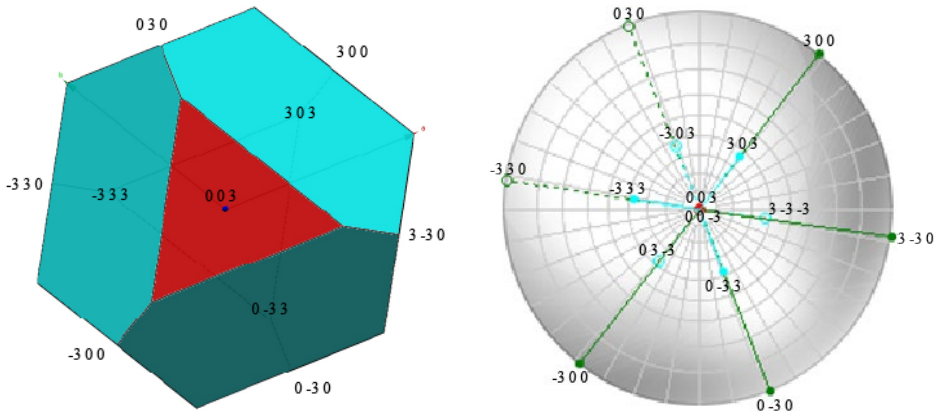

Figure 8. (Left) Single crystal model of Li_2BeF_4 made using lattice values from NOMAD 2022 with KrystalShaper (003) planes shown in red, (303) planes shown in blue, (300) planes shown in green). (Right) Stereographic projection of the poles of the Li_2BeF_4 single crystal. [69]

To understand the solidification microstructure of Li_2BeF_4, the bulk texture of the material molten inside the vanadium sample can was characterized with the HIPPO instrument. The material preparation for this sample is equivalent to the one for the NOMAD 2022 samples as described in Section 3.1. It is important to note that the loaded can of liquid Li_2BeF_4 + 1 mol% LiH was allowed to cool naturally without quenching during salt solidification. Figure 7 shows the (0 0 3) and (3 0 0) pole figures resulting from the HIPPO analysis. Figure 8 shows the shape of a Li_2BeF_4 single crystal simulated with the KrystalShaper software as well as a stereographic projection of the same crystal orientation.

2.5.4 Density Comparison of Lattice Cell Evolution and Experimental

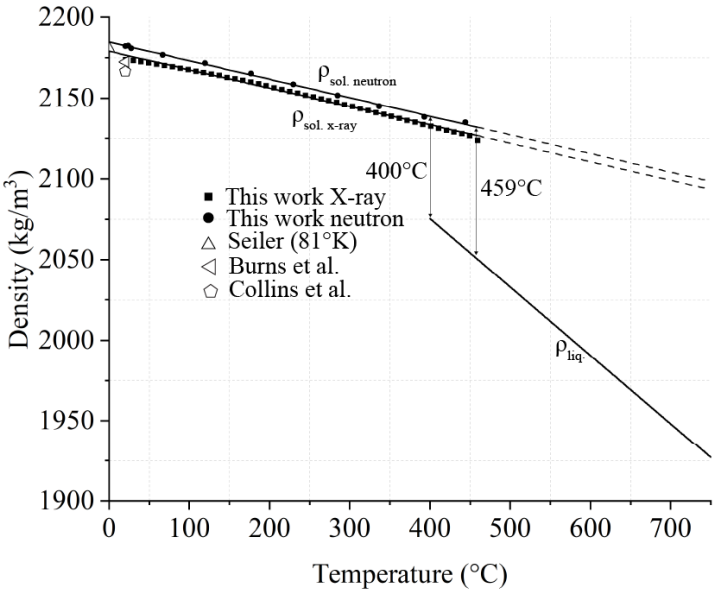

$Mol\ Vol_{solid,xray}\ \left[\frac{m^3}{mol}\right] = 1.5152(2) \times 10^{-5} + 8.1(2) \times 10^{-10} T\ [°C]$
$Mol\ Vol_{solid,neutron}\ \left[\frac{m^3}{mol}\right] = 1.5113(3) \times 10^{-5} + 8.09(3) \times 10^{-10} T\ [°C]$
$Mol\ Vol_{liquid,[30]}\ \left[\frac{m^3}{mol}\right] = 1.45(2) \times 10^{-5} + 3.6(3) \times 10^{-9} T\ [°C]$
$\rho_{solid,xray}\ \left[\frac{kg}{m^3}\right] = 2179.1(3) - 0.114(1) T\ [°C]$
$\rho_{solid,neutron}\ \left[\frac{kg}{m^3}\right] = 2184.8(4) - 0.115(2) T\ [°C]$
$\rho_{liquid,[30]}\ \left[\frac{kg}{m^3}\right] = 2245(7) - 0.424(17) T\ [°C]$

volume shrinkage upon freeze at 400˚C	X-ray	2.8(5) %
	neutron	3.0(5) %
% difference x-ray/neutron at 400˚C	0.25(6) %	

volume expansion upon thaw at 459˚C	X-ray	3.7(5) %
	neutron	3.9(5) %
% difference x-ray/neutron at 459˚C	0.24(7) %	

Figure 9. Measurements of solid density and molar volume using NOMAD 2022 neutron and X-ray diffraction results and measurements of liquid density and molar volume using the hydrostatic method for Li_2BeF_4 with propagated error[70].

As the trend of the unit cell volume temperature dependent change is measured for Li_2BeF_4 using neutron diffraction in this work, it is possible to extract the solid density at the measured temperatures as well. The experimental liquid density of Li_2BeF_4 was previously measured using the hydrostatic method [51], which used a bobber suspended by a wire to measure the liquid density with high precision. Though the measurements in ref. [51] took place at higher temperatures than this work, results are compared to provide estimates of the validity of this work. Ref. [51] calculated the following equation for their density measurements:

Liquid Li_2BeF_4 Density [51]

$$\rho_{FLiBe}[\frac{kg}{m^3}] = 2245(7) - 0.424(17)T[\text{°C}];$$

$$\text{for 447 to 820°C for } 22.59(5)\text{mol\%BeF}_2, \frac{^7\text{Li}}{^6\text{Li}}(\text{at})13.544(4), 33.02(5)\ \text{g/mol FLiBe.[51]}$$

Equation 2

Ref. [51] collected data regarding the lithium isotopic ratio, molecular weight with error, as well as the mole percent of melt species with error.

Equation 2 is only for the liquid density and measured accurately to temperatures as low as 447 °C.

By extrapolating, the density of Li_2BeF_4 at 444.19 °C is 2.056(10) g/cm^3 according to [51].

$$\rho\left[\frac{g}{\mathrm{cm}^3}\right] = MW\left[\frac{g}{mol}\right] \div Molar\ Volume\ \left[\frac{cm^3}{mol}\right];$$

$$Molar\ Vol.\left[\frac{cm^3}{mol}\right] = Unit\ Cell\ Vol. \div (No.of\ FLiBe\ units\ in\ crystal\ unit\ cell\ (54) \div N_{Avogadro})$$

Equation 3

Where one FLiBe unit has stoichiometry of $Li_{0.67}Be_{0.33}F_{1.32}$, and for Li^7/Li^6 (at) = 13.544(4), the corresponding molecular weight becomes: 33.02(5) g/mol, and there are 54 FLiBe units in a unit cell of 126 atoms.

Average solid Li_2BeF_4 Density (this work)

$$\rho\left[\frac{kg}{m^3}\right] = 2184.8(4) - 0.115(2) \times T\ [°C];$$

$$for\ 23\ to\ 444\ \mathrm{K};\ \frac{^7Li}{^6Li}(at) = 99(1);\ 32.979\frac{g}{mol}FLiBe, 126\ atoms\ per\ unit\ cell$$

Equation 4

Using the structure visualization program Mercury 4.0, from the Cambridge Structural Database System, it was found that there are 126 atoms per unit cell of Li_2BeF_4 [71], [72]. Of these 126 atoms, 72 are fluorine, 36 are lithium, and 18 are beryllium. One asymmetric unit of this unit cell contains 1 beryllium atom, 2 lithium atoms, and 4 fluorine atoms. Using the Seiler, P. (1993) Z value showing the number of units inside a Li_2BeF_4 unit cell of 18, and the standard FLiBe molecular weight of 33.02 g/mol, the density of Li_2BeF_4 was calculated.

The comparison of the trendlines and values of the solid neutron diffraction density measured from this work with liquid hydrostatic method density measured by [51] is shown in Figure 9**.** The melting temperature of Li_2BeF_4 is known to be 459 °C, however it has been to observed to supercool as low as 400 °C [51]. By extrapolating the equation produced by [51] from its lowered measured temperature of 447 °C to the lowest observed supercooled state of Li_2BeF_4 at 400 °C and comparing the calculated value to the measure diffraction density, a 2.8(5) to 3.0(5)% range of volume shrinkage upon salt freezing was found. Similarly, a 3.7(5) to 3.9(5) % range of volume expansion was found when melting at 459 °C.

2.6 Discussion

2.6.1 Low Temperature Literature and Experimental Validation

In Figure 4, a comparison of the room temperature lattice parameter magnitudes for Li_2BeF_4 is shown for three neutron and one X-ray diffraction experiments from this work, three X-ray diffraction experiments from literature, and two modeling studies from literature. Between the two studies conducted on the same instrument, the variation in values between HIPPO 2021 and HIPPO 2022 may have been caused by the addition of 1 mol% LiH in HIPPO 2021. When comparing the set of room temperature diffraction data collected as a part of this work with the set of three single crystal X-ray diffraction experiments found in literature, the P values between the two methods for the *a* and *c* parameters are 0.0909 and 0.7028, respectively, implying that there is no statistical significance between data sets [73]. When repeated for the *c/a* ratio, a P value of 0.6769 is calculated showing no statistically observed difference between the two methods [73]. The ab-initio structural optimization of the 126-atom unit cell for crystalline FLiBe at 0K predicts a unit cell with larger volume than the experimental studies shown but yielded a c/a ratio of 0.669, which is quite close to the c/a ratio of 0.67009(5) measured in this work [30]. An earlier

computational study performed using the Born-Mayer-Huggins models with and without the addition of the Van Der Waals term both predict a higher *c/a* ratio value of 0.678 and 0.679 respectively than this work [39]. The addition of the Van Der Waals term leads to *a* and *c* values closer to those experimentally measured, but lack the ability to accurately capture the crucial ionic polarization and covalent bonding interactions as highlighted in ref. [39]. These discrepancies highlight the importance of using highly accurate DFT functionals while modelling the structural properties and thermal expansion for solid FLiBe. The low statistical difference in the *a* parameter, *c* parameter, and *c/a* between the resolidified powder neutron diffraction experiments from this work and the three single crystal X-ray diffraction experiments found using the ICSD validates the credibility the lattice parameters via the repeatability of measurements [45], [46].

2.6.2 Temperature Dependence of Lattice Evolution

When measuring the lattice parameter magnitudes over a range of different temperatures, the first observation from Table 3 is that the behavior of thermal expansion of each of *a*, *c*, and V as a function of temperature is best described by a linear fit. When fitting to Equation 1 to calculate the coefficient of thermal expansion for the lattice parameters as well as unit cell volume, the asymptotic standard error extracted from the fit of the thermal expansion data points for the initial magnitude f_0 is below 1% for all measured variables [70]. The α_f term error for *a*, *c*, and V is also accurate having an error below 5% for all three variables.

The removal of the quadratic term for both datasets results in a decrease on the overall fit error indicating the behavior measured by neutrons and X-rays can best be described by a linear function. The resulting fits and errors are shown in Table 4.

Table 4. Recommended thermal expansion coefficients for Li_2BeF_4 based on the neutron and x-ray diffraction experiments from this work fit to the form $f(T) = f_0(1 + \alpha_f(T-T_0) + \beta_f(T-T_0)^2)$ where f_0 is lattice parameter *a*, *c*, and the unit cell volume V and T_0 is 293 K for Li_2BeF_4 with 126 atoms in the solid unit cell.

		Lattice Parameter *a*	Lattice Parameter *c*	Unit Cell Volume (V)
Average Li_2BeF_4 Thermal Expansion Coefficients	f_0	13.2785(3) Å	8.8959(3) Å	1358.35(4) $\times 10^3$ Å^3
	α_f	1.51(1) $\times 10^{-5}$ K^{-1}	2.32(1) $\times 10^{-5}$ K^{-1}	5.38(1) $\times 10^{-5}$ K^{-1}

$$\text{for } [23 \text{ to } 444 \text{ K}, \frac{^7\text{Li}}{^6\text{Li}}(\text{at}) = 99(1), 32.979 \frac{\text{g}}{\text{mol}} \text{FLiBe}, 126 \text{ atoms per unit cell}]$$

Equation 5

As Table 4Table 4 and the recommended linear correlation equations show, the α_f term of the *c* CTE is slightly larger than the α_f term of the CTE for *a*, denoting anisotropy between the axes of the unit cell; however, this difference in the rate of thermal expansion for these two parameters is relatively small which lowers the probability of solid Li_2BeF_4 crystals cracking due to thermal stress between axes.

2.6.3 Thermal Strain and Anisotropy

When analyzing the anisotropic thermal expansion behavior using the thermal strain measurements displayed in Figure 6, it is found that at 444 °C, the *c*-axis strain with a magnitude of 1.00% is around 1.54 times the *a* strain at the same temperature (0.65%). When not accounting for anisotropy and only measuring the unit cell volume strain, a value of 2.14% is found as shown in Figure 6**.** This value is what would be

compared to any literature values of Li_2BeF_4 thermal strain found using dilatometry if they were to exist; however, to determine the thermal stress that this strain from thermal expansion applies on its surroundings, the Young's Modulus of Li_2BeF_4 is needed. The impact of the anisotropy observed between the *a* and *c* directions is more consequential if the bulk solid has a preferred orientation. If the *a* and *c* axes of each unit cell are oriented in random directions throughout the solid structure, then the unit cell volume strain and any dilatometry measurements can be used. However, if preferred orientation does occur, then the contribution of each parameter and, in turn, the magnitude of the thermal strain will vary depending on the direction.

The pole figures in Figure 7 indicate the texture of the Li_2BeF_4 sample by showing the orientation of the crystallographic grains within by measuring the pole density. This pole density, which is measured in units of multiples of random density (mrd), is denoted by color showing the probability of finding grains oriented in the viewed direction. The figure shows a two-dimensional representation of the pole density viewed from the axial direction of the cylindrical can (the cylindrical axis of the sample can is in the center of the pole figures). It is observed that in the center of the can, the density of the *a* axis shown by (3 0 0) is lower than the density of the *c* axis shown by (0 0 3) in same direction. This indicates that the solid Li_2BeF_4 has preferred orientation with the majority of the *a* axes oriented radially while the *c* axes are primarily oriented along the cylindrical axis. In the (3 0 0) pole in Figure 7, there are six concentrated areas of pole density located in 60° intervals around the perimeter of the can. As the model in Figure 8 shows, the Li_2BeF_4 single crystal contains 14 faces with the six faces in the (3 0 0) group located at 60° intervals perpendicular to the c axis. Similarly, for the two faces in the (0 0 3) group for the Li_2BeF_4 single crystal, the positioning of the faces 180° apart aligns with the pole density shown in the (0 0 3) pole of the pole figure. The comparison between the KrystalShaper single crystal model and the pole figure of the (3 0 3) poles further correspond with the three (3 0 3) group poles from the simulation corresponding to pole figure areas of high mrd [69]. The areas of concentrated pole density shown in pole figure aligning with the single crystal model indicate that in the 6 mm vanadium can, there is one large single crystal encompassing the entire filled volume. As a perfect Li_2BeF_4 single crystal aligned vertically would result in more point-like behavior of the pole density as shown by the stereographic projection in Figure 8, the shape of the areas of pole density in the center and around the edges of the can may denote a slight offset in the angle of the single crystal. The large crystal shown in this work is similar to a study completed by Burns & Gordon where their method used to create the single crystals used in X-ray diffraction experiments was to grow crystals by slowly cooling molten Li_2BeF_4, then grind the large crystals produced down to the desired size [40].

As it is known that crystals solidify along a temperature gradient, with nucleation beginning at the coldest point, which in the case of this work is the vanadium can wall, then growing crystals inward towards the hotter center as the liquid cools, it can be concluded that the *a* axes of the crystals' unit cells preferentially aligns along a temperature gradient while the *c* axes aligns perpendicular to a temperature gradient [74]. As it was previously noted that the strain of the material varies depending on the unit cell axis, this evidence of preferred orientation indicates the possibility of the applied stress on the surroundings in the axial and radial directions to be widely different at temperatures near 444 °C.

2.6.4 Density Comparison of Lattice Cell Evolution and Experimental

The 3.0-3.9% difference between the volume of solid and liquid Li_2BeF_4 measured from this work aligns with observations from literature on similar salts. The salt from the Molten Salt Reactor Experiment (MSRE), consisting of LiF-BeF_2-ZrF_4-ThF_4-UF_4 at a mole percent ratio of 69.0-23.0-5.2-1.7-1.1, at ORNL was reported to have around a 2% volume shrinkage upon freezing however, the source does not note how this study was conducted [75].

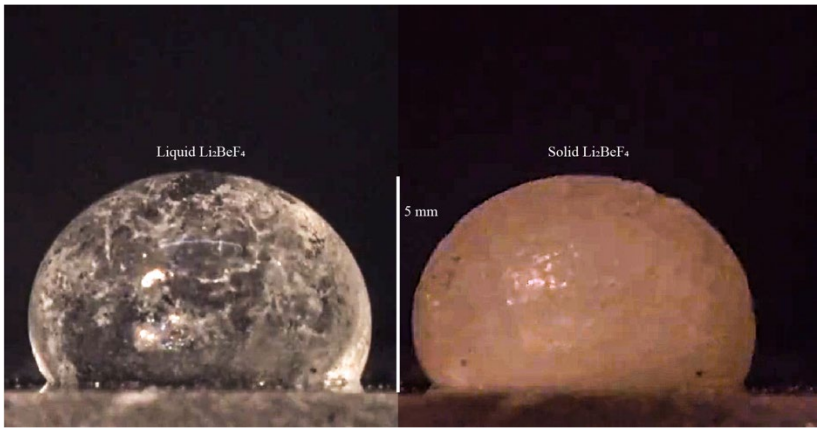

Figure 10. Li_2BeF_4 droplet imaged while in the liquid and solid state.

This work imaged a sample of Li_2BeF_4 inside an oven on a graphite substrate (Toyo Tanso, IG-110). Images were taken from 370 to 471°C, visually observing freezing and melting transients. Analysis of these photos prior to and after freezing revealed a volume shrinkage upon freezing of confidently less than 5% (this value could be lower; more detailed imaging would be needed for more quantitative analysis).

2.7 Conclusion

This work presents a comprehensive examination of the crystal structure thermal evolution of Li_2BeF_4 from room temperature to its melting point. This behavior was described by calculating the coefficients of thermal expansion for this salt for the first time. It was found that the thermal expansion of the *a* and *c* lattice parameters as well as the unit cell volume was best described using a linear fit. The rate of expansion of the *c* parameter was found to be 1.54 times the rate of the *a* parameter; however significant anisotropy in the thermal strain behavior of these unit cell axes was noted. An important observation from this study is the presence of strong preferred orientation in crystalline Li_2BeF_4. It was found that the *a* axis of the unit cell aligns with the temperature gradient during crystal formation, while the *c* axis aligns perpendicular to a temperature gradient. However, due to the *c* axis undergoing around 54% greater thermal strain of 1.00% from room temperature to melting, there is less strain in the axial direction as the thermal strain of the *a* lattice parameter was found to be only 0.65%. An average of 2.9(4) % to 3.8(4) % difference between the liquid and solid was found when comparing solid density neutron diffraction measurements with hydrostatic liquid density measurements from a previous study aligning with results taken from literature for similar salts. Additional liquid structure characterization of the same FLiBe sample is available in Ref.[20].

3 ACTINIDE AND FLUOROBERYLLATE STRUCTURAL EFFECTS ON THERMOPHYSICAL PROPERTIES

3.1 Chapter Summary

Molten beryllium and uranium containing fluoride salts such as NaF-BeF2-UF4-ZrF4 and NaF-BeF2 are examples of fuel solvent and heat transfer salts used in molten salt reactor designs. To observe the behavior of these salts and to ascertain the mechanisms behind the ionic complex formation present in their molten state, this work used high temperature rheology and hydrostatic density methods to measure thermophysical properties. Similar to modeling literature, two regions of viscosity were identified: one below 60 molar percentage of complex forming cations where it is hypothesized that viscosity is driven by the diffusion of small ionic fragments, and one above where it is hypothesized the degree of polymerization of the complexing cation and network formation drives the increase in viscosity.

3.2 Introduction and Background

Density and viscosity are two of the thermophysical properties of fluoride salts whose characterization is useful for molten salt reactor (MSR) applications. For example, in molten salt reactor designs that incorporate natural circulation salt loops, thermal expansivity, density, and viscosity are necessary to design the required loop geometry for natural circulation and passive heat removal. Density and viscosity also are essential to calculating pumping power required for salt flow, predicting the migration of gaseous fission products in the reactor core, and designing for effective heat transfer in the heat exchanger [76], [77], [78]. NaF-BeF_2-UF_4-ZrF_4 denoted UZrFNaBe, and NaF-BeF_2 denoted FNaBe, are two candidate salts for molten salt reactors as a fuel and heat transfer fluid respectively.

During molten salt reactor operations, in addition to transients such as temperature and salt flow rate, due to the fission process, elements across the periodic table are present in the salt system. Understanding of the mechanisms of complex formation in uranium and beryllium containing fluoride salts and its effect on density and viscosity allows for more accurate modeling of molten salt thermophysical property behavior at various temperature conditions as well as better prediction of the effect of fission and corrosion products over the reactor lifetime [11], [28], [79].

Beryllium fluoride containing molten salt systems have been studied for decades through a variety of methods. In 1969, a polymer model was proposed describing the oligomer forming behavior of BeF_2 containing molten salts and hypothesized that increasing the BeF_2 content in a melt increased the number and length of long polymer chains present which are formed from BeF_4^{2-} linkages through corner sharing fluorines [24]. Thermophysical property measurements such as viscosity have been used to demonstrate how increasing the BeF_2 content in a LiF-BeF_2 melt increases the viscosity and activation energy of viscosity due to network formation[80]. Viscosity has also been used to observe how in BeF_2, a tetrahedrally-linked network-forming liquid, the molten structure is weakened by the addition of components such as LiF which cause the severing of bridging fluorines [81]. This structural network-breaking behavior has also been noted to be caused by the addition of CeF_3 in LiF-NaF-BeF_2 melts[82]. X-ray and neutron diffraction studies as well as *ab initio* and neural network molecular dynamic simulations have been used to confirm the presence of these network species and measure the coordination number and polymer chain length of fluoroberyllate complexes [20]. This relationship between properties and complex ion structure is also present when the weakly-coordinating cation Li^+ is instead Na^+ as is the case in NaF-BeF_2 melts [83].

Similarly, experimental and modeling studies have shown that uranium-containing molten fluoride salts have been found to form polymerized networks of corner, face, and edge sharing complexes [84]. Coordination numbers for beryllium and uranium in fluoride salts have been measured and simulated to be around 4 and 8 respectively [20], [84], [85]. Zirconium fluoride melts have also been studied through experimental and simulation techniques and measured to have a coordination number ranging from 6 to 9 [86], [87].

Molecular dynamics computer simulation has identified two regions of viscosity mechanisms in LiF-BeF_2 melts [79]. At low BeF_2 content below 50 molar percentage, viscosity is primarily driven by the diffusion of ionic species such as BeF_4^{2-} formed by the fourfold coordination of beryllium, while at high BeF_2 content the main driver of viscosity is the structural relaxation of beryllium oligomer networks as the length of the polymeric chains increase [79]. UF_4 melts have been modeled to show similar behavior to fluoroberyllate melts[84]; it exists primarily as UF_8^{4-} ionic species at low uranium content below 20 molar percentage, and has network forming character at high uranium content.

The goal of this work is to use thermophysical properties, namely viscosity, density, and thermal expansivity to probe the structure NaF-BeF_2-UF_4-ZrF_4 and NaF-BeF_2 to compare the mechanisms of uranium and beryllium network forming behavior. Comparing density and thermal expansivity values with literature and experimentally providing currently unpublished values of viscosity for potential advanced reactor fuel and coolant salts provides data pertinent to molten salt reactor applications and betters understanding of the effect of solvated fuel on the thermophysical properties of salt melts.

3.3 Materials & Methods

3.3.1 Elemental Analysis and Composition Determination

Compositional measurement was completed using dilute 20 M nitric acid in a CEM SP-Discover 80 Microwave Digester System for salt digestion and a Perkin Elmer 5300 DV Inductively Coupled Plasma – Optical Emission Spectroscopy (ICP-OES) for elemental analysis. Percent recovery and digestion efficiency was calculated from the ICP-OES measured intensity of the initial masses of approximately 0.05 g of sample digested compared to the calibration curve created using Inorganic Ventures elemental analysis standards.

3.3.2 Density Measurements

Density measurements were performed using the hydrostatic method. This method is based on the principle of Archimedes: a body fully immersed in a fluid will experience a force equal to the weight of the displaced fluid. The set-up shown in Figure 11 was placed in an argon glovebox (LC Technology Solutions Inc) with an atmosphere of argon (AirGas cylinder 99.999% purity). Pressure was kept between P_{atm}-0.2 mBar and P_{atm}-0.1 mBar, and oxygen and moisture levels were kept below 5ppm and 0.1 ppm respectively. The volume of the 316 stainless-steel bobber (designed and machined at UC Berkeley) was calibrated using Cargille Laboratories NIST traceable organic series fluids of 0.800 and 3.310 g/cc density. The bobber was then suspended from the hook of a GH-252 analytical scale (A&D Company), with a precision of 0.1 mg, using a 0.51 mm diameter nickel-chrome wire (WIREOPTIM). Underneath the bobber and scale, a glassy carbon crucible measuring 50 mm in diameter and 85 mm in height (SPI Supplies) containing the salt and a type N thermocouple (OMEGA, TJ36-NNIN-116U-18-SB-SMPW-M) was located inside of a CFRC-36/115-A vertical tube furnace (WATLOW) and placed on a scissor jack. The furnace and thermocouple were connected to a Platinum Series proportional–integral–derivative (PID) controller (OMEGA, part# CS8DPT) to set a stable temperature for each experiment (P=8.8; I =0.001; D 336.00).

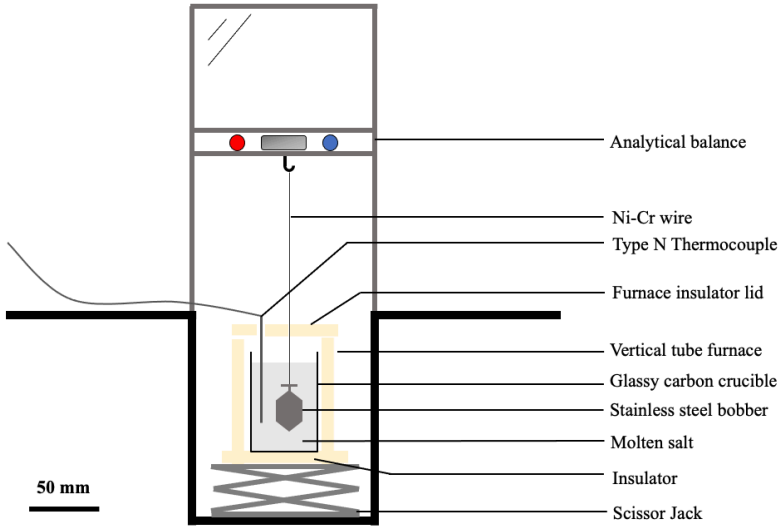

Figure 11: Scheme of the hydrostatic method set-up.

After hanging the bobber, the scale was tared, the salt was melted, and the bobber was immersed into the molten salt using the scissor jack to lift the furnace assembly. After complete immersion of the bobber into the molten salt was confirmed visually, the value measured by the scale corresponded to the difference of weight ΔM. ΔM measurements were made with NIST-traceable density calibration fluids (0.8000 and 0.3100 g/cm3) at 25 ºC and with molten salt at high temperature.

After the immersion of the bobber, an insulating lid was placed on top of the furnace. ΔM was then recorded every 10 seconds for 15 minutes (90 points) using the RsCom WinCT software (A&D Company). Average ΔM and standard deviation were calculated on 90 points at each temperature T. After each experiment, salt was left to cool to ambient temperature by using the glovebox cooling fans and heat exchanger. Frozen salt was then removed from the crucible and stored in a plastic container in the glovebox. Figure 12 gives density benchmarking results on LiF-BeF_2 (FLiBe) and thermocouple cooling curves from this setup.

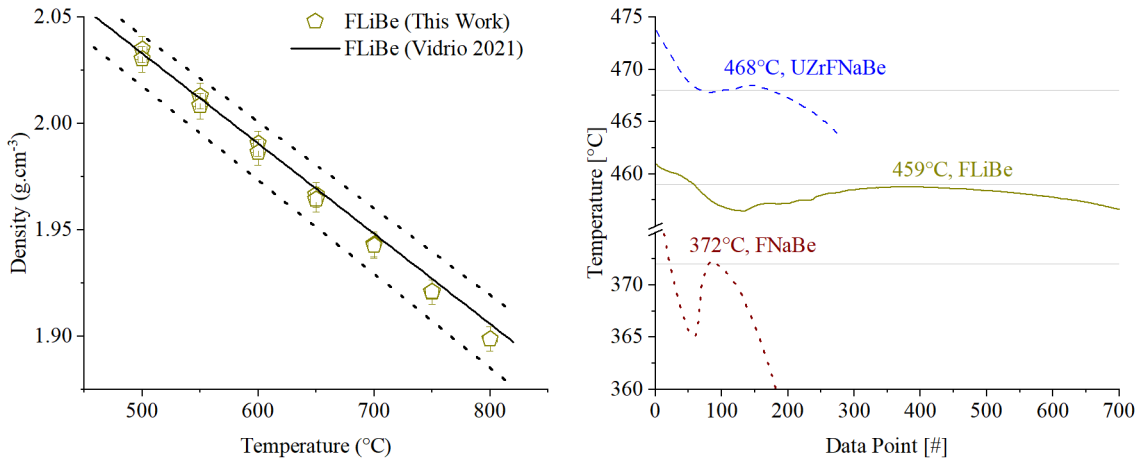

Figure 12. (Left) Density benchmarking against previously reported FLiBe [51]. (Right) Melting points of the studied salts measured by freezing the type N thermocouple in the salt prior to density measurement.

The temperature measurements reported by the thermocouple (TC) have an error of ±2.2°C or 0.75% of the reported value in °C, depending on which value is larger; thus for the temperature measurements in this study, each measurement contains an implicit 0.75% uncertainty which is propagated across all three independent temperature measurements.

Validation of TC readings was performed by comparison to melting point of FLiBe observed during salt cooling curves, where the TC is frozen in the salt. We believe that the same TC was used for FNaBe and UZrFNaBe density vs. temperature measurements; though we note that chain of custody quality assurance was not applied to the TC, so we cannot exclude the possibility that other oven users replaced the TC in-between the two measurements.

To ensure thermal equilibration, the system was held at the targeted temperature for 40 minutes before measuring each data point to allow the system to fully reach equilibrium. The temperature inaccuracy due to thermocouple lag is negligible for this study: for the thermocouple used here, the reported time constant is approximately 6 seconds [88], and the difference in temperature of the environment from the temperature measured during a 5°C/min ramp with our thermocouple would be 0.5°C which is within the reported thermocouple error [89].

Density is computed from the measured ΔM at temperature, and the volume at temperature, computed from the calibrated bobber volume at 25 oC and the computed thermal expansion of stainless steel 316, α_{SS316}[90] (see Supplementary Data for the temperature-dependent α_{SS316}). Surface tension correction [51] on the mass difference is negligible (<0.003%) for the size of the bobber used in this experiment (100.7145g stainless steel 316). Thus, the density of the salt is computed as follows:

$$\rho_{salt}(T) = \frac{\Delta M_{salt}(T)}{V(T)}$$

$$V_{25℃} = \frac{\Delta M_{NIST}}{\rho_{NIST}}$$

$$V(T) = V_{25℃}[1 + 3\alpha_{SS316}(T - T_{25℃})]$$

$$\rho_{salt}(T) = \frac{\Delta M_{salt}(T)}{V(T)}$$

Equation 6

The error contributions to the measured salt density were: 0.3% due to variability between $V_{25℃}$ calibrations with the two NIST-certified density fluids; 0.3% due to uncertainty in thermal expansion of the stainless steel bobber; and between 0.04% to 0.13% due to ΔM_{salt} measurement noise over the measurements time, once thermally-equilibrated (see Supplementary Data for error propagation).

3.3.3 Viscosity

Viscosity experiments were performed using an Anton Paar Modular Compact Rheometer (MCR) 702e. In this experiment, the rotational viscosity method was used, utilizing a parallel plate measurement setup. For the rotational method, the shear stress τ (tau) was found by measuring the force of the salt's resistance to flow as torque and dividing by the surface area of the parallel plates. Then, using a known and preset shear rate $\frac{dv}{dt}$ or γ (gamma), recorded by dividing the rotational velocity of the upper parallel plate by the measuring gap height between the two plates, the dynamic viscosity μ (mu) was calculated by dividing the shear stress by the shear rate (Eqn. 5-7). Shear rate was kept at 50 s^{-1} in all experiments; this value was the instrument vendor recommendation for this plate diameter. The measuring gap height was kept at a constant value of 1 mm for all measurements.

$$\tau = \mu \frac{dv}{dt}$$

Equation 7

$$\tau\ (Shear\ Stress) = \frac{Force\ (F)}{Area\ (A)}$$

Equation 8

$$\frac{dv}{dt}(Shear\ Rate) = \frac{Velocity\ (v)}{Height\ (h)}$$

Equation 9

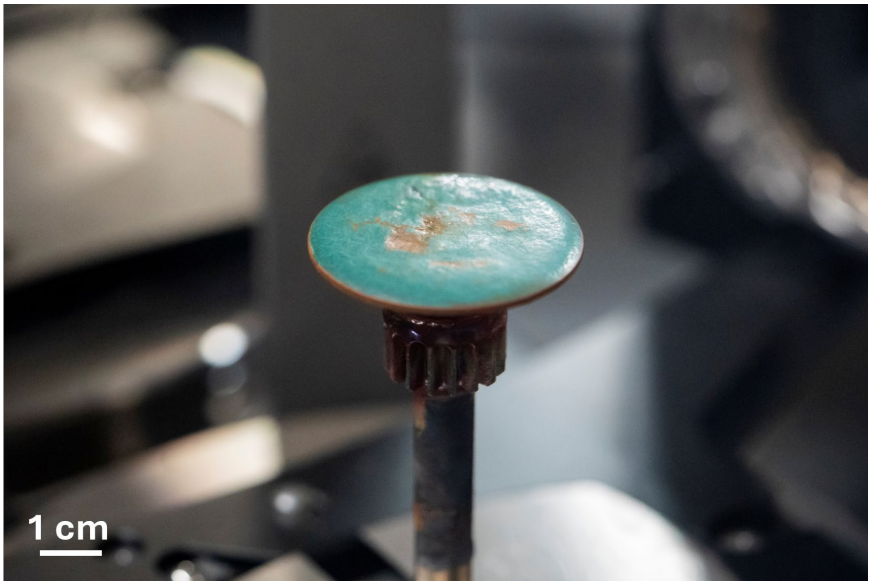

Figure 13. UZrFNaBe cooling on the lower parallel measuring plate after viscosity measurement. (Adam Lau/University of California Berkeley Engineering)

The measuring accessories used in this work were from Anton Paar Instruments. The upper and lower parallel plates had a diameter of 40 mm and are made from 316 stainless steel, while the shafts were made from Alloy 625 Inconel. The lower plate can be seen in Figure 13. The same plate set was used for all measurements, and in between salt samples, the salt is scraped off and then sonicated in water until no residue is visible and then wiped dry with Kimwipes; if the plates contain debris or are not flat and smooth, then viscosity measurements will be incorrect.

The salt sample is loaded at room temperature, then the clam-shell oven is closed and brought to temperature. The plates are brought to a distance of 1mm after the salt melts, and then the oven is opened while the salt is melted, to verify that no surface area of the measuring plate remained uncovered by the salt; excess sample coming off the plate is scraped with the scraper supplied by Anton-Paar. The oven is then closed and allowed to equilibrate at the temperature set-point for 2 minutes, and then the viscosity measurement begins. Temperature is then ramped at a constant rate of 2.3 C/min; if temperature ramp rates are too high, thermal equilibration is not achieved, and viscosity readings are incorrect. Supplementary data also includes a 15-minute temperature hold example for one of the samples, which illustrates viscosity variability with an isothermal hold, which in this study is lower than sample-to-sample variability. Figure 14 shows LiF_2BeF_4 (FLiBe) data, benchmarked against prior literature for this melt.

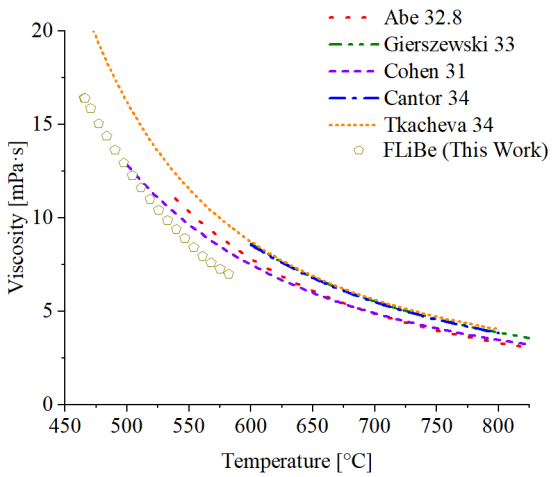

Figure 14. Viscosity benchmarking against prior FLiBe literature. x_{BeF_2} is indicated in the legend, for each reference; the expected x_{BeF_2} for this work is 33%. [80], [91], [92], [93], [94], [95]

To extract the activation energy of the viscosity of the salts measured in this work, the viscosity Arrhenius equation was used (Eqn. 8). This equation, slightly different from the typical Arrhenius equation due to the absence of a negative sign, is shown in Equation 10 where E_a is the activation energy of viscosity, A is the pre-exponential constant, T is the temperature in K, and R is the universal gas constant.

$$\ln(\mu) = \ln(A) + \frac{E_a}{RT} \qquad \text{Equation 10}$$

3.3.4 Sample Preparation & Handling

Salt storage, sample preparation, and experimentation took place inside of an argon glovebox with regulated oxygen and moisture levels. During salt storage, handling, and experimentation, oxygen and moisture levels were kept below 5 ppm and 0.1 ppm respectively. As radioactive depleted uranium and toxic beryllium are both health hazards, regular monitoring was completed to ensure levels remained below OSHA free release levels. Beryllium monitoring was completed through quarterly swiping of outer glovebox gloves, glovebox entrances, and general lab areas. Swipes were then sent out for digestions and analysis according to the OSHA ID-125G method. Of the 90 collected swipes over the data collection period, five were below 0.03 µg/100 cm^2 and 85 of them were below detection (<0.0071 µg/100 cm^2). In addition, air monitoring was performed during glove-box maintenance operations, and all 37 results were below detection (< 0.04 µg/m3 or lower, depending on air sampling volume for each sample). During glovebox maintenance operations, full-face or half-face respirators were worn with P100 respirator cartridges. For radiation monitoring, finger ring thermo-luminescent dosimeters were worn during rad salt handling and experimentation. Laboratory radiation monitoring was conducted using a Ludlum Model 26 Integrated Frisker, for in-glovebox surveys, and a ThermoFisher Scientific Radey B20 along with swipes analyzed by Perkin Elmer Tri Carb 290 TR Liquid Scintillation Analyzer for general lab surveys.

3.4 Results

3.4.1 Elemental Analysis & Melting Point

Results from the ICP-OES elemental analysis of FNaBe and UZrFNaBe are listed in molar percentages in Table 5. The UZrFNaBe salt sample measured in this work is from the same sample batch as Ref.[96] and the target composition of the originally prepared batch of salt was 72:16.5:11:0.5 NaF-BeF_2-UF_4-ZrF_4. Uncertainty was calculated on the UZrFNaBe sample using the error from volume additions during dilution and on the FNaBe sample using the propagation of the volume addition error and

the standard deviation of elemental analysis results.

Table 5. ICP-OES elemental analysis of FNaBe and UZrFNaBe

Sample	Digestion Efficiency (%)	X_{NaF}	X_{BeF2}	X_{UF4}	X_{ZrF4}	X_{GdF3}
FNaBe	93(2)	0.48(1)	0.52(1)			
UZrFNaBe	99	0.68(3)	0.21(1)	0.102(5)	0.0044(2)	0.00040(2)

3.4.2 Density

UF_4 and BeF_2 species have very different estimated molar volumes, reflecting the different ionic radii of the cations (0.27 Å for Be^{2+} and 1 Å for U^{4+} in ionic crystals) [97]. Density values including propagated uncertainty collected in this work using the hydrostatic method on the FNaBe and UZrFNaBe salts are shown in Figure 15 and compared against experimental literature values for similar composition salts; melting points measured by the OMEGA type N thermocouples used in this work are also shown. Ideal density calculated using molar volume additivity was calculated based on two different sources for the molar volume of NaF and BeF_2 single component melts: empirically estimated molar volumes [98] and high temperature experimental data [99]; other reported values of molar volumes and densities for NaF and BeF_2 can be found in Ref.[100].

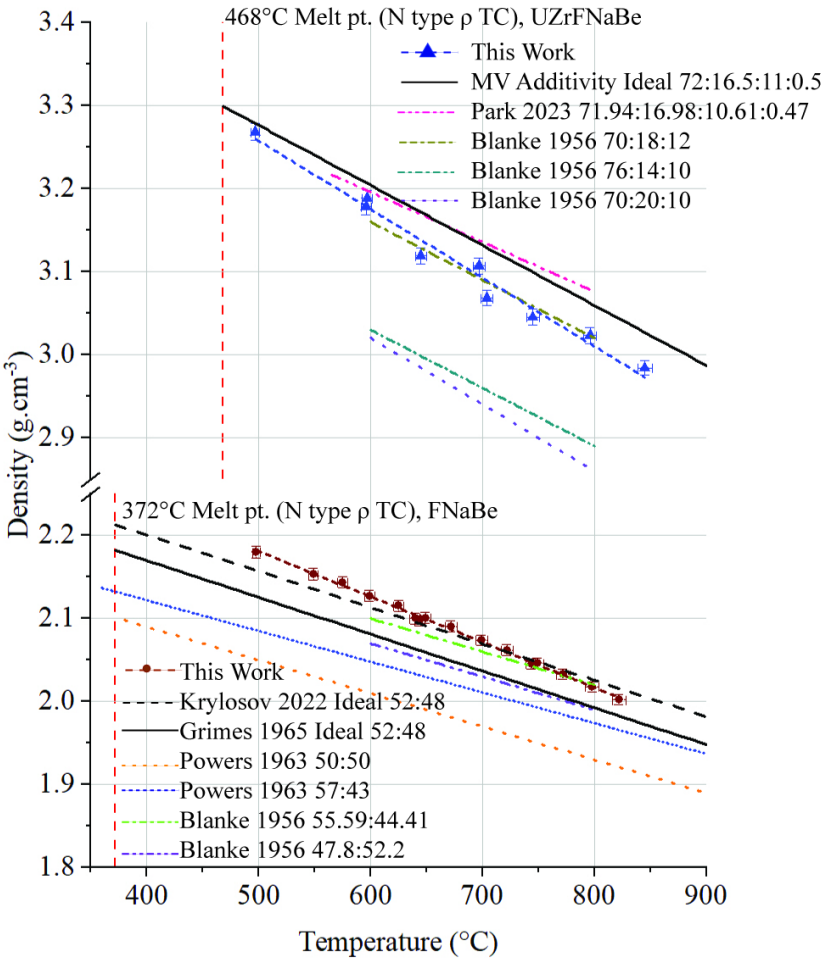

Figure 15. Density of FNaBe and UZrFNaBe salts measured using the hydrostatic method, compared to literature values of similar composition salts[96], [101], [102]. Comparison is limited to experimental work only and does not include modeling predictions.

A linear fit for the density of FNaBe and UZrFNaBe was calculated by performing a linear regression on the temperature dependent density data including propagated error for temperature and density using OriginPro v.10.0.0.154:

$$\rho_{FNaBe}\left[\frac{kg}{m^3}\right] = 2454(13) - 0.55(2) * T[°C], for\ x_{BeF_2} = 0.52(1), 372 \text{ to } 820\ °C$$

Equation 11

$$\rho_{UZrFNaBe}\left[\frac{kg}{m^3}\right] = 3670(30) - 0.83(5) * T[°C],$$
$$for\ x_{BeF_2} = 0.21(1), x_{NaF} = 0.68(3)\ x_{UF_4} = 0.102(5)\ x_{ZrF_4} = 0.0044(2), 480 \text{ to } 820\ °C$$

Equation 12

Thermal expansivity was calculated from the slope of the collected density values versus the temperature at which they were measured. Results are compiled in Figure 16.

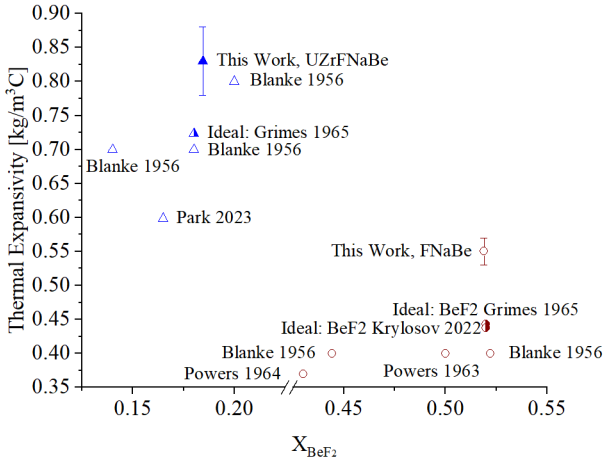

Figure 16. Thermal Expansivities of FNaBe and UZrFNaBe measured in this work, compared with thermal expansivities from literature[16], [29], [32].

3.4.3 Viscosity

3.4.3.1 Temperature Dependence

Viscosity was measured in range from 400–600 and 490–600 °C for the FNaBe and UZrFNaBe salts respectively. Data was collected in triplicate with three separate samples of each salt being taken from the bulk container of fresh salt. Uncertainty was quantified using the standard deviation of the three experiments. The resulting measurements are shown in Figure 17. Raw data including viscosity, shear stress, torque, time, and temperature for all viscosity runs are located in Supporting Information.

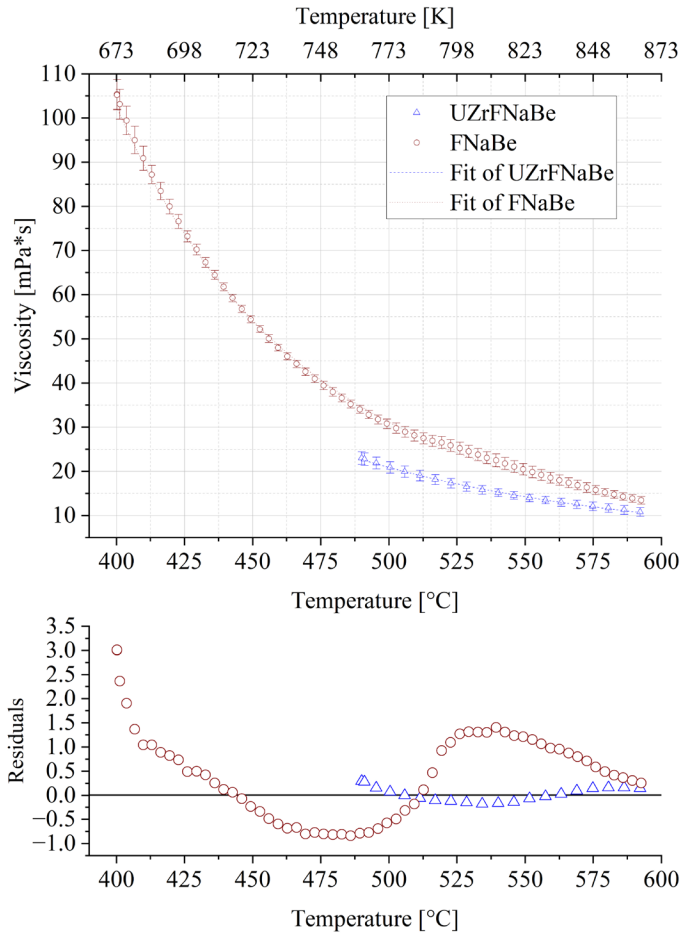

Figure 17. The viscosity of FNaBe and UZrFNaBe measured in this work using a 40 mm parallel plate rotational viscometer at 50 s^{-1} shear rate. Error bar is standard deviation across three runs on three different samples from the same salt batch.

3.4.3.2 Activation Energy

Temperature dependent viscosity values were collected for both salts and fit to Equation 10. The resulting fitted lines are shown in Figure 18. Then using OriginPro, a linear fit was applied to extract the measured activation energy of viscosity in the form of the slope and pre-exponential constant A in the form of the y-intercept. Values for the Equation 10 parameters E_a and A are located in Table 6.

.

Table 6. Activation energy of viscosity and pre-exponential constant values calculated for the viscosity measured in this work.

Sample Name	Temperature Range [°C]	A [mPa-s]	E_a [J/mol]
FNaBe	400-600	0.0103(8)	51,500(500)
	400-510	0.0071(9)	53,700(700)
	520-600	0.007(4)	55,000(5,000)
UZrFNaBe	490-600	0.05(2)	41,000(2,000)

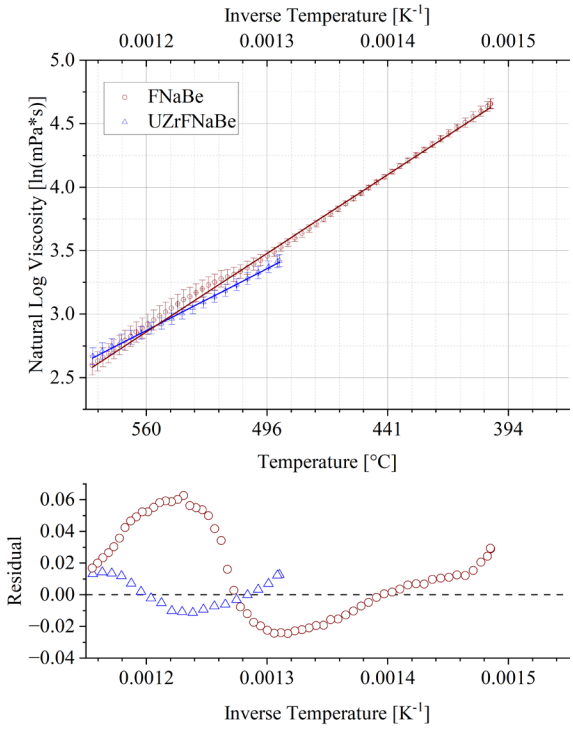

Figure 18. Activation energy of viscosity calculated of FNaBe and UZrFNaBe measured in this work using a 40 mm parallel plate rotational viscometer at 50 s^{-1} shear rate. Error bar is standard deviation across three runs on three different samples from the same salt batch.

3.5 Discussion

3.5.1 Variations in Molar Volume Additivity Calculation

The thermal expansion coefficient, β, is expressed as follows, from linear density functions:

$$\rho_{FNaBe}\left[\frac{kg}{m^3}\right] = 2454(13)\cdot\left(1-0.0224(8)\left[\frac{\%}{°C}\right]\cdot T[°C]\right), x_{BeF_2} = 0.52(1), 372 \text{ to } 820\ °C$$

$$\rho_{UZrFNaBe}\left[\frac{kg}{m^3}\right] = 3670(30)\cdot\left(1-0.0226(14)\left[\frac{\%}{°C}\right]\cdot T[°C]\right), x_{BeF_2} = 0.21(1)\ x_{NaF} =$$

$0.68(3)\ x_{UF_4} = 0.102(5)\ x_{ZrF_4} = 0.0044(2)$, 488 to 820 °C

Both the thermal expansion coefficient and the thermal expansivity $\rho\beta$ measured in this work for FNaBe and UZrFNaBe are higher than literature values (see Figure 16). The values predicted by the molar volume additivity model (see Figure 16) are higher than prior literature values and lower than the values measured here.

Two linearity assumption are possible for these single-component salts: either molar volume vs. temperature is linear, or the density versus temperature is linear. Using molar volume additivity with these two assumptions arrives at Eq. 13 and Eq. 14, respectively, for the temperature and composition dependence of the NaF-BeF_2 binary system. By taking the partial derivative with respect to temperature, $\left(\frac{\delta}{\delta T}\right)_{x_{BeF_2}}$, the slope of the ideal density, (i.e. the thermal expansivity) was computed, which remains a function of temperature and composition and is illustrated in Figure 19 (see equation in Supporting Information [103], [104]).

$$\rho_{NaF-BeF_2,v\ linearity}(x_{BeF_2}, T) = \frac{x_{BeF2}MW_{BeF2} + (1 - x_{BeF2})MW_{NaF}}{x_{BeF2}(0.004 * T + 21.2) + (1 - x_{BeF2})(0.0056 * T + 15.72)}$$

Equation 13

$$\rho_{NaF-BeF_2,\rho\ linearity}(x_{BeF_2}, T) = \frac{x_{BeF2}MW_{BeF2} + (1 - x_{BeF2})MW_{NaF}}{x_{BeF2}(\frac{MW_{BeF2}}{-0.0003 * T + 2.17}) + (1 - x_{BeF2})(\frac{MW_{NaF}}{-0.0006 * T + 2.56})}$$

Equation 14

Sensitivity of thermal expansivity with temperature and with composition is of engineering importance and is therefore discussed here. Both Equation 13 and Equation 14 predict a 2.5% change in thermal expansivity with +/- 2 mol% deviation from 52 mol% BeF_2. Equation 13 predicts 13% change in thermal expansivity between 400 and 800°C; Equation 14 predicts 1% change across the same temperature window; uncertainty in the experimentally measured constant slope is 4% for FNaBe and 6% for UZrFNaBe. Empirically, we would conclude that the assumption of linear density with temperature is more suitable than linear molar volume with temperature for the single-component salts. Future structural studies should investigate the structural reason behind this observed linearity.

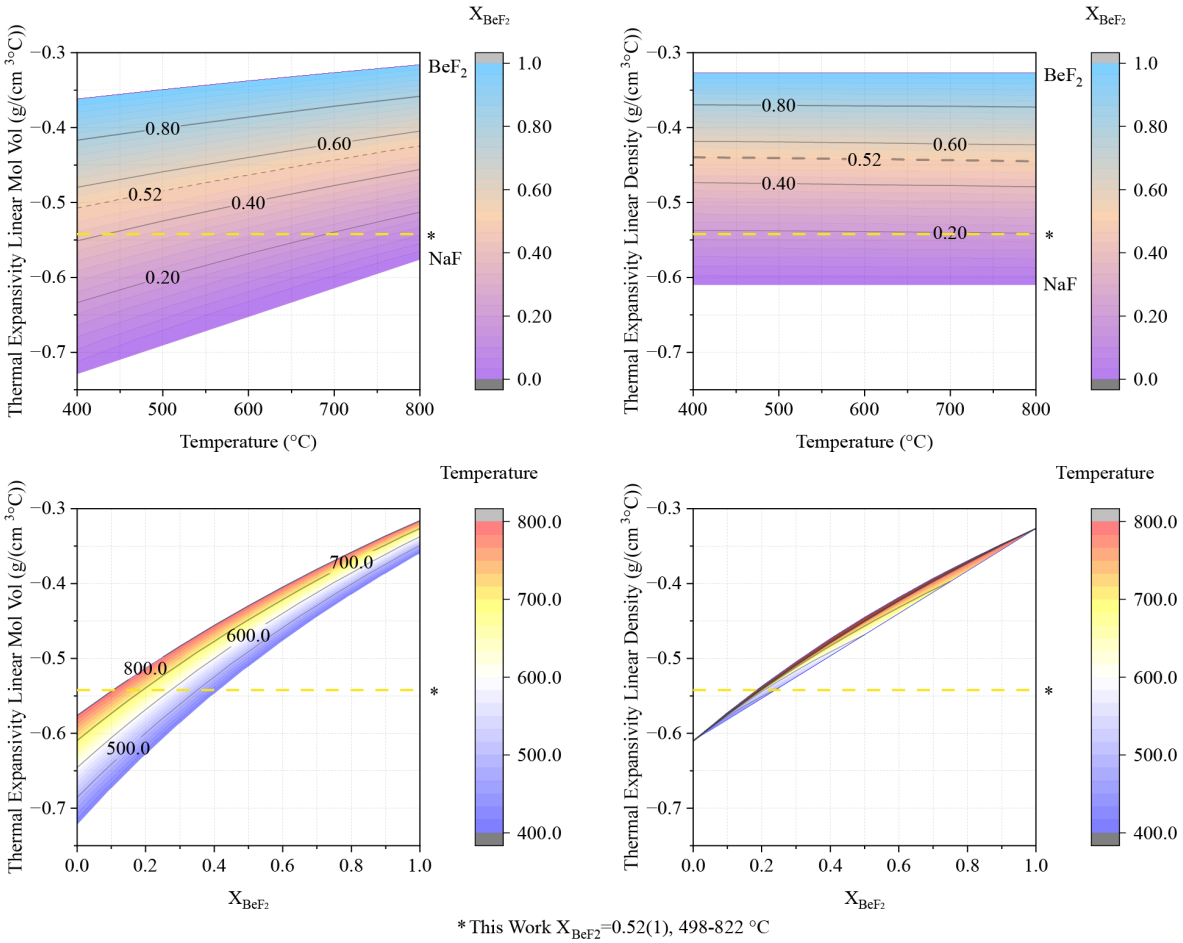

Figure 19. Ideal thermal expansivity of NaF-BeF_2 as a function of the molar composition and temperature assuming (Left) molar volume linearity or (Right) Density linearity.

3.5.2 Viscosity Temperature Dependence and Activation Energy Fitting

3.5.2.1 Two regions of FNaBe

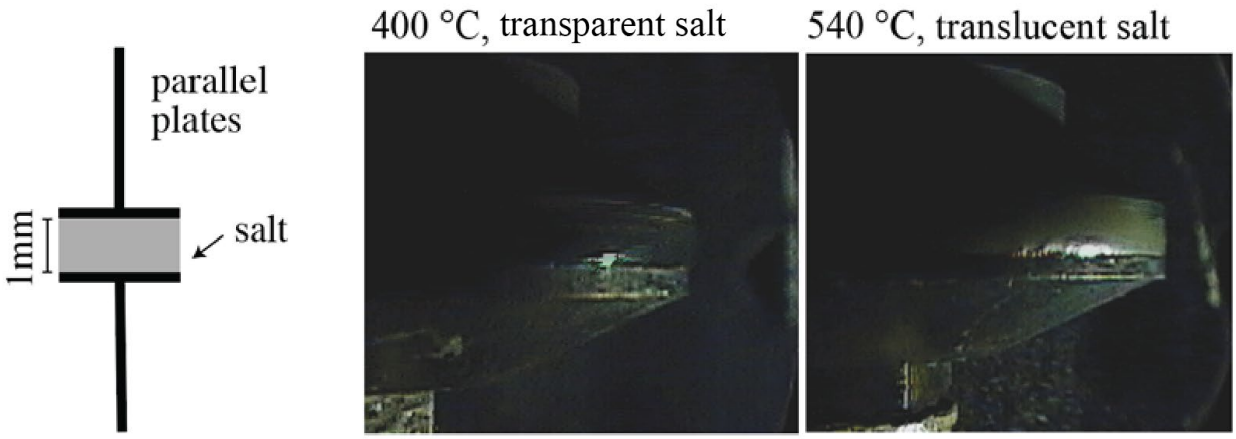

Figure 20. Image of FNaBe salt during parallel plate viscosity measurement at 400 and 540 °C.

During the temperature ramp for viscosity experiments, it was observed, using a high temperature camera located at the front of the viscometer oven, that at a specific temperature, there was a shift in the color of the salt visible between the upper and lower parallel plates as shown in Figure 20. The salt turned from a dark transparent fluid into a whitish translucent fluid. This shift can be seen in Figure 17 and Figure 18 at approximately 510-520°C. This alteration in the color corresponded with a slight change in the trends of viscosity vs temperature and the error bars increased. Between measurements gathered from 400-510°C and 520-600°C there was a 2.4% increase in the activation energy of viscosity as recorded in

Table 6. However, since the standard deviation error among the activation energy of viscosity measurements increased over 600% between the two temperature ranges, this increase in activation energy was deemed statistically insignificant. This shift behavior was observed in all three successive runs of three separate salt samples (data provided in Supplementary).

3.5.2.2 Degree of Polymerization Be vs U

A two region behavior has been previously observed in *ab initio* molecular dynamic simulations of LiF-BeF_2 melts: at low but not dilute BeF_2 concentration, from around 8 to 60 mol% BeF_2 the structural relaxation time of the Be-F network indicates that the mechanism of viscosity was due to diffusion of ions, while at high BeF_2 concentration the structural relaxation time of the network and the viscosity both increase and the viscosity scales linearly with the degree of polymerization [79].To test this hypothesized behavior, Figure 21 shows the activation energy of viscosity of this work compared alongside activation energy of viscosities of other fluoroberyllate melts, extracted from digitized studies on LiF-BeF_2, LiF-BeF_2-UF_4, LiF-NaF-BeF_2 titrations with two different x axes [80], [82], [101], [105], [106].

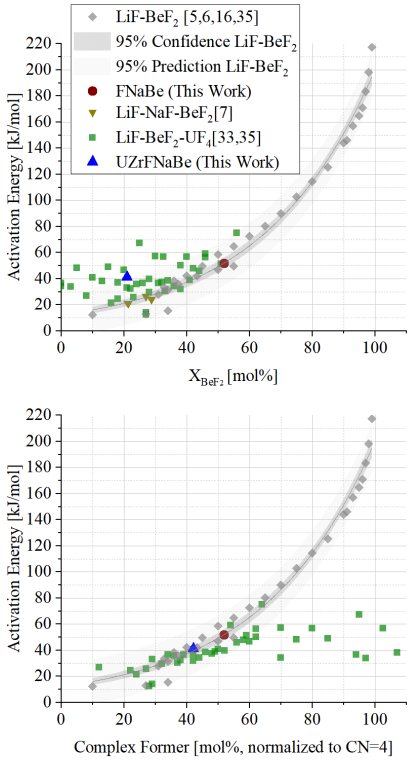

Figure 21. Activation energies of viscosity for FNaBe and UZrFNaBe compared to prior literature for activation energies measured from titrations of LiF-BeF_2, LiF-BeF_2-UF_4, and LiF-NaF-BeF_2 [80], [81], [82], [101], [105], [106], [107]. The logarithmic fit, confidence interval, and prediction interval of LiF-BeF_2 literature data [80] are overlayed.

The activation energies of viscosity for FNaBe measured in this work fits the trend of the LiF-BeF_2 data compiled and gathered by Ref. [80] at the same molar concentration of BeF_2. Thus, at this particular fluoroberyllate concentration studied, an effect of the nature of the weakly-coordinating cation (Li^+ vs Na^+) on the activation energy is not observed: the 7(9)% difference in activation energy is not statistically-distinguishable from zero [70]. This reinforces the modeling observations that there exists a concentration regime where the viscosity of the melt is decoupled from the diffusive motion of the non-complexing cation, and the structural relaxation processes are dominated by the fluoroberyllate structures [79]. Data from a

study on three LiF-NaF-BeF_2 melts is also included in Figure 21. This study is different from the other salts measured in this work and literature that are shown in Figure 21 in that it contains two weakly-coordinating cations. Further viscosity studies for the activation energy of various NaF-BeF_2 and NaF-LiF-BeF_2 titrations are necessary to fully determine whether this effect remains present across the compositional space.

To better compare the UZrFNaBe salt with this correlation, the uranium fluoride content was normalized to BeF_2 in the form a term called "molar percent complex former," where the concentration of complex forming species was counted on the basis of coordination with 4 fluoride ions. As molten U^{4+} has a U-F coordination number of 8 and Be^{2+} has a Be-F coordination number of 4, one UF_8^{4-} is counted as equivalent to two BeF_4^{2-} ions. The Zr^{4+} complex former content was calculated for coordination numbers ranging from 6 to 9 and the uncertainty included as x-axis error [86], [87]. Using this method, the activation of energy of viscosity of UZrFNaBe measured in this work here is compared to FNaBe and the LiF-BeF_2 and LiF-NaF-BeF_2 data in Figure 21 and found to follow the same trend with increasing complex former content, indicating that at this composition, the complex forming behavior of UF_4 results in similar effects as BeF_2[80]. Furthermore, data on LiF-BeF_2-UF_4 titrations from Ref. [101] (digitized and fit to Eqn. 10) also follow the LiF-BeF_2 trend, with a deviation of less than 1(4)% when logarithmically fit up to 60 mol% complex former.

However, as the UF_4 concentration in the melts increased and BeF_2 concentration decreased there is a notable decrease in the slope of the activation energy trend when compared to lower molar percentage complex former content [80], [105]. Based on the simulation cited in Ref.[79], the viscosity measurements in this work, and the LiF-BeF_2 and LiF-BeF_2-UF_4 titrations viscosity measurements, it can be hypothesized that at lower molar percentage complex former concentration, the small ionic species fragments such as UF_8^{4-}, BeF_4^{2-}, and $Be_2F_7^{3-}$ are the dominant mechanism of viscosity through ion diffusion [79], [80], [105]. Meanwhile, at high molar percentage complex former content, the behavior differs. For BeF_2, as the concentration increases, the activation energy of viscosity increases logarithmically due to the increase in the presence of long polymeric chains. Alternatively, UF_4 does not have the same viscosity behavior at high compound concentration, implying that while also a network forming compound, UF_4 does not have the same degree of polymerization as BeF_2.

In fuel solvents such as UZrFNaBe, potentially soluble fission products such as YF_3, LaF_3, CeF_3, SmF_3, have been estimated to be present in concentrations ranging from 2-4% each [108]. The addition of these species, with varying cation coordination numbers, have been noted to affect the structure and thermophysical properties of fluoride salts [82]. This work and its observation of previous literature has demonstrated that for the two complex forming species UF_4 and BeF_2, in concentrations less than around 60 molar percent complex former, the slope of the activation energy of viscosity vs composition remains constant. To confirm if this behavior remains present in salt in reactor conditions with solvated fission products, in addition to viscosity experiments with added fission products to measure the changes in the activation energy, calculated coordination numbers, confirmed by neutron or x-ray diffraction are necessary [20]. Potential methods to interpret the mechanisms behind the different polymerization behavior at high complex former content present in these molten salts include ab-initio molecular dynamic simulations to observe the behavior of various sized oligomer chains; high temperature NMR[109] or other spectroscopic methods to verify the predicted degree of polymerization, and oscillatory viscoelasticity studies to extract the complex shear modulus and measure the polymer crosslinking behavior in molten salts [20], [26], [79], [110], [111].

3.6 Conclusion

Density and viscosity and their temperature dependence were measured on two fluoroberyllate salts of relevance to molten salt reactor applications, and the connection between molecular structure of complexing ions and the observed thermophysical properties was discussed.

The equations describing the density as function of temperature for 52:48 NaF-BeF_2 and 70:18:12

NaF-BeF_2-UF_4 were calculated from experimental hydrostatic density measurements:

$$\rho_{FNaBe}\left[\frac{kg}{m^3}\right] = 2454(13)\cdot\left(1-0.0224(8)\left[\frac{\%}{°C}\right]\cdot T[°C]\right), x_{BeF_2} = 0.52(1), 372 \text{ to } 820\ °C$$

$$\rho_{UZrFNaBe}\left[\frac{kg}{m^3}\right] = 3670(30)\cdot\left(1-0.0226(14)\left[\frac{\%}{°C}\right]\cdot T[°C]\right),$$
$$x_{BeF_2} = 0.21(1) x_{NaF} = 0.68(3)\ x_{UF_4} = 0.102(5)\ x_{ZrF_4} = 0.0044(2), 488 \text{ to } 820\ °C$$

The error on density was under 0.5%, with the dominant contributions from the volume of stainless-steel bobber at temperature. Within the temperature range of measurements, the thermal expansivity was constant, to within 6% uncertainty. Consequently, for ideal mixture density predictions of these muti-component melts, empirically, we conclude that the assumption of linear density with temperature is more suitable than linear molar volume with temperature for the single-component salts. Future structural studies should investigate the structural reason behind this observed linearity.

Viscosity of the same salt samples was measured using parallel plate rotational rheometer:

$$\mu_{FNaBe}[mPa\cdot s] = 0.0103(8)\ e^{51.5(5)\ [\text{kJ/mol}]/RT[°C]};\ for\ 400 \text{ to } 600\ °C, \text{and shear rate } 50\ s^{-1}$$

$$\mu_{UZrFNaBe}[mPa\cdot s] = 0.05(2)\ e^{41(2)\ [\text{kJ/mol}]/RT[°C]};\ for\ 490 \text{ to } 600\ °C, \text{and shear rate } 50\ s^{-1}$$

Together with comparisons to prior literature measurements of titrations of LiF-BeF_2 and LiF-BeF_2-UF_4, it was hypothesized that, for the particular concentrations measured here, the diffusion of the weakly-coordinating cations (Na^+ or Li^+) did not dominate the mechanism of viscosity in the presence of larger UF_8^{4-}, BeF_4^{2-}, and $Be_2F_7^{3-}$ ionic complexes. Using the UZrFNaBe, FNaBe, and LiF-BeF_2 and LiF-BeF_2-UF_4 titrations, two regions of BeF_2 and UF_4 behavior were identified; a lower complex-former concentration region where the diffusion of the aforementioned ionic fragments is the dominant mechanism of viscosity and behavior is similar between UF_4 and BeF_2 (normalized for coordination number), and a higher network-former concentration region where the behavior differs between UF_4 and BeF_2.

4 STRUCTURAL EFFECTS OF ACTINIDES IN CHLORIDE SALTS

4.1 Chapter Summary

Actinides dissolved in a chloride salt, such as NaCl-UCl_3 eutectic melt, are to be used as nuclear fuel, and non-actinide-bearing chloride salts, such as NaCl-$MgCl_2$ or NaCl-KCl, are to be used as heat transfer fluids in molten chloride salt fast nuclear fission reactors (MCFR). Hence, assessment of reactor performance of these salts necessitates predictive capability for their thermophysical properties. Melting point, density, and viscosity of three chloride salt eutectics, NaCl-UCl_3, NaCl-KCl, and NaCl-$MgCl_2$ are measured. Melting point variability in literature was >20°C, potentially attributable to lack of appropriate temperature calibration standards for salt differential scanning calorimetry (DSC) samples, or compositional variability of the prepared melt; comparison between DSC data on 50 mg samples and cooling-curve data in 10-gram samples points towards the latter. NaCl-UCl_3 density variability in literature was 8%, potentially attributable to variability in uranium mol% and uranium oxidation state; ± 2.5 mol% UCl_3 or 5 mol% $U^{4+}/(U^{4+}+U^{3+})$ can lead to 5% density variability; the non-uranium binary melts studied here would exhibit less density variability with composition, did not have the possibility of multiple oxidation states, and literature variability of their densities is <1%. In viscosity measurements, when comparing activation energies of the three binary mixtures, the rate of increase of the activation energy of viscosity with increasing non-NaCl content is aligned with the Mg^{2+} and U^{3+} complex ion formation and polymerization behavior observed by prior diffraction studies, and for K^+ indicates that it forms a weaker coordination than the Na^+ cation.

4.2 Introduction & Background

As previously stated in Chapter 1, with rising energy needs, the necessity of the development of nuclear energy as economic and resilient energy source is evident. To support the design and construction of sustainable, cost effective, safe, and proliferation resistant advanced nuclear reactors, the Generation IV International Forum (GIF) was established[2]. Chloride salts are potential fuel solvents and coolants of Molten salt reactors (MSR's), a proposed Generation IV advanced nuclear reactor class. Several companies such as TerraPower, Southern Company, Moltex Energy, and Elysium Industries have utilize molten chloride salts as fuel solvents in their reactor concepts.[112] These reactors, denoted Molten Chloride Fast Reactors (MCFRs), contain two salt loops; a primary loop of fissile material containing fuel salt which is pumped through the reactor core, and a secondary unfueled salt loop as which is an intermediate heat exchanger between the fuel salt and a tertiary fluid[113], [114]. Chloride salts, alternatively from commonly studied fluoride molten salts, are desired due to their lower supply costs and high actinide solubility[112], [115].

However, several of the thermophysical properties for these salts such as density, melting, point and viscosity range in value across experimental studies, or not currently available in literature for certain temperature ranges. For engineering scale reactor modeling as well as atomistic ab-initio molecular dynamic simulations of chloride salt systems, thermophysical properties are necessary to measure and validate studies of molten salt behavior[28], [116], [117]. This work seeks to experimentally provide viscosity and density of an actinide containing NaCl-UCl_3 eutectic primary loop salt using oscillatory and rotational rheology and the hydrostatic method respectively, as well as to propagate error and establish the bounds of the uncertainty of this measurement using NaCl-KCl eutectic and NaCl-$MgCl_2$ eutectic heat transfer salts[118], [119].

The thermophysical properties of various chloride salt systems have been examined for nuclear applications throughout literature. Single-component salts (such as NaCl, $MgCl_2$, $BaCl_2$, and KCl) have been experimentally studied for their density and melting point; due to their high melting points, these are not suitable for molten salt reactor fluids[120], [121], [122], [123], [124], [125], [126], [127], [128]. Binary and ternary chloride salts have been proposed as candidate coolants and fuel solvents; a large variation exists in the reported thermophysical properties of chloride melt mixtures [112], [113], [115], [128].

Viscosity mechanisms in fluoride salts have been identified to be correlated to their ionic structure [79], [80], [129]. Molten chloride as well as molten fluoride salts form ionic complexes around the strongly-coordinating cations[79], [80], [129]. Some of the strongly coordinated ionic complexes can also form polymeric ions by sharing of halide ions between two strongly coordinating cations. The distribution and branching of these polymeric anions will be specific to each cation combination in the melt. Since viscosity can increase with increased polymer length, polymer branching, and polymer concentration, different cation mixtures will result in varying viscosities and temperature and composition dependence of viscosity. Through diffraction studies as well as simulations, UCl_3 in salt melts has been identified to be a strong complex former[130], [131], [132], [133]. It also forms U-containing polymeric species, which in increase in length as the UCl_3 concentration in the melt increases[130], [131], [132], [133]. Similar complexing behavior has also been observed in UF_4 salt melts[84], [134]. In sodium-uranium chloride melts multiple regions of viscosity have been identified based on different UCl_3 content[129]. Based on the activation energy of viscosity, it was observed that as UCl_3 content increases in the melt up to 80 molar percentage the viscosity also increases. This is attributed to the structure inside changing from being dominated by ionic fragments such as $NaCl_4^{3-}$, UCl_5^{2-}, and UCl_6^{3-}, to then viscosity being dominated by uranium dimers at higher concentration, to finally being dominated by all uranium complexes consisting of chains of multiple uranium atoms. Above 80 molar percentage UCl_3, the viscosity and its activation energy decreases with increased U^{3+} concentration, attributed to the large uranium structures breaking down[129]. Magnesium in molten NaCl-$MgCl_2$ has also been noted to be a complex former by neutron and x-ray diffraction studies, however interpretation of this diffraction data using molecular dynamic simulations have observed only dimers of magnesium cations and no higher order polymers[135]. In contrast, chain formation of NaCl and KCl in molten chloride melts has not been observed in molecular dynamics simulations of NaCl- or KCl-containing systems[136], [137]; thus the NaCl-KCl binary is not expected to be chain-forming

Complex formation has been correlated to density in molten salts. Modeling of the non-ideal mixing of chloride salts have observed that salt ternary systems containing complexing salts result in higher non-ideal density behavior than ternaries containing cations that coordinate to a lesser extent[138]. Using Redlich Kister modeling fitted to binary NaCl-KCl, NaCl-YCl_3, KCl-YCl_3, and NaCl-UCl_3 experimental data to extrapolate empirical predictions of ternary compositions, this reference demonstrated that ternary melts containing UCl_3 such as KCl-NaCl-UCl_3 have a significantly higher excess molar volume than non-UCl_3 containing ternary systems and theorized that this lower density and higher molar volume was caused by the formation of $[UCl_n]^{n-3-}$ chains[138]. An experimental study compared measured and molar volume additivity molar volumes NaCl-UCl_3 system and also observed a positive excess molar volume with a maximum near the eutectic compositional point which then began to decrease as the UCl_3 concentrations was increased[129]. This study attributed this excess molar volume to the formation of complex uranium dimer species[129]. However, another simulation study using molecular dynamic studies did not reproduce this behavior and instead computed a negative excess molar volume[130]. As there is more simulation-to-simulation variability as well as experiment-to-experiment variability among studies performed on composition-dependent measurements of excess molar volume in NaCl-UCl_3 literature, than the magnitude of excess molar volume, comparison among studies of different composition to determine excess molar volume is not possible to date.

In previous studies, a method was demonstrated to calculate the ideal molar volume and ideal density of a binary salt mixture using the molar volume additivity of its individual components[51]. As Excess molar volume quantifies the difference between mixture and single-component molar volume,[51] experimental densities of NaCl, KCl, $MgCl_2$, and UCl_3 melts were converted to molar volumes using their molar masses[124], [126], [139], [140]. Then by taking the molar volumes at two temperatures, taking their weighted average based of their molar ratios in the eutectic salt, and extrapolating the trendline down to the desired measuring temperature range, the ideal density was calculated. The molar mass of UCl_3 used for

ideal density calculation was 344.39 g/mol which assumed the isotopic ratio of uranium present was the natural enrichment.

The goal of this work is to provide the values and propagated uncertainty of the thermophysical properties of three chloride fuel and coolant salts with constituents of varying complexing behavior from their melting point to 800°C, contrast the differences in the melting point, density, and viscosity to determine information regarding error ranges of measurements, and to observe the mechanisms of the internal structure of chloride molten salt and its effect on thermophysical properties. Unlike prior studies, this work also completed multiple sets of property measurements on the same salt sample under the same measurement conditions allowing for further characterization of each composition including calculation of kinematic viscosity.

4.3 Methods

4.3.1 Radiation Safety

4.3.1.1 In-glovebox Surveillance

Depleted uranium, which contains less than 0.7 wt.% of the isotopes ^{235}U and ^{234}U and primarily consists of ^{238}U, has a specific activity of around 0.33 μCi/g[141]. Finger ring thermos-luminescent dosimeters were worn to measure the quarterly dose for radioactive salt experimentalists. Samples were handled in gloveboxes to prevent inhalation and skin irritation. To ensure that materials leaving the glovebox did not have radioactive surface contamination, a Ludlum Model 26 Integrated Frisker was used monthly to survey the glovebox train and confirm that the readings inside were less than 2 times the background.

4.3.1.2 Laboratory Surveillance

General laboratory surveillance was completed using two methods: handheld detectors and swipe self-surveys. Monthly, radiation levels were measured using these methods in high use laboratory areas including but not limited to, entrances, outer surface of gloveboxes, ventilation, fume hoods, computers, and work benches. Handheld surveys were completed using a ThermoFisher Scientific Radeye B20 survey meter and swipes were analyzed using a Perkin Elmer Tri Carb 2910 TR Liquid Scintillation Analyzer to ensure that laboratory operation levels were less than 2 times the background.

4.3.2 Sample Preparation

Salt storage, sample preparation, and measurement took place inside LC Technology negative pressure argon gloveboxes with monitored oxygen and moisture levels. During sample preparation and experimentation, oxygen was kept below 5 ppm and moisture below 0.1 ppm. Non-experimental measurement salt manipulation took place on nickel 200 alloy sheets as shown in Figure 22.

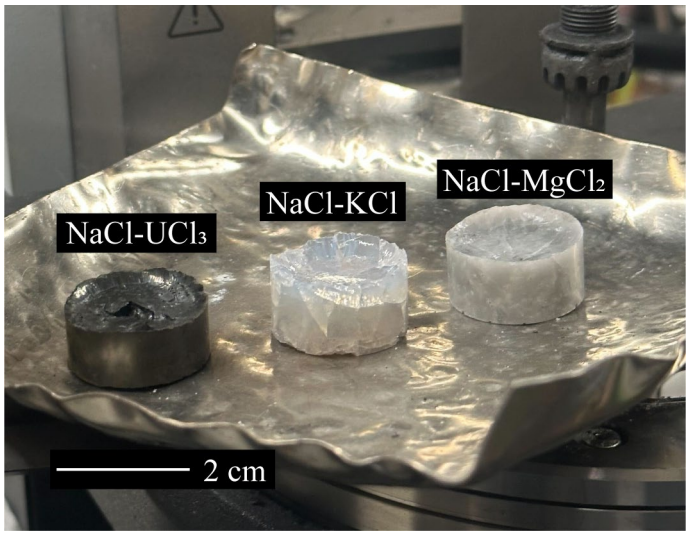

Figure 22. (From left to right) Frozen $NaCl\text{-}UCl_3$, NaCl-KCl, and $NaCl\text{-}MgCl_2$ salt pucks on a nickel 200 alloy sheet after rheology measurement.

4.3.3 Elemental Analysis

Elemental analysis was completed by first using a CEM SP-Discover 80 Microwave Digester System to digest salt samples of approximately 50 mg in a solution of dilute Nitric acid. After 1 hour at the digestion temperature of 160 °C and visual inspection to ensure full digestion, a Perkin Elmer 5300 DV Inductively Coupled Plasma – Optical Emission Spectroscopy (ICP-OES) was used to analyze the molar compositions of the samples. Digestion and analysis were completed in triplicate for uncertainty propagation and to ensure repeatability, with three separate samples of each salt being analyzed, using Texas Scientific Products ICP Standards for Na, K, Mg, and U to form a calibration curve. Composition was calculated using the measured molar ratio of Na to the other binary component (K, Mg, U), with error determined from the standard deviation of the molar compositions of the three separate samples. Raw ICP-OES counts data and calibration curves can be found in Supplemental Information.

4.3.4 Differential Scanning Calorimetry

Thermogravimetric-differential scanning calorimetry (TG-DSC) was performed on a Setaram ThemysONE thermal analyzer to measure transition temperatures and enthalpies of salts. The comparison of heat flux between a reference crucible and sample crucible was conducted by the instrument to calculate relative changes in heat within the sample, as detected by a type S thermocouple on the DSC, and mass changes were recorded by the instrument's microanalytical balance. The Setaram software Calisto was used

for data acquisition and processing. The open instrument and its sample plate are shown in Figure 1.

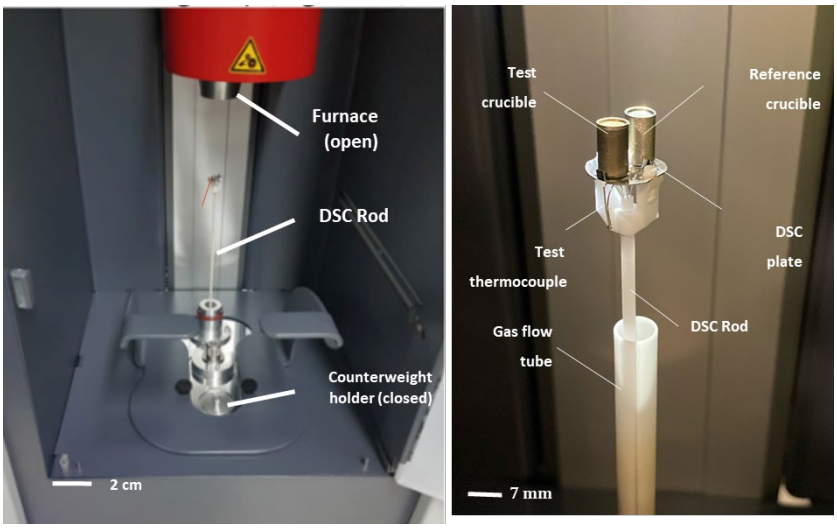

Figure 23. (Left) inside of the DSC chamber with the furnace raised for sample loading. (Right) Sample holder with crucibles loaded for before measurement. Note that alumina crucibles were used in thermocouple calibration and not depicted here.

The ThemysONE DSC thermocouples and heat flow sensors imaged in Figure 23, were calibrated with PJLA-certified metal standards (prepared and measured by Engineering Analytics Laboratories, measurements provided in supplemental data) in alumina crucibles (Setaram). Following ASTM E794-06 (melting point determination protocol) and Setaram documentation on metal calibration, melting and freezing events were calculated using Calisto Data Processing software using spline approximations. For each standard, raw melting point and specific heat measurements were collected for scan rates (SRs) of 5,10, and 15 ºC/min with no carrier gas flow. Comparing the standards' raw measurements with the PJLA-certified measurements, calibration coefficients were produced for temperature and heat flow corrections:

$$T_{corr} = -6.812366 - 0.01568499 \cdot T - 0.01929801 \cdot R$$

Equation 15

The instrument was used in an Argon atmosphere glovebox (H_2O < 0.1 ppm, O_2 < 5 ppm) such that the highly hygroscopic nature of chloride salts would not lead to reactions or modifications of the salt composition. Sample crucible preparation involved taring the crucible in glovebox, spooning in 50-100 mg of salt into the crucible, capping the crucible with its lid, and carefully transferring the crucible to the DSC chamber. Platinum-rhodium crucibles (Setaram) and lids were used to contain the sample and the reference in each chloride experiment.

A heating profile was programmed to thermally cycle the sample between melting and freezing three times. An initial pre-melt step was programmed to heat the sample to 50 ºC above its apparent melting point and cool to 50 ºC below its melting point, after which the furnace was set to oscillate between these set points for three cycles, with ten-minute isothermal holds at the two boundaries for heat flow stabilizations. The pre-melt was heated and cooled at a SR of 10 ºC/min while the consecutive three cycles heated and cooled at 5 ºC/min. No cover gas was used. All standard and chloride sample temperature and heat flow measurements are included in the Supplemental data.

4.3.5 Density

Density was measured in this work using the hydrostatic method as described in previous

literature[51], [134]. The setup consisted of a nickel bobber suspended from a Pheonix GH-252 analytical balance using metal wire, and a glassy carbon crucible (SPI Supplies) containing salt inside of a Watlow full cylinder ceramic fiber furnace; the set-up is shown in Ref.[134]. The same bobber and glassy carbon crucible were used for all measurements. The bobber was cleaned between salts using water and Kimwipes, and the glassy carbon crucible was cleaned using Ghost Wipes and Kimwipes.

Temperature was controlled and monitored using a Type K ungrounded omega thermocouple connected to a DIN Universal High-Performance Controller PID. Once the desired temperature was reached and the system had equilibrated for ten minutes, the bobber (Nickel 200 Alloy, Special Metals) was then lowered into the furnace using an OMEGA electronic lift and submerged into the salt. The mass difference was then measured in intervals of 1 second for a total duration of 60 seconds.

The Type K thermocouple (0.125 in diameter, 6 in sheath length, TJ36-CAIN-18U-6-SB-SMPW-M, DwyerOmega) was calibrated using the melting point of pure NaCl (Los Alamos National Laboratory). NaCl melting point offsets were measured by freezing the thermocouple in the molten salt and recording the cooling curve, then corrected using PID software in successive trials until the melting point measured was ±1 °C from the literature value[142]. As reported by the vendor, the uncertainty on the temperature measured by the thermocouple was 0.75% of the measured temperature value in degrees Celsius. The dominant source of error of the density method used in this work was the uncertainty on the bobber volume at room temperature.

Melting point offset compared to differential scanning calorimetry (DSC) of the type K density thermocouple are measured by freezing the thermocouple in the molten salt inside the glassy carbon crucible. Salt was allowed to air cool in the furnace and the temperature was recorded to measure the extent of supercooling and to identify the temperature at which phase change was observed. Cooling curves and estimated melting points are shown in Figure 24.

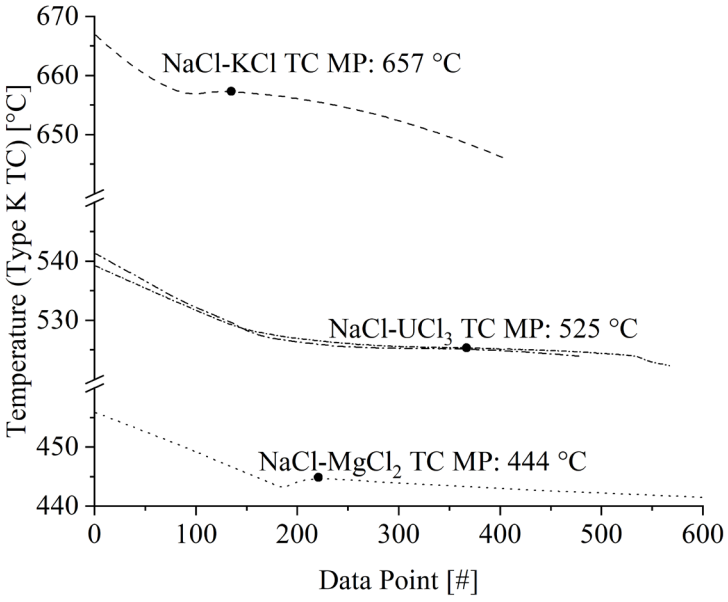

Figure 24. Cooling curves measured prior to each density measurement by the type K thermocouple immersed in the molten salt, while salt is cooling from liquid to solid state.

Error propagation on liquid density measurements includes uncertainty on: the coefficients of thermal expansion of the bobber, temperature of the bobber, the bobber volume at room temperature, the

surface tension at room temperature and high temperature of the salt and the calibration fluid on the wire, and salt temperature determined from the thermocouple temperature readings. Linear fitting parameters for liquid density versus temperature propagate both measurement error on liquid density and measurement error on salt temperature, using the x-error and y-error linear fitting function in OriginPro 2025b[51], [104].

Molar volume additivity predictions were based on linear extrapolations of density as a function of temperature for single-component salt melts, evaluated at 600 and 800 °C. The choice of density linearity versus molar volume linearity was discussed in Ref.[134].

4.3.6 Viscosity

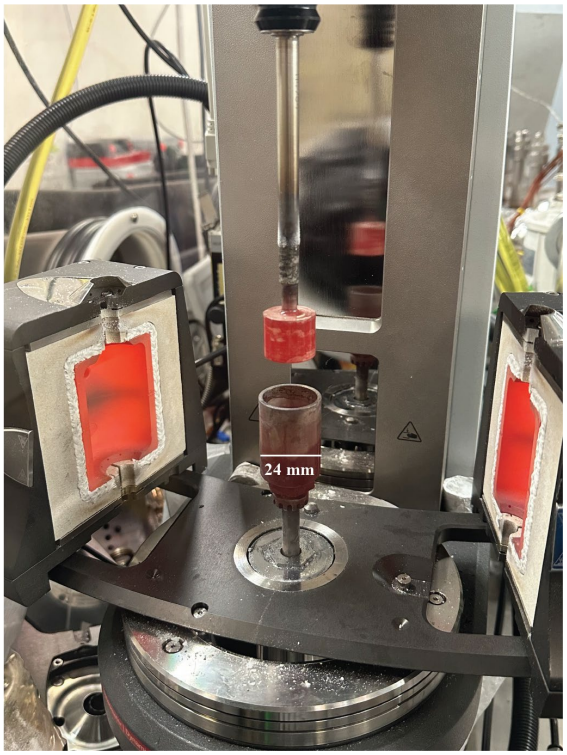

Figure 25. Image of rheometer with inconel cup and bobber attached located inside of the argon glovebox post NaCl--KCl salt measurement.

Temperature dependent viscosity was measured in this manuscript using an Anton Paar Modular Compact Rheometer (MCR702e) with a cup and bobber measuring setup as shown in the schematic in Figure 25. Measurement took place inside of an Inconel measuring cup located on a shaft inside of a convection oven capable of reaching 1000°C. Rheometer viscosity calibration was completed using Cannon Instrument Company S600 viscosity standard silicone oil. Salt was loaded into the measuring cup as a homogeneous powder and then heated to temperature under Argon cover gas. Once at temperature, an Inconel measuring bobber, suspended from an air bearing using an Inconel shaft, slowly lowered into the molten salt. After temperature equilibration, a rotational period of 2 minutes by the bobber and upper shaft was completed to remove excess air bubbles and ensure temperature and sample homogeneity. After this period, rotational viscosity measurement was completed on each salt from 10 °C above the thermocouple measured melting point to 800 °C through isothermal, constant shear experiments. The shear rate for all experiments was held constant at 50 s^{-1}. The dominant source of uncertainty in the viscosity data analysis was identified to be the fitting errors of the Arrhenius viscosity equation.

4.4 Results

4.4.1 Elemental Analysis

The elemental compositions measured by ICP-OES, of the salts studied in this work, are shown in Table 7. Percentage recovery was calculated using a calibration curve and the initial sample mass digested. Uncertainty was calculated from the standard deviation of the elemental analysis results. NaCl-UCl_3 percentage recovery of 96(2)% was calculated assuming 100% UCl_3 and 0% UCl_4.

Table 7. Experimental Chemical Sample Table: Sources and compositions of the salts used in this work, digested in triplicate and measured by ICP-OES

Sample	CAS No. & Chemical Components	Supplier	Elemental Analysis Method	x_{NaCl} [mol %]	Run ID	Percentage Recovery (%)
NaCl-KCl	NaCl:7647-14-5 KCl:7447-40-7	Oak Ridge National Laboratory (NaCl: Fisher Scientific, KCl: Sigma Aldrich)[143]	ICP-OES	50.1(8)	1	95.0
					2	97.0
					3	94.0
NaCl-UCl_3	NaCl: N/A (Internal TerraPower) UCl_3: N/A (Internal TerraPower)	TerraPower	ICP-OES	65.1(8)	1	96.4
					2	98.5
					3	94.1
NaCl-$MgCl_2$	NaCl: N/A (Internal TerraPower) $MgCl_2$: N/A (Internal TerraPower)	TerraPower	ICP-OES	58.7(8)	1	92.3
					2	98.2
					3	99.0

4.4.2 Differential Scanning Calorimetry

Characterization of the three salts measured in this work was completed through elemental analysis by ICPOES and melting point determination by DSC. Figure 27 contains a compilation of melting points, molar compositions, and measurement methods for previous studies characterizing NaCl-KCl, NaCl-$MgCl_2$, and NaCl-UCl_3 eutectic salts. Based on the phase diagram for NaCl-KCl provided in Ref.[144] the NaCl-KCl is located at 50 molar percent NaCl. For NaCl-$MgCl_2$ the targeted eutectic point has been measured to be 58.5 molar percent NaCl[145], [146]. Finally, in NaCl-UCl_3 using differential scanning calorimetry, the eutectic composition was measured to be 66 molar percent NaCl[115]. A compilation of phase diagrams from prior literature is shown in Figure 26.

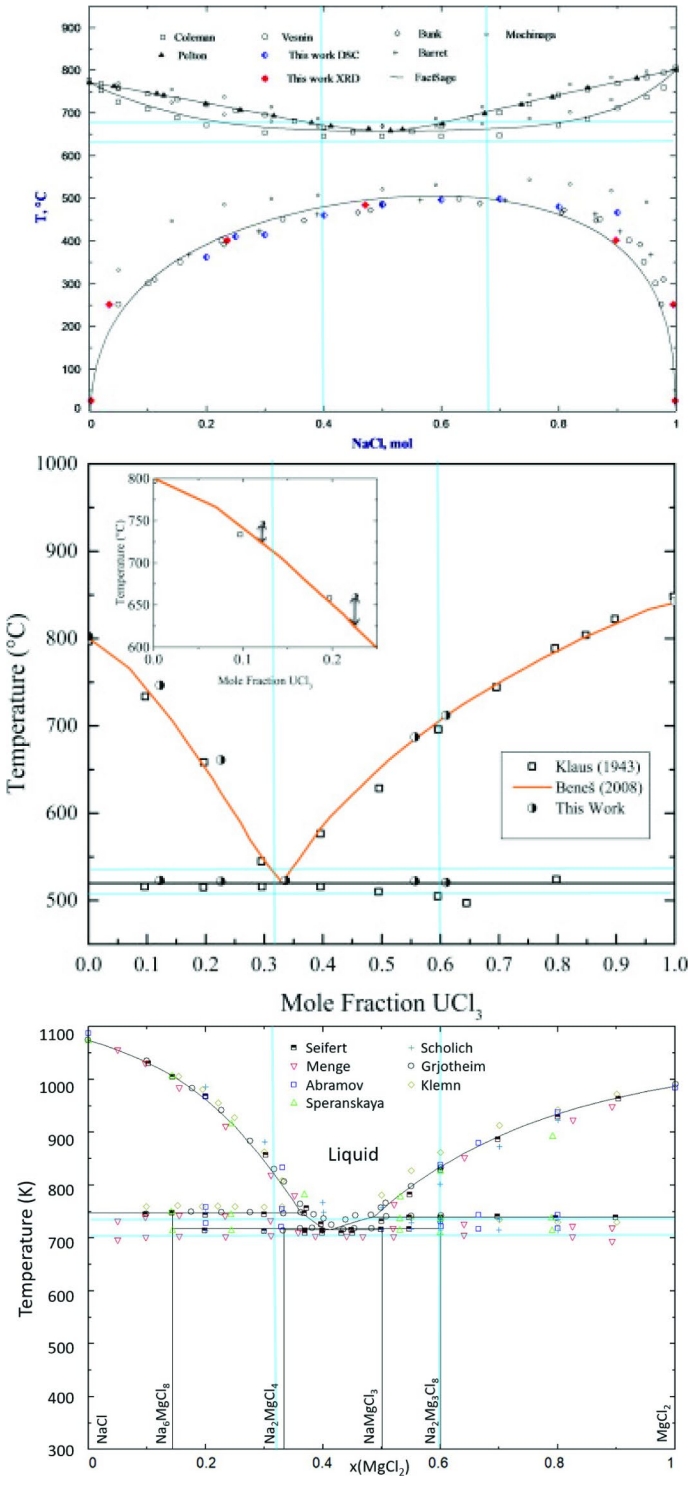

Figure 26. Phase Diagrams of the NaCl-KCl, NaCl-UCl_3, and NaCl-$MgCl_2$ binary systems.[115], [144], [146]

The salt samples analyzed in Table 1 are further characterized regarding their solid-liquid transitions using DSC, as shown in Table SI-4. A full DSC test report with masses, cycling ranges, melting, and freezing points can be found in Supplemental Information. Melting point was also measured using the type K thermocouple (TC) used for temperature control during density experimentation. The TC was immersed in the salt, the salt was allowed to cool until frozen, and temperature of the TC was measured as a function of time. As the binary melts exhibited supercooling, the melting point was determined at the location of zero slope on the temperature vs. time plot. For all three melts, the melting point determined by the two independent methods were within one standard error of each other, with methods, calibration standards, and scale of experiment (50 mg vs. 50 g) being different and independent.

Supercooling behavior was observed, by both DSC and TC, in MgCl2-NaCl, UCl3-NaCl, and KCl-NaCl (Table 9).

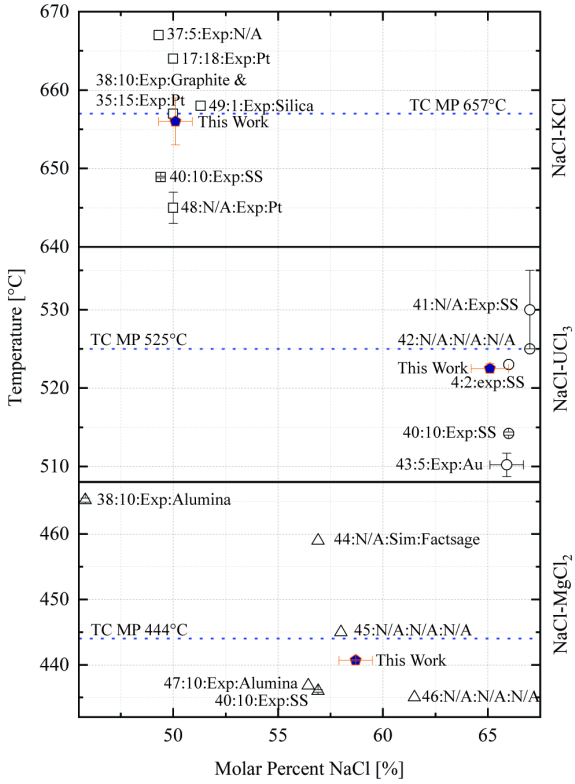

Figure 27. Melting points of binary chloride salt mixtures studies in this work measured by DSC and the type K thermocouple used for density work, and comparison to literature values. [Legend: Source, Heating Rate (°C/min), Experimental/Simulation, Crucible Material][115], [127], [144], [147], [148], [149], [150], [150], [151], [152], [153], [154], [155], [156], [157], [158], [159]

4.4.3 Density

Figure 28 and Figure 29 show the experimental densities measured in this work, prior literature

data for these binaries, and ideal mixture densities predictions calculated by molar volume additivity.

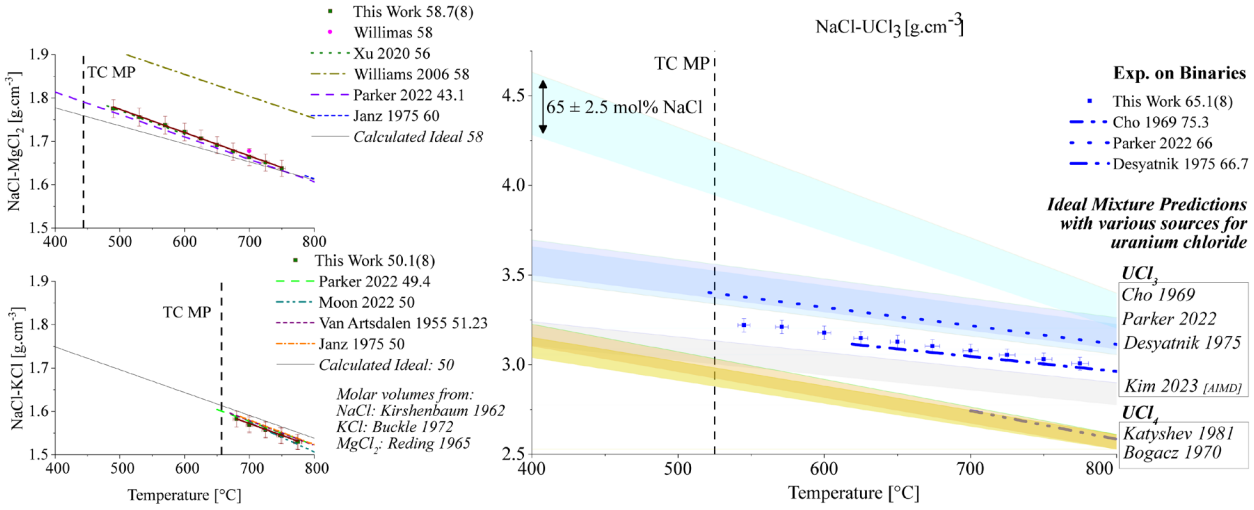

Figure 28. Densities of chloride salts measured in this work, experimental literature, and ideal values and value ranges calculated using molar volume additivity. (Top: NaCl-$MgCl_2$. Middle: NaCl-UCl_3. Bottom: NaCl-KCl). The ideal densities were calculated using the compositions measured by this work. Graphs are annotated with type K thermocouple measured melting points[124], [126], [129], [139], [140], [150], [155], [157], [160], [161], [162], [163]

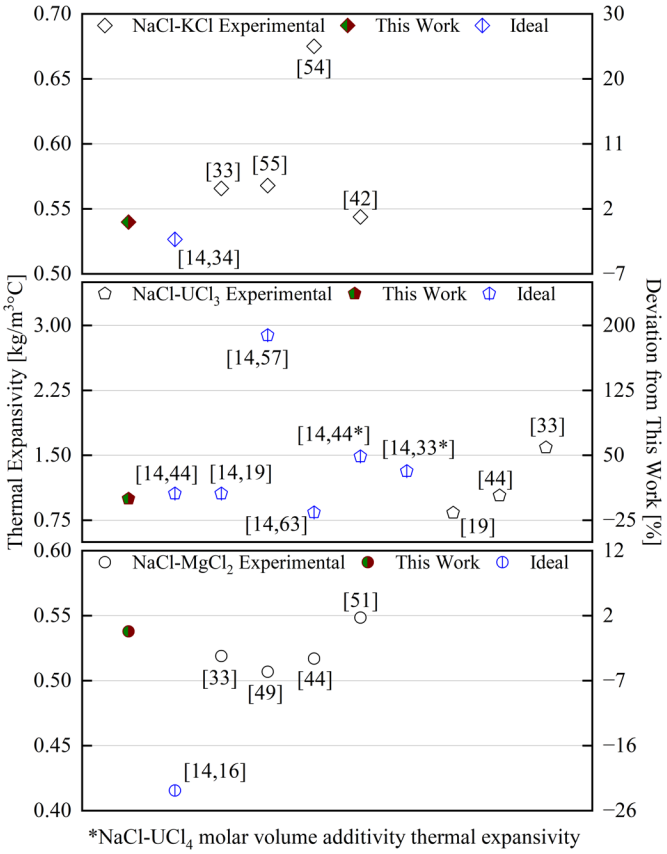

Figure 29. Thermal expansivities of the salts studied in this work compared with literature values. [124], [126], [129], [139], [140], [150], [155], [157], [160], [161], [162], [163]

4.4.4 Viscosity

Viscosity data was collected in increments from 10 °C above their type K thermocouple measured melting point to 800 °C. For each measured temperature, 10 data points were collected for statistical analysis. For the NaCl-$MgCl_2$ isothermal experiments, instrument error caused two data point measurements to report values outside of the fitted trend error bars. To verify that these two isothermal measurements were correctly omitted, a temperature ramp viscosity experiment was completed and found to not fall outside the measured error ranges of the corrected isothermal data experiment. All data including omitted points can be found in Supplemental information. The average values, standard deviation, and Arrhenius fits for viscosity at each measured temperature are shown in Figure 30. The activation energies of viscosity (E_a) and the pre-exponential constants (A) are shown in

Table 8.

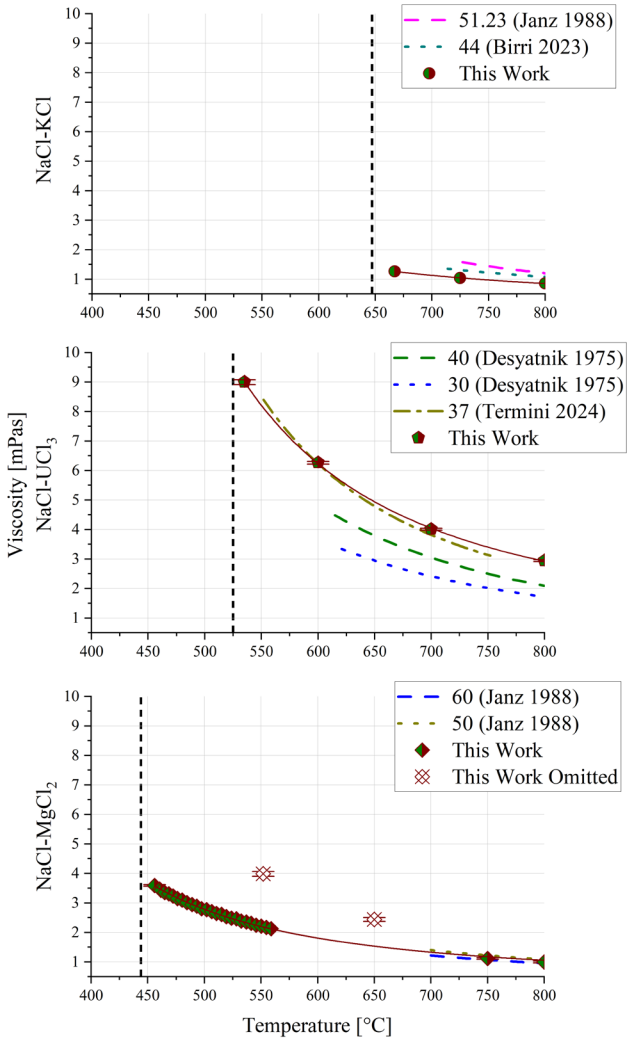

Figure 30. Viscosity of each studied salt with Arrhenius fit. Graphs are annotated with type K thermocouple measured melting points[129], [139], [164], [165]

Table 8. Measured ranges, Activation energies of viscosity, and pre exponential fitting constants for the salts measured in this work.

Sample Name	Temperature [°C]	A[mPa*s]	E_a [J/mol]
NaCl-KCl	667-800	0.05(1)	25,000(2,000)
NaCl-UCl_3	535-800	0.092(4)	30,700(300)
NaCl-$MgCl_2$	454-800	0.059(2)	24,800(200)

4.5 Discussion

4.5.1 Salt characterization

Thermocouple offset calibration was completed on NaCl (Los Alamos National Laboratory) until the temperature reading during freezing was ±1 degree of the NIST standard melting point of 801°C[142]. The melting point measured by DSC was consistently below the thermocouple couple measured melting points for all three studied salts. As shown by Figure 24 and Figure 27, the offsets measured were 1(3) °C for NaCl-KCl, 2.5(6) for NaCl-UCl_3, and 3.3(1) for NaCl-$MgCl_2$, indicating that the farther from the calibration point a reading took place, the larger the offset increased. However, across the studied ranges the largest offset recorded was 3.3(1) °C, validating the provided vendor uncertainty for the couple which has a maximum of 6 °C. Stock type K thermocouples are vendor-calibrated using an ice bath, the freezing point of a known metal such as Tin, or a dry block calibrator, however the calibration points of these methods are far beneath the experimental range of this study[166]. Density data collection at high temperature can be affected by a drifting thermocouple, consequently changing the slope of the experimentally collected density values, (i.e., changing the measured thermal expansivity). For the present density measurements, high temperature thermocouple calibration resulted in a larger offset at low temperatures but only to a maximum value of 5 °C.

Experimental melting points from literature revealed no correlation between measurement variation and experimental conditions such as heating rate, crucible containment, and method, as shown in Figure 27. Reported values may vary based on other factors, from environmental to compositional to analytical. Environmental conditions such as oxygen content may induce compositional changes and thus melting point differences. As shown in Table 9, using the binary phase diagrams, based on the propagation of 2.5 mol% error at the measured eutectic points, the sensitivity of composition on the liquidus was compared to the overall literature liquidus variation in the same compositional range. The sensitivity of the liquidus points of the NaCl-$MgCl_2$ and NaCl-UCl_3 binaries exceeded the literature uncertainty in this range indicating the possible effect of compositional error on melting point variability. While most studies are performed in Argon gloveboxes, few report oxygen content in the cover gas: chloride salts, when in the presence of oxygen in the cover gas, are known form oxides and possibly corrode the container, with solvated oxides and corrosion product metal cations possibly affecting the melting point of the 50 mg DSC sample with 1 cm^2 surface area[167]. Analytical calibrations, which are dependent on the metal-crucible combinations used in producing a calibration curve, may yield different melting temperatures. For studies including details on DSC or DTA calibrations, most authors used a different crucible for metal standard calibrations than what is used for salt measurement, which may lead to inaccurate melting point corrections depending on the thermal differences of the two crucible materials[115], [127], [144], [147], [148], [149], [150], [150], [151], [152], [153], [154], [155], [156], [157], [158], [159]. To further characterize and compare systemic factors affecting salt melting point measurements, systematic studies comparing melting point determination techniques and experimental conditions are necessary, as demonstrated by a recent round-robin study on chlorides and fluorides [143]. In this work, there is consistency observed melting point measurements using the thermocouple and the DSC on the same salt sample in the same measurement environment, providing confidence in the analytical methods employed here.

Table 9. Summary of calorimetry data, and prior literature variability

	MP, °C						Super-cooling, °C	Super-cooling, °C	x_{NaCl}
	DSC	err[(a)]	TC	err[(b)]	Lit. Var. Range (<+/-2.5 mol% comp. variability)	Liquidus Sensitivity to +/- 2.5 mol% at the eutectic[115], [144], [146]	DSC (10°C/min cooling)	TC in salt	
NaCl-KCl	656(3)	0.5%	657(5)	0.75%	3% (n=8)	1%	< 6	<0.5	50.1(8)
$NaCl$-$MgCl_2$	440.70(13)	0.03%	444(3)		2% (n=5)	7%	10.1(2)	~1.5	58.7(8)
$NaCl$-UCl_3	522.5(6)	0.1%	525(4)		4% (n=5)	6%	12(1)	<0.1	65.1(8)

(a) variability among runs, at the same temperature ramp rate
(b) TC reading uncertainty

4.5.2 Density

The equations for density for the salts measured in this work were measured to be as follows.

$\rho_{NaCl-UCl_3}\left[\frac{g}{cm^3}\right] = 3.77(1) - 9.7(2) \times 10^{-4} T[°C]$ for Na(mol%)=65.1(9), 545-775 °C, depleted uranium

$\rho_{NaCl-MgCl_2}\left[\frac{g}{cm^3}\right] = 2.053(5) - 5.42(7) \times 10^{-4} T[°C]$ for Na(mol%)=58.7(8), 490-750 °C

$\rho_{NaCl-KCl}\left[\frac{g}{cm^3}\right] = 1.967(7) - 5.5(1) \times 10^{-4} T[°C]$ for Na(mol%)=50.1(8), 680-775 °C

Equation 16

Ideal density was calculated using the molar volumes of end-member constituents. For the density of the end member single components, NaCl, KCl, and $MgCl_2$[124], [126], [140], agreement among prior studies within 2% is observed. However, when gathering UCl_3 molar volumes from literature experimental studies of UCl_3 density using the hydrostatic method, UCl_3 unit cell volumes extracted from molecular dynamic simulations of KCl-UCl_3, and UCl_3 density using neutron imaging, variation was observed among reported values[129], [139], [150], [163], [168]. Consequently, this variation can be observed in the calculation of the NaCl-UCl_3 ideal densities shown in Figure 28. At 700 °C, the variability among the ideal densities for NaCl-UCl_3 calculated with different UCl_3 molar volumes was 13% (n=4). The variability among experimental density measurements near the eutectic (+/- 0.8 mol%) was 8% (n=3)[129], [139], [150]. In comparison, for NaCl-$MgCl_2$ and NaCl-KCl, the variability among experimental density measurements were 0.5% and 0.2%, respectively. The NaCl-$MgCl_2$ calculation incorporates the experimental data from Ref.[139], [150], [157] and does not utilize the molar volume additivity based calculation modeling data from Ref.[128]. To visualize the effect of compositional uncertainty on the molar volume additivity ideal density predictions, the ideal trendlines were calculated and displayed as bands in Figure 28, which gives the prediction range for the composition range of 65 ± 2.5 mol% NaCl. This illustrative compositional variability is based on the range of compositions reported for experimentally prepared NaCl-UCl_3 melts that targeted the eutectic melting point determination (experiments compiled in Figure 27). Using the Ref.[150] UCl_3 data as an example case to calculate the sensitivity of density to composition, ± 2.5 mol% variability leads to 5% predicted density variability and 5% thermal expansivity variability, exceeding the experimentally-observed variability in the density of the binary (n=3). This indicates that, for uranium-containing melts, compositional sensitivity of the liquid density must remain as

a top consideration in error propagation and sensitivity analysis of salt liquid density and thermal expansivity values that are used for engineering and safety analysis calculation of systems that employ these salt mixtures. This sensitivity is not as pronounced for the non-uranium melts studied here, NaCl-KCl (0.1% difference in density, and 0.2% difference in thermal expansivity) and NaCl-MgCl2 (0.3 % difference in density, and 3% difference in thermal expansivity), since the difference in the density and thermal expansivity of the two constituents is not as pronounced as density differences between actinides (i.e. UCl_3) and NaCl.

The sensitivity to redox potential of the binary mixture containing uranium chloride should also be considered for its effect on the liquid density of the mixture, since soluble uranium can exist as both U^{4+} and U^{3+} in chloride melts and the redox potential will shift the ratio of the two oxidation states of uranium present in the melt. The target oxidation state of uranium in the binary melt was UCl_3, however the presence of UCl_4 post salt synthesis has also been observed by electrochemical open circuit potential measurments[169]. UCl_4 can be introduced by the synthesis process of uranium chloride; for example, Ref.[169] synthesized UCl_3 from Uranium metal by reaction with molten iron chloride, then used electrochemical techniques to measure the UCl_4/UCl_3 activity ratio to be in the range of 0.0025 to 7.6×10^{-7}, depending on the standard reference potential used[169]. UCl_4 can also be present in the NaCl-UCl_3 fuel salt system due to contamination with oxidants (e.g. Cr^{3+}, air, moisture), as measured in similar uranium-containing chloride melts[169], [170].

UCl_3 and UCl_4 have different densities[139]. Conceptually, the ionic radii are 1.81 Å for Cl-, and 1.03 Å for U^{3+} (six-fold coordination), and 1 Å for U^{4+} (eight-fold coordination); the volume of the chloride anions dominate the volume of the melt, and UCl_4 molar volume would be expected to be about 30% higher than that of UCl_4, corresponding to 20% higher density of UCl_3 than that of UCl_4[97]. This is a highly idealized approximation that does not account for changes in open space among the ions in the melt. Measurements of UCl_4 and UCl_3 liquid density report 30% higher density for UCl3, evaluated at 800 °C, noting still the uncertainty in redox potential of these single-component melts[139]. Thus the sensitivity to UCl_3/UCl_4 ratio or the redox potential of the melt, on the density of the salt mixture warrants evaluation[139].

This density difference is illustrated in Figure 28. The calculated ideal density bands of the composition measured in this work ± 2.5 mol percent, denoted Ideal Katyshev 1981 and Ideal Bogacz 1970, created using the UCl_4 density data compiled in Ref.[139], [150] results in a lower density and lower thermal expansivity than the experimentally measured values in this work as well as calculated ideal density bands using literature UCl_3 density values. To further investigate the possible redox effect, using the NaCl, UCl_3, and UCl_4 data measured in Ref.[124], [150], the sensitivity of UCl_4 on the density of a uranium fuel salt was calculated using the molar volume additivity method[134] at the Na:U ratio of 65.1(8):34.9(8), the formation of 1, 5, and 10 mol% UCl_4 in the UCl_3 melt resulted in a ~1, ~5 and ~11% lower melt density, and a ~0.2, ~1, and ~3% lower melt thermal expansivity respectively as compared to the 0% UCl_4 base case. Thus, the 8% variability that has been observed thus far among the literature density measurements for the NaCl-UCl_3 eutectic melt could be explained by an unintended UCl_4 content in the binary, of the order of magnitude of 8 mol% UCl_4.

The variability in volar volume additivity predictions of density with redox potential is bounded by using in one set of cases the UCl_3 density, and in another set of cases the UCl_4 density. Figure 28 illustrates an up to 30% effect of oxidation state on the 65± 2.5 mol% NaCl binary melt; Figure 28 also illustrates an up to 20% variability among different single component data sets for the same oxidation state of uranium.

The redox effect of fission in an uranium chloride fuel salt is not yet known, due to unknow redox dependence of the oxidation state of the fission products in the fuel melt[8]. Multiple methods of redox measurement and control in molten chloride fast reactor systems have been proposed[171], [172]. As demonstrated by the data in Ref.[139], in the design and operations plan of an MCFR system, the tolerances necessary for monitoring and control of the UCl_4/UCl_3 ratio should also be informed by the acceptable

thermophysical property variability in the fuel. For example, the performance of passive safety systems that rely on natural circulation in the fuel system, for the purpose of decay heat removal, will scale linearly with the thermal expansivity of the fuel: 30% decrease in thermal expansivity of the liquid fuel corresponds to 30% decrease in the rate of heat removal by the natural circulation-based decay heat removal system. The total uranium inventory in the critical core will also scale linearly with the fuel density. In summary, a combination of ±2.5 mol% compositional variability in the NaCl-UCl_3 composition or a ± 8 mol% variability in mol% $U^{4+}/(U^{4+}+U^{3+})$ could both feasibly be responsible for the observed NaCl-UCl3 variability of 8% for density (n=3). Future evaluation should examine both phenomena to understand their relative contributions to the alterations in the density and thermal expansivity and to further disambiguate between the effects of the two.

Table 10. Summary of density data, and prior literature variability

	Density				Thermal expansivity				
	Measurement Density Overall Uncertainty at 700 °C [kg/m3]	Measurement Relative Uncertainty of Density at 700 °C [%]	Density Variability at 700 °C Literature [%]	Density Variability Mol.Vol.Add (<+/-2.5 mol% range) [%]	Measurement Thermal Expansivity Overall Uncertainty at 700 °C [kg/m3-°C]	Measurement Thermal Expansivity Relative Uncertainty at 700 °C [%]	Measurement Thermal Expansivity Relative Uncertainty at 700 °C Omitting Bobber Volume Uncertainty [%]	Thermal Expansivity Variability Literature [%]	Thermal Expansivity Variability Mol.Vol.Add (<+/-2.5 mol% range) [%]
NaCl-KCl	0.02	1	0.2 (n=4)[139], [150], [160], [161]	0.1	2×10^{-4}	2	2	10 (n=4) [139], [150], [160], [161]	0.2
NaCl-$MgCl_2$	0.02	1	0.5 (n=4)[119], [139], [150], [157], [160]	0.3	8×10^{-5}	2	2	3 (n=3) [9,33,44,51,5]	3
NaCl-UCl_3	0.04	1	8 (n=3)[129], [139], [150]	5	2×10^{-4}	2	2	34 (n=3) [129], [139], [150]	5
Note: sources of error considered: the coefficients of thermal expansion of the bobber, temperature of the bobber, the bobber volume at room temperature, the surface tension at room temperature and high temperature of the salt and the calibration fluid on the wire, and salt temperature determined from the thermocouple temperature readings.									

The relative uncertainty on the thermal expansivity in this work at 700 °C is reported in Table 10 with and without the propagation of the bobber volume uncertainty at room temperature. As the bobber volume uncertainty at room temperature is the dominant error in this work and is not a temperature dependent quantity, for calculation of the error of the slope of the density trendline, it should not be included.

4.5.3 Viscosity Comparison

The Arrhenius equations for viscosity of the salts measured in this work were:

$\mu_{NaCl-UCl_3}[mpa\cdot s] = 0.085(9)\times e^{\frac{31{,}300(800)}{R*T[K]}}$ for Na(mol%)=65.1(9), 535-800 °C, 50 s^{-1}, depleted uranium

$$\mu_{NaCl-MgCl_2}[mpa \cdot s] = 0.059(2) \times e^{\frac{24{,}800(200)}{R*T[K]}}$$ for Na(mol%)=58.7(8), 454-800 °C, 50 s^{-1}

$$\mu_{NaCl-KCl}[mpa \cdot s] = 0.053(5) \times e^{\frac{24{,}700(700)}{R*T[K]}}$$ for Na(mol%)=50.1(8), 667-800 °C, 50 s^{-1}

Equation 17

A linear fit for each binary is performed on data from the prior study that measured compositional-dependent viscosity. Data points from other studies at unique compositions are superimposed on this plot, for comparison (Figure 31). Further analysis is necessary regarding the compositional dependency of the activation energy of viscosity in chloride melts, however across the compositional ranges measured in prior literature shown in Figure 31, the rate of increase of the activation energy with increasing non-Na cation content (i.e. Mg^{2+} or U^{3+} or U^{4+}) corresponds to oligomer observations by prior literature[129], [130], [131], [132], [133], [135], [136], [137]: The strong complex forming cation U^{3+} has been modeled to form dimers, trimers, and tetramers at concentrations between 10 and 40%, and a complex polymer network above 40%[130]. This follows the observations made by Ref.[129] of the viscosity of UCl_3 containing melts being driven by the size of the uranium complexes present at a certain composition. Mg^{2+} in $MgCl_2$-NaCl chloride melts has also been observed to be a strong complex forming species but has been observed to form only dimers[135]. Ref.[134] compared to molten salt species present in a melt normalizing to a known coordination number (CN). In this work, a melt containing NaF, ZrF_4 and UF_4, with CNs of 8, and BeF_2, with a CN of 4, were characterized by normalizing their activation energy of viscosity as a function of composition to the CN of 4. By observing the differences in slopes of titrations of melts containing these species, this work determined that the increase in viscosity measured when adding increased quantities of strong complex formers constituents was not only due to the varying size of ionic complexes resulting from different CNs, but also the extent to which these complexes formed oligomeric chains (the degree of polymerization). The CN of U^{3+} in UCl_3 containing melts has been reported to have a value ranging primarily from 6 to 8[130], [131], [132], [133], and the CN of $MgCl_2$ has been reported as 4[135].

When applying this method to the complexing forming salts in this work, and normalizing to the Mg^{2+} CN of 4, it is observed that at ~40%-equivalent CN, the activation energies for the magnesium and uranium complex does overlap, indicative of viscosity dominated by concentration of strong-coordinated bonds. Above 40% (i.e. 40 mol% MgCl2 of CN=4, 20 mol% UCl3 of CN=8), the rate of increase of the activation energy of viscosity vs mol percent non-NaCl is not fully captured by just the difference in CN. The U^{3+} CN is 1.5 to 2 times larger than the Mg^{2+} CN depending on the value selected[130], [131], [132], [133], [135]. The slope of the compositional dependent activation energy of viscosity for NaCl-UCl_3 and NaCl-$MgCl_2$ is 170(30) E_a/mol% and 70(20) E_a/mol% respectively, a multiplication factor of 2.5, larger than the difference between coordination numbrs. This helps to validate the observations shown in Ref.[129], [134] that beyond 40 mol% UCl3, the viscosity of molten salts containing complex forming species depends on the degree to which these species form oligomeric chains, increasing the viscosity of the melt and its activation energy, beyond what would be expected based on number of strongly coordinationated bonds alone.

Neither Na+ and K+ are expected to form strong complexes[136], [137]. For NaCl-KCl, the activation energy increases with increased concentration of KCl, indicating either that KCl might form stronger associations than NaCl, or that a mechanism other than complex ion formation dominates viscosity for this particular binary melt; this is not an entirely surprising observation, considering that in fluoride salts, K^+ is predicted to form stronger associations than Na^+[28]. What is perhaps surprising is that the activation energies in the KCl-NaCl binary are higher than those of the $MgCl_2$-NaCl binary, a complex former; this would indicate either that K^+ is a stronger complex former than Mg^{2+}, or that a mechanism unique to K^+ may be contributing to viscosity, which cannot be fully captured by the concepts of complex ion formation.

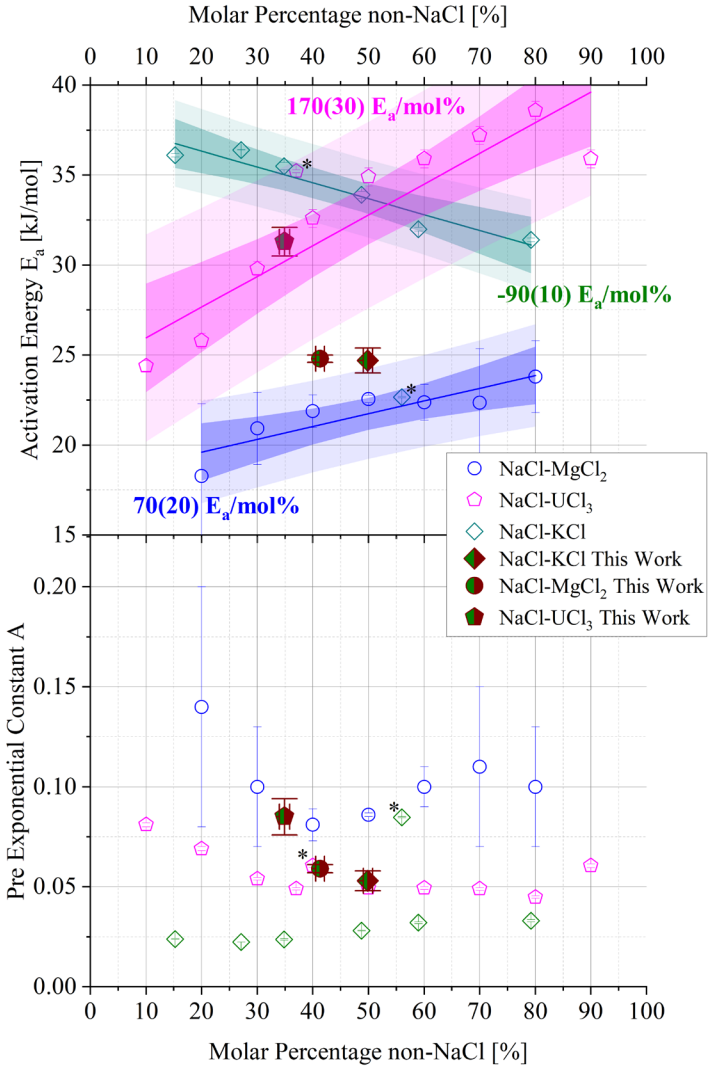

*Singular data point from Ref[58,59]. Linear fits calculated from compositional dependent data in Ref.[19,33]

Figure 31. Experimental activation energies of viscosity and pre-exponential constants from Arrhenius fitting of viscosity[129], [139], [164], [165]. Linear fits, confidence, and prediction bands are based only on Ref.[129], [139], excluding the data points marked with an asterisk.

Using the hydrostatic density and dynamic viscosity collected in this work, the following equations for the kinematic viscosity behavior NaCl-UCl_3, NaCl-$MgCl_2$, and NaCl-KCl were generated. Measurement uncertainty from density and viscosity is error-propagated in the calculation of kinematic viscosity data points, and then a fit is performed, with the error reported accounting both for fit error and measurement uncertainty of the underlying data.

$$\nu_{NaCl-UCl_3}\left[\frac{mm^2}{s}\right] = 0.036(2) \times e^{\frac{28{,}600(300)}{R*T[K]}}$$ for Na(mol%)=65.1(9), 545-775 °C, 50 s^{-1}, depleted uranium

$$\nu_{NaCl-MgCl_2}\left[\frac{mm^2}{s}\right] = 0.047(3) \times e^{\frac{22584(500)}{R*T[K]}}$$ for Na(mol%)=58.7(8), 454-800 °C, 50 s^{-1}

$$\nu_{NaCl-KCl}\left[\frac{mm^2}{s}\right] = 0.06(1) \times e^{\frac{20{,}000(2{,}000)}{R*T[K]}}$$ for Na(mol%)=50.1(8), 667-800 °C, 50 s^{-1}

Equation 18

4.6 Conclusion

High temperature experimental properties of three binary chloride mixtures with relevance to liquid fuel and heat transfer in molten chloride salt nuclear reactors (MCFRs) were measured: melting point, density, viscosity. Measurements results were discussed in the context of the variability of these types of measurements on these binaries in prior literature. All property measurements took place in a glove box on the same sample in the same environment with a cover gas of argon with H_2O < 0.1 ppm and O_2 < 5 ppm. The salt composition was characterized by acid microwave digestion followed by ICP-OES analysis with matrix-matched NIST standards. The melting points measured by DSC were $MP_{NaCl\text{-}UCl3}$ = 522.5(6) $[°C]$, $MP_{NaCl\text{-}MgCl2}$ = 440.7(1) $[°C]$, $MP_{NaCl\text{-}KCl}$ = 656(3) $[°C]$. The measurements used platinum crucibles for salt samples and Ag, Al, Zn, and Sn metal standards in alumina crucibles for temperature calibration. The densities measured by the hydrostatic method were $\rho_{NaCl-UCl_3}\left[\frac{g}{cm^3}\right] = 3.77(1) - 9.7(2) \times 10^{-4}T[°C]$ for Na(mol%)=65.1(9), 545-775 °C, depleted uranium, $\rho_{NaCl-MgCl_2}\left[\frac{g}{cm^3}\right] = 2.053(3) - 5.42(7) \times 10^{-4}T[°C]$ for Na(mol%)=58.7(8), 490-750 °C, and $\rho_{NaCl-KCl}\left[\frac{g}{cm^3}\right] = 1.967(7) - 5.5(1) \times 10^{-4}T[°C]$ for Na(mol%)=50.1(8), 680-775 °C. Volume on the nickel 200 alloy bobber was determined using the mass of the bobber and the material vendor-supplied density, and the volume uncertainty dominated the contributions to density measurement uncertainty. The viscosities measured experimentally using the rotational cup and bobber method were $\mu_{NaCl-UCl_3}[mpa \cdot s] = 0.085(9) \times e^{\frac{31{,}300(800)}{R*T[K]}}$ for Na(mol%)=65.1(9), 535-800 °C, 50 s^{-1}, depleted uranium, $\mu_{NaCl-MgCl_2}[mpa \cdot s] = 0.059(2) \times e^{\frac{24{,}800(200)}{R*T[K]}}$ for Na(mol%)=58.7(8), 454-800 °C, 50 s^{-1}, and $\mu_{NaCl-KCl}[mpa \cdot s] = 0.053(5) \times e^{\frac{24{,}700(700)}{R*T[°C]}}$ for Na(mol%)=50.1(8), 667-800 °C, 50 s^{-1}.

Prior literature for melting point of these melts had a variation of >20°C, and values reported here fall within the prior data ranges. Based on the data reviewed here, the variation cannot be solely attributed to crucible type, heating rate, measurement method and corresponding calibration, however, since a systematic study of factors affecting melting point has not been performed to date, it can be postulated that these factors can still have an effect. Melting point sensitivity to composition of the measured systems was investigated using literature provided phase diagrams and found to exceed the literature variability in the ± 2.5 mol percent compositional range around the eutectic for the $NaCl\text{-}MgCl_2$ and $NaCl\text{-}UCl_3$ binaries. Other factors such as oxygen content in cover gas and salt, composition, and moisture levels have not always been reported in the studies to date and should be evaluated in future studies for their impact on melting point.

Literature comparisons of experimental density measurements and ideal density calculations for $NaCl\text{-}UCl_3$ and UCl_3 melts were observed to have a wider variability than $NaCl\text{-}MgCl_2$ and NaCl-KCl ($NaCl\text{-}UCl_3$ Experimental:8%, $NaCl\text{-}MgCl_2$ Experimental:0.5%, NaCl-KCl Experimental:0.2%). It is postulated that the high variability in the uranium melts may be attributable to compositional uncertainty or redox uncertainty. The variability in the calculated $NaCl\text{-}UCl_3$ ideal density predicted by molar volume additivity with a ± 2.5 mol percent change in composition was 5%. The change in $NaCl\text{-}UCl_3\text{-}UCl_4$ ideal density and thermal expansivity with $U^{4+}/(U^{4+}+U^{3+})$ contents of 1, 5, and 10% were 1, 5, and 11% and 0.2, 3, and 5%, respectively. Data gaps exist in measuring the UCl_4 content (i.e. measuring the redox potential of the characterized salt) both in this work as well as in prior $NaCl\text{-}UCl_3$ property literature. Future studies should probe compositional sensitivity and redox sensitivity (i.e. UCl_3/UCl_4 ratio) on density and thermal

expansivity, to understand with what chemical variation these property changes become of engineering relevance.

The effect of the extent of complex formation on the viscosity of NaCl containing chloride salt binary melts across their compositional ranges was described. Among different studies, there is scatter in the activation energy and pre-exponential constant, which at the moment dominates over chemical compositional sensitivity. The compositional sensitivity will depend on mechanism that dominates viscosity, which in turn will vary with the composition of the melt. In the lower-concentration range of complex-forming cations, the coordination number has an influence of activation energy. At higher concentration, polymerization begins to dominate instead, as observed in the plots of activation energy versus composition. Data observed here is in agreement with prior structural observations of U^{3+} polymerization, and absence of large oligomeric species in the Mg^{2+} binary. In the KCl-NaCl binary, activation energy increases with NaCl content, indicating that NaCl might form stronger associates than KCl; the dominant mechanism that leads to this effect has not yet been described and merits further study.

5 FUTURE DIRECTIONS FOR ACTINIDE MOLTEN SALT STRUCTURE AND PROPERTIES CHARACTERIZATION

5.1 Sensitivity of Actinide and Non-Actinide Halide Salt Structure & Thermophysical Properties to Fission, Transmutation, and Neutron Activation Products

Based on the measurements and observations in Chapters 3 & 4, strong complex forming cations present in a molten salt system can increase the activation energy of viscosity of the system depending on their coordination number and degree of polymerization. Chapter 4 also demonstrated the importance of redox control on thermophysical property management in a fuel salt system, where multiple oxidation states of uranium may be present. To further explore the applications of these findings on a molten salt reactor, a study was completed experimentally simulating the burnup conditions inside of a NaCl-UCl_3 fueled molten salt reactor. Using predicted concentrations of uranium fuel and prominent fission and transmutation products after a burn-up time 180 MWd/kg-HM, this study examined how these changes in the fuel composition affect the redox potential and thermophysical property of the melt[8]. Three conditions were measured, the eutectic feed fuel salt (Eutectic Fuel), the fuel salt at the equilibrium sodium to uranium ratio after burn-up (Equilibrium Ratio), and the equilibrium ratio fuel salt with the addition of fission and transmutation products (Equilibrium Ratio & Fission Products). To ensure that property measurements were not affected by changes in the ratio of UCl_3 to UCl_4 as shown in Figure 28, a uranium metal rod was used to control the redox potential of the salt as shown in Equation 19. As uranium metal exposed to oxygen and moisture can result in the formation of uranium oxide, to remove any oxide layer present on the rod, the rods were submerged in molten NaCl prior to usage. Figure 32 illustrates the mass of uranium reacted as a function of time at each condition. Based on Equation 19 and an original sample mass 196.660 g, the Equilibrium Ratio condition contained ~4 mol% of UCl_4 before reduction. Similarly, assuming all uranium metal rod oxidation and mass loss was due to the formation of UCl_4, the Equilibrium Ratio & Fission Products sample contained ~45% UCl_4 before reduction. As shown by the calculations Table 11 and the mass loss in Figure 32, based on the 13.3370(1) g of U metal consumed during the Equilibrium Ratio and Fission Product reduction step, the molybdenum and ruthenium chlorides, which one would expect to be metals after redox, would account for ~13 g of this reaction.

$$3UCl_4 + U \rightarrow 4UCl_3$$

Equation 19

Table 11. Sample information table of fission product additions for Equilibrium Ratio & Fission Product sample preparation.

Sample	Supplier	Mass Added (g)	Moles Added (mol of cation)	U Metal potentially reacted by fission product (g)
$CeCl_3$	Sigma Aldrich	14.6161(1)	0.0593	14
$NdCl_3$	Sigma Aldrich	4.8250(1)	0.01925	5
CsCl	Sigma Aldrich	3.2749(1)	0.1945	0
$ZrCl_4$	Sigma Aldrich	6.9054(1)	0.02963	9
$RuCl_3$	Sigma Aldrich	3.0728(1)	0.1481	4
$MoCl_5$	LANL (Thermo Fisher Scientific)	6.0767(1)	0.2224	9

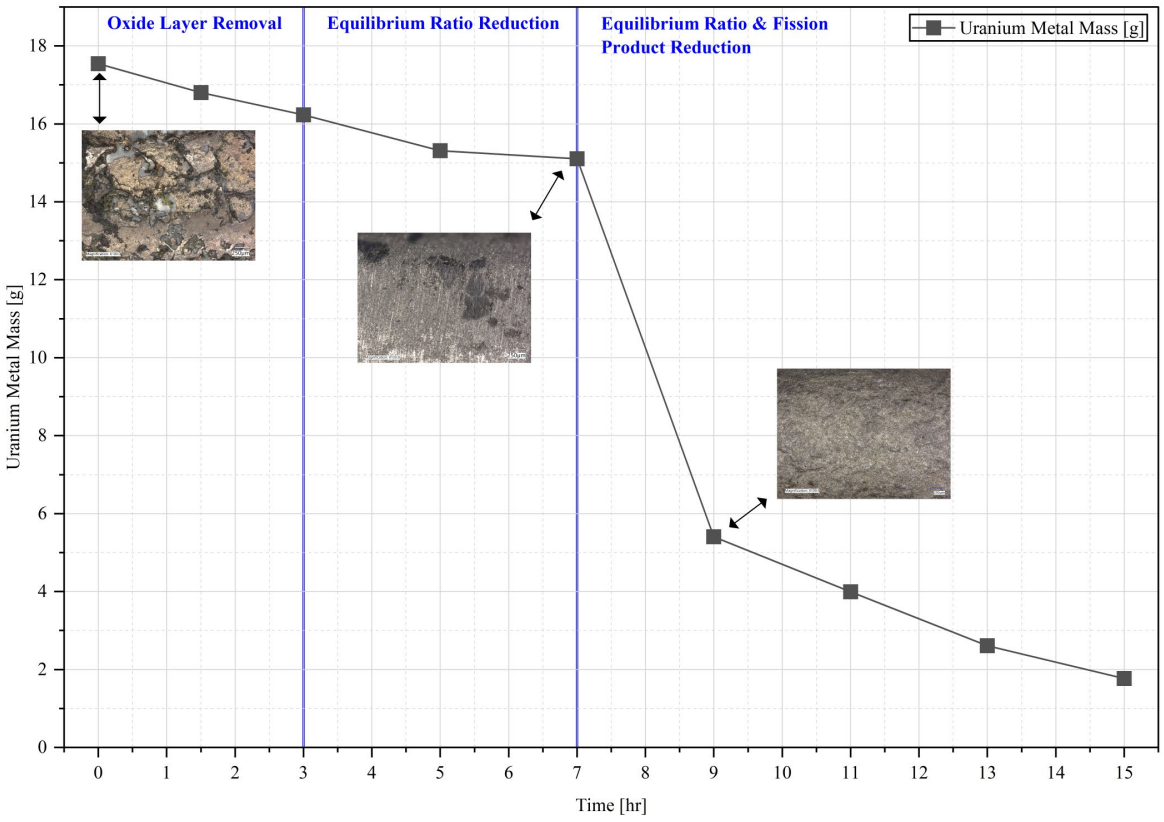

Figure 32. Mass of the uranium rod used for redox control in this study mass as a function of time submerged in the $NaCl$-UCl_3 fuel salt. The three conditions measured are indicated by the vertical blue lines.

Density was measured using the same hydrostatic method as Chapters 3 & 4, with a Nickel 200 alloy bobber and wire, suspended from a balance. Error analysis was completed with linear fit with x and

y error of the 60 recorded data points using OriginPro[104]. Bobber volume calibration was completed using the vendor reported density for the Nickel 200 alloy material and the experimentally measured mass of the bobber. Results of the density sensitivity measurements are shown in Figure 33.

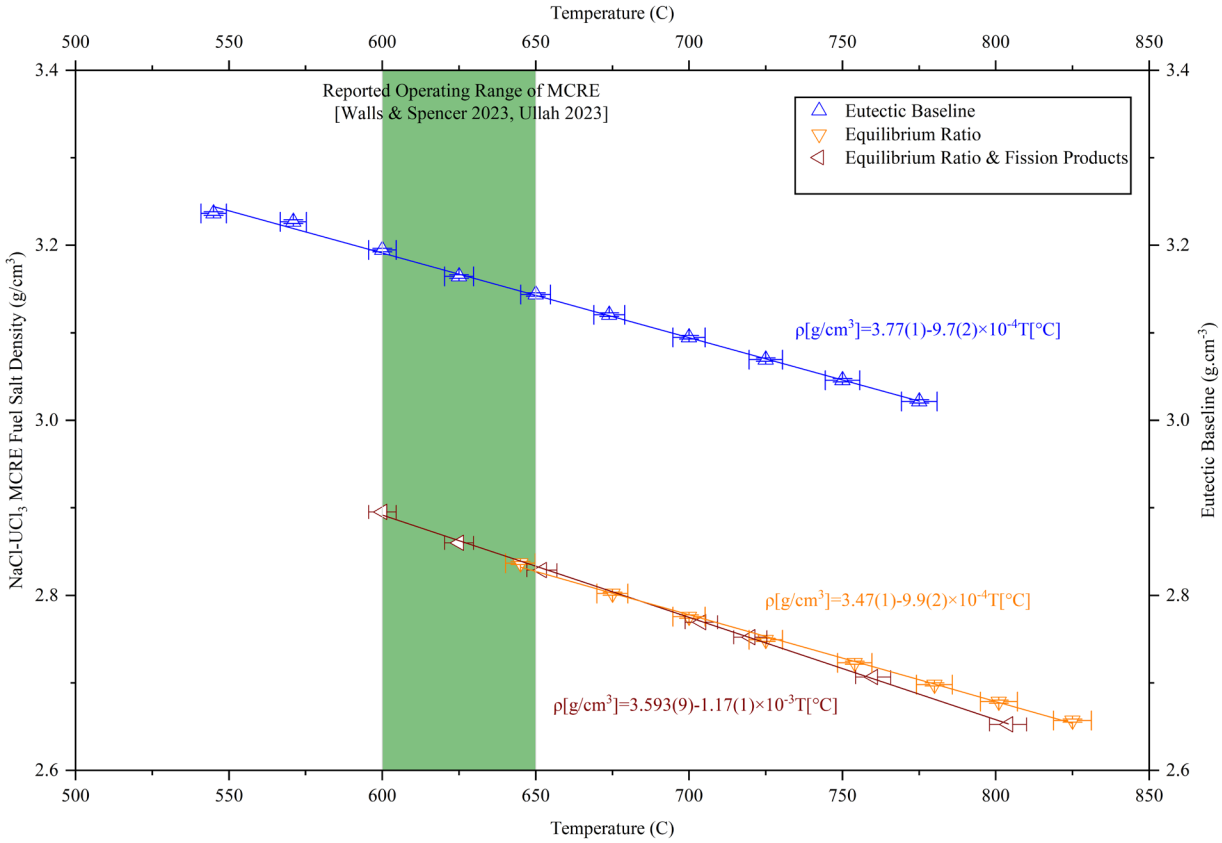

Figure 33. Sensitivity of density to each measured condition. MCRE operating ranges were gathered from Ref.[15], [173], [174]

Viscosity was measured using an Inconel 625 measuring cup and cylinder on an Anton Paar modular compact rheometer (MCR702e). Experimentation took place inside of an argon glovebox, and argon cover gas was flown through the oven over the sample at a flow rate of 20 ml/min. Absolute viscosity readings in mPa*s were collected using the rotational method at a shear rate of $50s^{-1}$. As the temperature was ramped at a constant linear rate from 600°C to 825°C, readings were collected at a constant rate of 1 point per 3.25 minutes. Uncertainty was propagated using the fitting error of the viscosity Arrhenius equation[104], [134]. Instrument calibration took place using a Cannon Instrument Company S600 certified viscosity reference standard at 80°C. Results of the viscosity sensitivity measurements are shown in Figure 34.

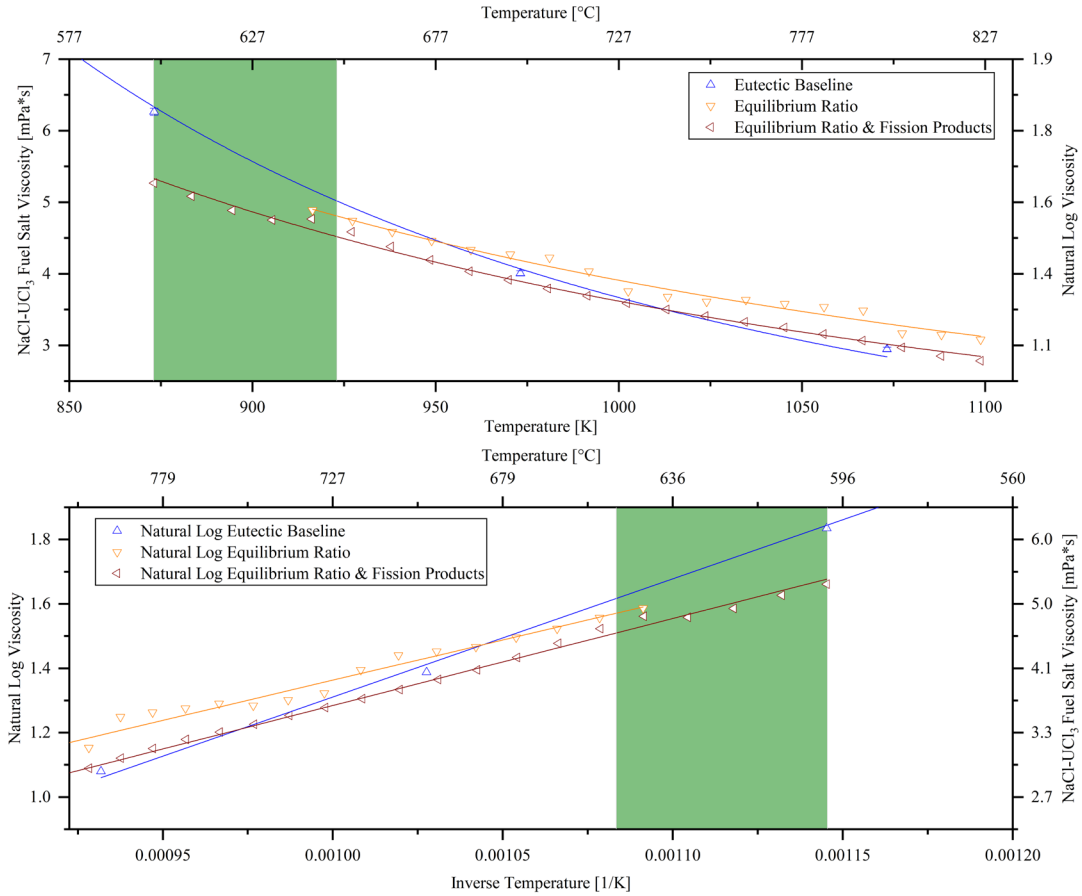

Figure 34. . Sensitivity of viscosity to each measured condition. MCRE operating ranges were gathered from Ref.[15], [173], [174]

Using the experimental density and viscosity trends with propagated error measured for the three operating conditions, the variation of the density, thermal expansivity, viscosity, activation energy of viscosity, and Arrhenius viscosity pre-exponential constant for the NaCl-UCl_3 eutectic feed fuel salt to changes in composition was calculated (the equilibrium sodium to uranium ratio, the equilibrium ratio with the addition of fission products). The sensitivity to each of these parameters was calculated at 600 °C and 650 °C, the high and low end of the planned MCRE fuel salt operating range[15], [173], [174].

Table 12. Sensitivity analysis of density, thermal expansivity, viscosity, activation energy of viscosity, and pre-exponential constant of the NaCl-UCl_3 feed fuel salt to changes in composition to the equilibrium sodium to uranium ratio as well as the equilibrium ratio with the addition of fission products. Percent difference was calculated at 600 °C and 650 °C, the high and low end of the planned MCRE fuel salt operating range[15], [173], [174]. Eutectic data was collected from 535-800 °C for viscosity and from 545-775 °C for density.

Percent Difference of Eutectic Fuel Salt Compared to…	**Density**		**Viscosity**		
Condition Name	Density (%)	Thermal Expansivity (%)	Viscosity (%)	Activation Energy of Viscosity (%)	Pre-Exponential Constant (%)
Equilibrium at 600 °C	-9.7(8)	2(3)	*-1(2)*	*-3.4(3)*	*2.8(5)*
Equilibrium at 650 °C	-9.9(9)	2(3)	-.04(0.2)	-3.4(3)	2.8(5)
Equilibrium & Fission Products at 600 °C	-9.4(6)	2.1(3)	-2(1)	-2.9(2)	1.9(4)
Equilibrium & Fission Products at 650 °C	-9.9(7)	2.1(3)	-1(2)	-2.9(2)	1.9(4)

As shown by the experimental data in Figure 33 and Figure 34, and the sensitivity analysis in

Table 12, the progression of the MCRE initial eutectic NaCl-UCl_3 fuel salt feed to its equilibrium state can potentially change the melt density ~10% and viscosity ~3%, based on the simulations results from Ref.[8]. To understand the mechanisms of how uranium burnup and fission product propagation influence these properties, the methods used in Chapters 3 & 4 can be applied. Changes in the activation energy of viscosity due to changing UCl_3 concentrations in an NaCl-UCl_3 were shown to be described by a linear fit in Figure 31. Thus, for the shifting sodium to uranium ratio in the MCRE fuel salt, the activation energy of viscosity can then be predicted.

As shown in Figure 32, based on the mass loss of the uranium rod used for redox control, the addition of fission products can shift the redox potential of the fuel salt[8], [9], [10], [11], [171]. For the fission products that remain soluble in this salt after redox control, the speciation mechanisms of every constituent have not all been fully characterized. However, as demonstrated in Chapter 3, for a non-binary actinide melt containing multiple cations (NaF-BeF_2-UF_4-ZrF_4 used in Chapter 3), at low coordinating cation concentration, the coordination number of each species can be used to predict activation energy of viscosity behavior. To fully verify this technique in NaCl-UCl_3 fuel salt systems containing fission products, it is necessary to know the solubility in the fuel at the design specified redox potential, the coordination number in the liquid state, and the degree of polymerization for each fission and transmutation product species.

In addition to the chloride fuel salt system, Hydrogen isotopes such as tritium are present in actinide halide fuel salt systems as a fission product, as well as in FLiBe salt-cooled nuclear reactor systems due to neutron capture of lithium-6, which subsequently decays into an alpha particle and tritium[8], [21], [53], [175], [176]. To understand the structural effects and speciation behavior of these isotopes on molten salt, low temperature neutron diffraction analysis of a well characterized salt, FLiBe, with hydrogen added as LiH was completed in December 2021 on the HIPPO instrument at the LANSCE facility at LANL[177]. This method and reaction shown in Equation 20 [177] has been demonstrated in prior electrochemical studies[177].

$$2LiH + BeF_2 = 2LiF + Be(m) + H_2(g)$$

Equation 20 [177]

Using the FLiBe + 1 mol% LiH sample characterized in Chapter 2, after a 6-hour heating and cooling cycle, evidence of LiH and BeH_2 was observed in the solid sample using neutron scattering. As shown in Figure 35, peak fitting was conducted using the MAUD software with cif files from the ICSD for 2Lif-BeF_2, LiH, and BeH_2[41], [178], [179], [180], [181]. The inset in Figure 35 at ~3.9 angstroms indicates the location of a experimental peak corresponding to BeH_2. The shoulder present in the peak at ~2.2 angstroms shows evidence of the presence of LiH. As previously reported in Chapter 2 and demonstrated in Figure 7, solid FLiBe contains strong preferred orientation and large grains. The Rietveld analysis completed using the MAUD software assumes that the sample is composed of a powder with random orientations. If the FLiBe + 1 mol% LiH sample was a random powder or a single crystal without preferred orientation, it would be expected that the intensities of the vertical line patterns on the 2D multiplot in Figure 36 would be constant. This may also elucidate why the measured peaks shown in Figure 35 and the fits from Ref.[41], [180], [181] differ slightly in position and intensity[55], [56], [58]. In future studies, to further characterize the speciation behavior of hydrogen isotopes in molten salt, either textural refinement of a solid sample should be completed during measurement or a resolidified powder FLiBe + 1 mol% sample should be analyzed. However, this study demonstrated how the solvation of hydrogen isotopes in molten salt is possible, and this knowledge of solvation behavior can be directly applied to tritium management in molten salt fueled and cooled reactors.

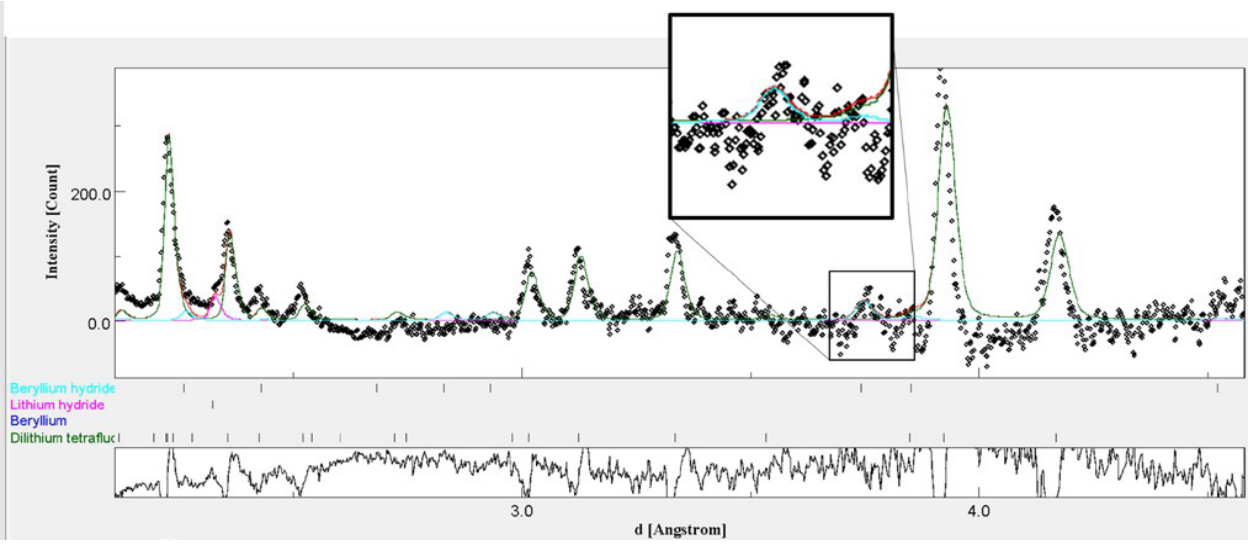

Figure 35. Solid FLiBe + 1 mol% LiH sample neutron scattering spectra with preliminary peak fitting to 2LiF-BeF_2, BeH_2, and LiH collected on the HIPPO instrument at the LANSCE Facility[56]. The magnified inset shows possible evidence of the presence of solid BeH_2. Peak fitting and analysis was conducted with the Materials Analysis Using Diffraction (MAUD) software[179].

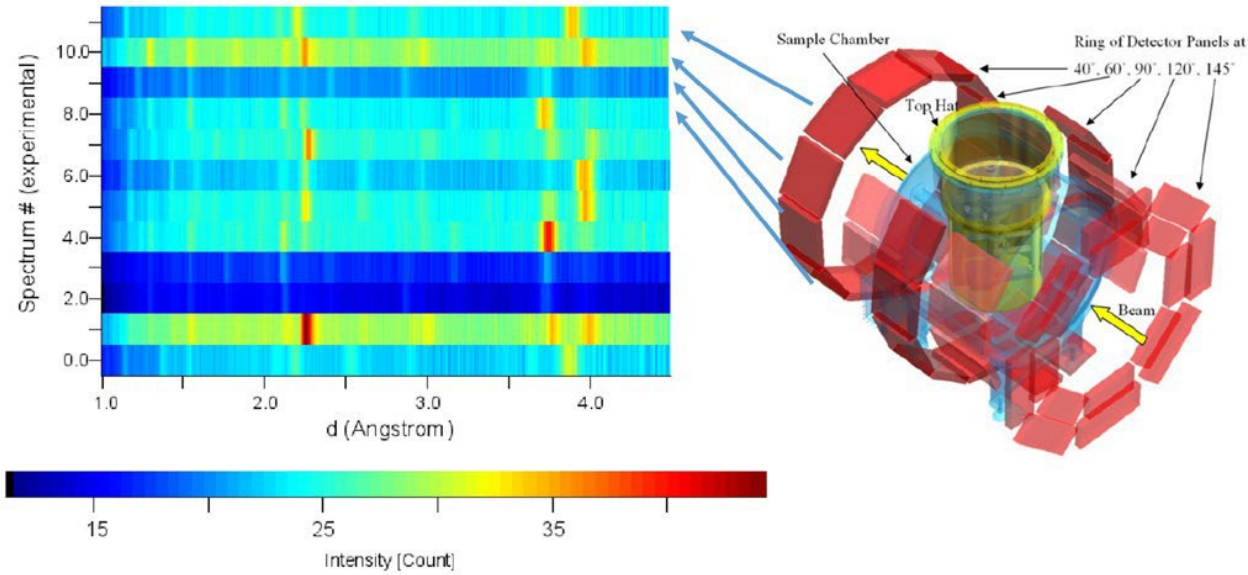

Figure 36. (Left) 2D Multiplot of detector banks with measured intensities from FLiBe + LiH neutron scattering experiment. (Right) A schematic of the Hippo Instrument. Arrows are used to indicate where the 2D multiplot detector banks are located on the instrument.

5.2 Probing Structural Mechanisms behind Thermophysical Properties in Molten Salts

As the previous chapters demonstrated, liquid structure can be correlated to changes in molten salt thermophysical properties. To further examine the mechanisms connecting internal structure to measurable properties, oscillatory rheology is a potential technique. This method is mentioned in Chapter 3, where oscillatory rheology is proposed as a method to probe internal molten structure. For the oscillatory method, the deflection path of the upper measuring apparatus of the viscometer is used to apply a controlled strain on the sample resulting in a measured shear stress[182]. The amplitude of the sinusoidal curve of strain and

stress response are used to calculate the complex shear modulus, |G*[182]|. The dynamic viscosity of the fluid divided by this complex shear modulus then produces the structural relaxation time $t_{relaxation}$. G can be broken down into two parts; a modulus describing the viscous properties of the melt, denoted as the Loss Modulus G^{I}, and a modulus describing the elastic portion denoted as the storage modulus, G^{II}. These relationships are illustrated in Equation 21.

$$G = \frac{\tau_A}{\gamma_A},$$

$$\mu = G \times t_{relaxation},$$

$$\tan(\delta) = \frac{G^{II}{}_{loss}}{G^{I}{}_{storage}}$$

Equation 21 [182]

The dynamic viscosity output from rotational rheology is dependent on temperature. Temperature is measured using a thermocouple located undeath the lower Inconel measuring accessory. To describe the viscous behavior of the salt over the full range of measured temperatures, it is possible to fit the measured viscosity to an exponential equation to extract the activation energy required for viscous flow.

$$\mu = A \times e^{\frac{E_a}{RT}}$$

Equation 22

The Arrhenius equation shown in Equation 22, contains the additional parameters A, a dimensionless pre exponential constant, R, the universal gas constant, T, the absolute temperature, and E_a, the activation energy of viscosity[80]. The calculated activation energy describes the energy required for the ions and species driving the viscosity of the melt to overcome the potential energy barrier for flow[183].

$$\mu = A \times e^{\frac{E_a}{R(T-T_g)}}$$

Equation 23

The Vogel-Fulcher-Tammann equation shown in Equation 23 also determines the activation energy of viscosity, but takes into account the different behavior above and below the glass transition temperature T_g[183]. This equation can potentially be used in future molten salt experimental studies as beryllium fluoride has been measured to have a glass transition temperature with values of 325°C and 390°C being reported[184], [185]. With this glass transition behavior correction, the activation energy of viscosity of BeF_2 based on the data measured by Ref.[107] changes from 245,000(4000) J/mol (Arrhenius fit) to 13,800(300) J/mol (Ref. [184]), and 23,900(500) J/mol (Ref. [185]). For high BeF_2 concentration melts, the characterization of any potential glass transition temperature should be explored to ensure accurate viscosity comparisons are completed.

By incrementally increasing the amplitude of the strain applied on the salt using the oscillatory method, its behavior in the non-destructive deformation range can be characterized[182]. The region before destructive deformation occurs is called the linear viscoelastic region (LVE). Figure 37 shows preliminary studies of the behavior of the storage modulus [G^{II}], loss modulus [G^{II}], complex shear modulus [|G*|], and loss factor [tan(δ)] of this region in molten FLiBe at 469, 500, 600, and 700 °C. Repeatability was not observed below 0.01% shear strain, so this value was used as the lower detection limit of the instrument.

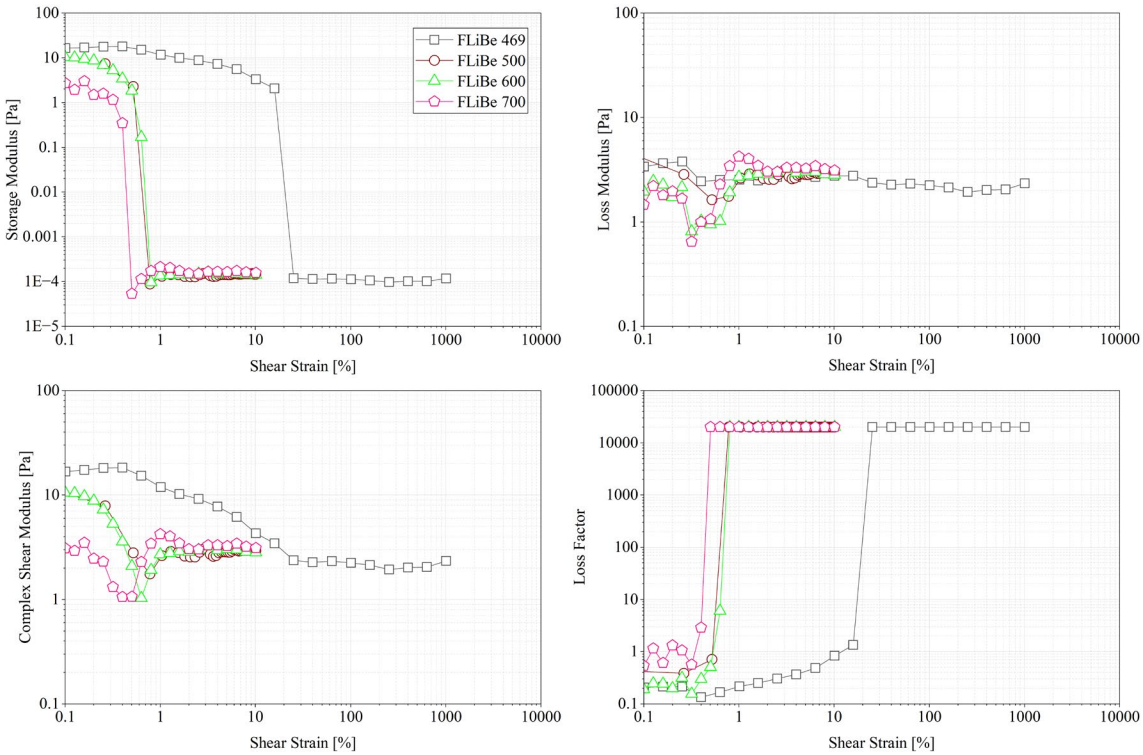

Figure 37. The storage modulus [G^{II}] (top left), loss modulus [G^{II}] (top right), complex shear modulus [|G*|] (bottom left), and loss factor [tan(δ)] (bottom right) of FLiBe.

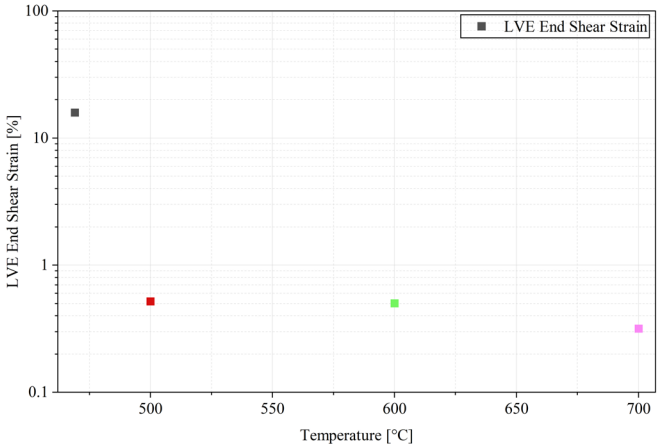

Figure 38. Comparison of ending points of the FLiBe Linear Viscoelastic Region (LVE) measured in Figure 37 versus temperature.

The LVE of the elastic contribution to the complex shear modulus of FLiBe, shown in the top left of Figure 37, decreases in length with increasing temperature. For 469 °C, 10 °C above the melting point of FLiBe, the elastic structure begins to break down at a shear strain of ~0.9%, with the structure fully disassociated at ~11%. As the temperature of the melt is increased to 500, 600, and 700 °C, the LVE is reduced and the structure is fully broken before 1% shear strain. For all temperatures, the loss modulus for FLiBe follows a linear trend with an average value of 3(2) Pa.

Based on the studies in Chapters 3 & 4 and the preliminary oscillatory rheology measurements, one would expect melts with higher complex forming cation content to contain a longer LVE, and a higher storage modulus [G^{II}] when compared to more disassociated melts[186], [187]. This method has been demonstrated in a study measuring the viscoelasticity of water in waxy crude oil emulsion gels [186]. To fully explore this hypothesis as well, amplitude sweeps on melts of varying complex forming cation contents should be completed at a set temperature for comparison. The uncalibrated shear modulus measured values and temperature dependent viscosity data are available in supplemental information but are not recommended for relaxation time calculation. To accurately extract the relaxation time of FLiBe at a specific temperature to compare to prior modeling literature, a viscoelastic standard such as PDMS (Polydimethylsiloxane) should be measured to validate complex shear modulus results[26], [79], [188]. Nevertheless, these preliminary oscillatory rheology experiments of molten FLiBe provide a proof of concept for a method capable of probing the structure of a molten salt, which provides new knowledge on connecting liquids structure to thermophysical properties.

6 CONCLUSION & APPLICATIONS FOR NUCLEAR CHEMICAL ENGINEERING

This work explores the connections between the internal structure and thermophysical properties of solid and liquid salts. This knowledge is of relevance to the fuel qualification, operation, and safety of liquid fueled molten salt nuclear reactors. In this dissertation, the influence of complex forming species on these parameters is examined by comparing the effects oligomeric species with varying degrees of polymerization. As molten actinide halide salts with cation forming constituents such as uranium, plutonium, and thorium have been reported to form large oligomeric species, to predict how fuel salt properties may alter at different compositions and temperatures, the determination of the ways in which the mechanisms of experimental properties are guided by oligomer formation is vital.

Through the exploration of the solid structure of a well characterized salt in Chapter 2, the bonding behavior, solid coordination number, temperature dependent solid density, and thermal expansion coefficient of FLiBe is reported. From these measurements it was observed that the FLiBe unit cell expands anisotropically, with the expansion rate of the *c* parameter calculated to be 1.54 times the rate of the *a* parameter. Additionally, the structural changes present during phase change from liquid to solid are explored for the first time, and the FLiBe was measured to have a ~3% volume shrinkage upon freezing, similar to the MSRE fuel salt. Characterization of the structure and solid properties of the FLiBe unit cell such as, solid coordination number, temperature dependent solid density, solid thermal expansion coefficient, and the volume change upon melting can be applied directly to MSR operations below the melting point of FLiBe at 459 °C, such as reactor startup, shutdown, and freezing incidents.

In Chapter 3, this work applied these structural properties to two molten sodium-fluoroberyllate salt systems, with one containing uranium. By comparing and contrasting the temperature dependent density and viscosity of these two systems, as well as titrations from prior literature, it was determined that when normalizing to the same coordination number, at concentrations of complex forming cations below 60%, the activation energy of the viscosity for the systems followed the same trend. However, as the concentration of complex forming cations increases, the differences in the oligomer forming properties of these cations become more pronounced. As measured by neutron diffraction structural studies, the extent of chain formation (also designated as the degree of polymerization) between beryllium and uranium differs, with beryllium fluoride melts forming complex species containing a high number of coordinating cations than uranium fluoride melts. For molten salt fuel systems where the melt composition may change due to burnup, such as in a $NaF\text{-}BeF_2\text{-}UF_4\text{-}ZrF_4$ fuel salt, this new knowledge of the relationship between the activation energy of viscosity, coordination number, and complexation ability can help better predict the viscosity at the various compositions that will occur.

In Chapter 4, this study of coordinating cation behavior in fuel and heat transfer salts was continued in chloride systems. By propagating uncertainties in the measurement of the macroscopic properties of melting point, density, and viscosity, analysis was completed on the polymerization behavior of three salts with varying extents of complex formation. Using neutron diffraction pair distribution function literature and activation energy of viscosity titrations from prior data, by calculating the slope of activation energy of viscosity vs complex forming cation concentrations, this work showed that a higher degree of polymerization of the coordinating cation corresponded to an increase in the slope of the activation energy vs concentration. Additionally, this chapter also completed a sensitivity analysis of redox and composition on the $NaCl\text{-}UCl_3$ fuel system and demonstrated the necessity of future redox control studies by calculating that the percent change in the $NaCl\text{-}UCl_3\text{-}UCl_4$ ideal density and thermal expansivity with $U^{4+}/(U^{4+}+U^{3+})$ contents of 1, 5, and 10% were 1, 5, and 11% and 0.2, 3, and 5%, respectively. Similarly in Chapter 5, preliminary results of a sensitivity analysis comparing the eutectic feed $NaCl\text{-}UCl_3$ fuel salt to an $NaCl\text{-}UCl_3$ at its equilibrium ratio of Na:U and to the equilibrium Na:U melt after addition of simulation predicted fission products. At 650°C The percent change in the density, thermal expansivity, and viscosity of the eutectic fuel salt when compared to the Equilibrium Ratio and Equilibrium Ratio & Fission Products melts were -9.9(9), 2(3), -0.04(0.2)% and -9.9(7), 2.1(3), and -1(2)% respectively.

In conclusion, to ensure that a molten salt reactor nuclear fuel salt fulfills the fundamental safety functions necessary for reactor operation and fuel qualification, characterization and error propagation of the thermophysical properties of the fuel salt including but not limited to density, thermal expansivity, viscosity, melting point is essential. In this work, the thermophysical properties of fuel salts are measured and the relationship among properties, internal structure, and property uncertainty present in a halide salt system are explored. The understanding developed in this work impacts molten salt nuclear reactor design and safety. It is determined that FLiBe freezes with strong preferred orientation and expands ~3% upon melting, providing data for molten salt vessel and piping design. This dissertation quantifies the extent to which the absence of redox control in a reactor can affect the fuel salt density by changing the oxidation state of the uranium present, which emphasizes the importance of redox control in a molten salt reactor system. To predict if viscosity of a fuel salt will shift outside of planned safety tolerance ranges in molten salt reactor due to burnup, this dissertation also connects the activation energy of viscosity of a salt melt to the coordination number, concentration, and complex forming ability of its cation constituents. Demonstrated experimentally through binary and quaternary melts, this theory shows that while at concentrations below ~60 mol% the diffusion of ionic species formed from strong complex forming cations result in similar viscous behavior when corrected for coordination number, at higher concentrations, the polymerization behavior of oligomer forming species begins to dominate. This method can be applied in reactor environments to ensure that a fuel salt after burnup containing fission products will still meet design criteria. Additionally, though future development is needed, this work also demonstrates the potential of what is novel technique in molten salts, of using oscillatory rheology to measure the breakage of structure present in a molten salt. This method begins to provide an understanding of the molecular structure of molten salts, assisting in the development and validation data set of models that predict thermo-physical properties based on ab-initio or other forms of molecular dynamics simulations. This dissertation provides experimental data and fundamental science knowledge that will enhance the fuel qualification and reactor operation of molten salt reactors.

7 DATA AVAILABILITY

The following files are archived as follows:

- Raw mass difference density values of NaCl-UCl_3 Equilibrium Ratio and Equilibrium Ratio & Fission Product Melts (Chapter 5 – Chapter 5 Chloride Fuel Sensitivity Density, CSV)
- Instrument collected viscosity data of NaCl-UCl_3 Equilibrium Ratio and Equilibrium Ratio & Fission Product Melts Chapter 5 Chloride Fuel Sensitivity Viscosity, CSV)
- Instrument collected viscoelasticity data of FLiBe (Chapter 5 – Chapter 5 Viscoelasticity Data, CSV)
- Raw mass difference density values of NaCl-KCl, NaCl-UCl_3, and NaCl-$MgCl_2$ (Chapter 4 – Chapter 4 Density Data, CSV)
- Instrument collected viscosity data of NaCl-KCl, NaCl-UCl_3, and NaCl-$MgCl_2$ (Chapter 4 – Chapter 4 Viscosity Data, CSV)
- Instrument collected DSC data of NaCl-KCl, NaCl-UCl_3, and NaCl-$MgCl_2$ (Chapter 4 – Chapter 4 DSC Data, CSV)
- Instrument collected elemental analysis data of NaCl-KCl, NaCl-UCl_3, and NaCl-$MgCl_2$ (Chapter 4 – Chapter 4 Elemental Analysis Data, CSV)
- DSC Metal standard certificates (Chapter 4 - Chapter 4 DSC PJLA-certified Metal Standards, PDF)
- Viscometer Calibration Certificate and Verification Report (Chapter 4 - Chapter 4 Viscometer Calibration Report, PDF)
- Raw mass difference density values of LiF-BeF_2, NaF-BeF_2 and NaF-BeF_2-UF_4. Partial Differential Equation for Thermal expansivity as a function of temperature and composition based on the molar volume additivity ideal density model (Chapter 3 – Chapter 3 Density Data, CSV)
- Instrument collected viscosity data of LiF-BeF_2, NaF-BeF_2, and NaF-BeF_2-UF_4 (Chapter 3 – Chapter 3 Viscosity Data, CSV)
- Raw neutron and X-ray diffraction data of LiF-BeF_2 (Chapter 2 - FLiBe NOMAD Raw GSAS, FLiBe PDF Raw GSAS, Rietveld Fit Histograms)

These files are stored in the SALT group Berkeley Box account under the following addresses…

- Berkeley Box, SALT_GROUP_FOLDERS, 99-Personal Folders, Nathanael, Dissertation, Dissertation Supplemental Data
- Berkeley Box, SALT_GROUP_FOLDERS, Project Folders, UCBS-35/UCBS-50
- Berkeley Box, SALT_GROUP_FOLDERS, J-Publications, J-90/J-69/J-60/J-94/J-54

8 ACKNOWLEDGEMENTS

This work contains components and data from the following published papers.

- "Complex Structure of Molten FLiBe (2LiF-BeF2) Examined by Experimental Neutron Scattering, X-Ray Scattering, and Deep-Neural-Network Based Molecular Dynamics." S. Fayfar, R. Chahal, H. Williams, D. Nathanael Gardner, et al PRX Energy 2024. 10.1103/PRXEnergy.3.013001
- "Solid structure of Li2BeF4 (FLiBe) from room temperature to melting studied by neutron and X-ray diffraction." D. Nathanael Gardner, et al. Journal of Applied Crystallography 2025. 10.1107/S1600576725000548
- "The Effect of Complex Forming Cations on the Thermophysical Properties of Beryllium and Uranium Fluoride Salts for Nuclear Reactor Applications." D. Nathanael Gardner, et al ACS Physical Chemistry Au 2025 10.1021/acsphyschemau.5c00043
- "Probing Speciation of Light Elements in Molten Salts by Electrochemistry, High Temperature Liquid NMR, and Neutron Diffraction." H. Williams, D. N. Gardner, et al. 2022 ANS Annual Meeting. doi.org/10.13182/T126-38488
- "Sources of Error in the Measurement of Thermophysical Properties of Molten Salts", D. Nathanael Gardner et al, ANS Winter Conference Paper 2023. doi.org/10.13182/T129-42452
- "Safety Analysis on Fission Induced Thermophysical Property Alterations of MCFR Fuel Salt." D. Nathanael Gardner et al, ANS Winter Conference Paper 2025. doi.org/10.13182/T133-48896

This work also contains components and data from the following unpublished works currently in the submission process.

- "Density, Calorimetry and Viscosity of Fuel and Heat Transfer Salts for Molten Chloride Fast Reactor (MCFR) Applications." **D. Nathanael Gardner**, *et al* ACS Applied Energy Materials (In Review)
- "Sensitivity of Eutectic Chloride Fuel Salt Thermophysical Properties to Molten Chloride Fast Reactor (MCFR) Operation" **D. Nathanael Gardner**, *et al* ACS Applied Energy Materials (In Preparation)
- "Viscoelastic Properties of BeF2 containing Molten Salts" **D. Nathanael Gardner**, Raluca O. Scarlat, Journal of Molecular Liquids (In Preparation)
- "Evidence of screening, polarization, and excess bridging in the network connectivity formation of LiF-BeF2 molten salts: from neutron and X-ray scattering, Hayley Williams, **D. Nathanael Gardner**, *et al* (In Preparation)

All co-authors on these manuscripts were contacted for permission prior to the submission of this work.

The CAD model in Figure 2 was created by Sebastian Barnes. A portion of this research used the 28-ID-1 beam line of the National Synchrotron Light Source II; a U.S. Department of Energy (DOE) Office of Science User Facility operated for the DOE Office of Science by Brookhaven National Laboratory under Contract No. DE-SC0012704. A portion of this research used resources at the Spallation Neutron Source, a DOE Office of Science User Facility operated by the Oak Ridge National Laboratory. This work also utilized the Los Alamos Neutron Science Center (LANSCE) at Los Alamos National Laboratory (LANL). Los Alamos National Laboratory is operated by Triad National Security, LLC, for the National Nuclear Security Administration of the U.S. Department of Energy under contract number 89233218NCA000001. Research on this work was in part supported by the Department of Energy's Nuclear Energy University Program (DOE-NEUP) project 21-24563. Research on this work is in part supported by the Department of

Energy's Nuclear Energy University Program (DOE-NEUP) project 22-28329, and by ThorCon Power. Students on this work are also supported by the Department of Energy's University Nuclear Leadership Program (DOE-UNLP) and the National Science Foundation Graduate Research Fellowship Program (NSF-GRFP) fellowships.

Salts utilized in the research were provided by the Nuclear Materials and Fuel Cycle Center at Salts utilized in the research were provided by the Nuclear Materials and Fuel Cycle Center at Virginia Tech (UZrFNaBe), the University of Wisconsin Madison and ThorCon Power (FNaBe), prepared by an industry collaborator from ORNL salts (FLiBe), TerraPower (NaCl-UCl_3 and NaCl-$MgCl_2$) , Los Alamos National Laboratory (NaCl), and Oak Ridge National Laboratory (NaCl-KCl). Adam Lau from the University of California Berkeley took the photograph of NaF-BeF_2-UF_4 on the viscometer lower parallel plate.

9 REFERENCES

[1] G. Locatelli, M. Mancini, and N. Todeschini, “Generation IV nuclear reactors: Current status and future prospects,” *Energy Policy*, vol. 61, pp. 1503–1520, Oct. 2013, doi: 10.1016/j.enpol.2013.06.101.

[2] B. Zohuri, “6 - Generation IV nuclear reactors,” in *Nuclear Reactor Technology Development and Utilization*, S. U.-D. Khan and A. Nakhabov, Eds., in Woodhead Publishing Series in Energy. , Woodhead Publishing, 2020, pp. 213–246. doi: 10.1016/B978-0-12-818483-7.00006-8.

[3] T. Abram and S. Ion, “Generation-IV nuclear power: A review of the state of the science,” *Energy Policy*, vol. 36, no. 12, pp. 4323–4330, 2008.

[4] “Generation IV Goals, Technologies and GIF R&D Roadmap | GIF Portal.” Accessed: Apr. 01, 2026. [Online]. Available: https://www.gen-4.org/generation-iv-criteria-and-technologies

[5] J. Serp *et al.*, “The molten salt reactor (MSR) in generation IV: Overview and perspectives,” *Prog. Nucl. Energy*, vol. 77, pp. 308–319, Nov. 2014, doi: 10.1016/j.pnucene.2014.02.014.

[6] E. Blandford *et al.*, “Kairos power thermal hydraulics research and development,” *Nucl. Eng. Des.*, vol. 364, p. 110636, Aug. 2020, doi: 10.1016/j.nucengdes.2020.110636.

[7] “TerraPower fast chloride reactor,” in *Molten Salt Reactors and Thorium Energy*, Woodhead Publishing, 2024, pp. 953–972. doi: 10.1016/B978-0-323-99355-5.00020-3.

[8] S. Paul, S. Attarian, M. Fratoni, D. Morgan, and I. Szlufarska, “Influence of transmutation products on the thermophysical properties of eutectic NaCl-UCl3 fuel salt in a fast-spectrum molten salt reactor,” *J. Nucl. Mater.*, vol. 605, p. 155572, Feb. 2025, doi: 10.1016/j.jnucmat.2024.155572.

[9] J. Zhang *et al.*, “Redox potential control in molten salt systems for corrosion mitigation,” *Corros. Sci.*, vol. 144, pp. 44–53, Nov. 2018, doi: 10.1016/j.corsci.2018.08.035.

[10] M. Rose and D. Ezell, “Molten Salt Reactor Fuel Cycle Chemistry Workshop Report,” ANL/CFCT--23/50, 2311167, 187645, Sep. 2023. doi: 10.2172/2311167.

[11] A. M. Wheeler, V. Singh, L. F. Miller, and O. Chvála, “Initial calculations for source term of Molten Salt Reactors,” *Prog. Nucl. Energy*, vol. 132, p. 103616, Feb. 2021, doi: 10.1016/j.pnucene.2020.103616.

[12] E. S. Bettis, R. W. Schroeder, G. A. Cristy, H. W. Savage, R. G. Affel, and L. F. Hemphill, “THE AIRCRAFT REACTOR EXPERIMENT. DESIGN AND CONSTRUCTION,” *Nucl. Sci Eng*, vol. Vol: 2, Oct. 1957, Accessed: Jan. 07, 2026. [Online]. Available: https://www.osti.gov/biblio/4322653

[13] M. W. Rosenthal, P. R. Kasten, and R. B. Briggs, “Molten-Salt Reactors—History, Status, and Potential,” *Nucl. Appl. Technol.*, vol. 8, no. 2, pp. 107–117, Feb. 1970, doi: 10.13182/NT70-A28619.

[14] P. N. Haubenreich and J. R. Engel, “Experience with the Molten-Salt Reactor Experiment,” *Nucl. Appl. Technol.*, vol. 8, no. 2, pp. 118–136, Feb. 1970, doi: 10.13182/NT8-2-118.

[15] Noor Ullah *et al.*, “MCRE Design Description in Support of External Model Development,” TerraPower, MCRE-ENG-PRSNT-0029, Dec. 2022. Accessed: Oct. 15, 2025. [Online]. Available: https://www.researchgate.net/publication/369261248_MCRE_Design_Description_in_Support_of_External_Model_Development

[16] R. Belles, G. F. Flanagan, D. E. Holcomb, and W. P. Poore III, “A safety and licensing

roadmap to identify the research and development gaps of commercial molten salt reactors," Oak Ridge National Laboratory (ORNL), Oak Ridge, TN (United States), ORNL/TM-2018/944, Sep. 2018. doi: 10.2172/1474561.

[17] D. E. Holcomb, J. A. King, and C. P. Chwasz, "Liquid Fuel Qualification for Molten Salt Reactors: Identification of Gaps and Challenges," Idaho National Laboratory (INL), Idaho Falls, ID (United States), INL/RPT-24-80651-Rev000, Sep. 2024. Accessed: Apr. 07, 2026. [Online]. Available: https://www.osti.gov/biblio/2477043

[18] *ANSI/ANS-20.2-2023 - Nuclear Safety Design Criteria and Functional Performance Requirements for Liquid-Fuel Molten Salt Reactor Nuclear Power Plants*, Jan. 04, 2024. Accessed: Apr. 24, 2026. [Online]. Available: https://webstore.ansi.org/standards/ansi/ansians202023?srsltid=AfmBOooszd_RxAmckR3P5A1hv64L9dPeU5HVTt4pMeWUTB6M6lQqNExi

[19] D. Holcomb, W. Poore (Retired), and G. Flanagan, "Fuel Qualification for Molten Salt Reactors (NUREG/CR-7299, ORNL/TM-2022/2754) | Nuclear Regulatory Commission," Office of Nuclear Reactor Regulation U.S. Nuclear Regulatory Commission Washington DC 20555-0001, NUREG/CR-7299, Dec. 2022. Accessed: Apr. 08, 2026. [Online]. Available: https://www.nrc.gov/reading-rm/doc-collections/nuregs/contract/cr7299/index

[20] S. Fayfar *et al.*, "Complex Structure of Molten FLiBe (2 Li F – Be F 2) Examined by Experimental Neutron Scattering, X-Ray Scattering, and Deep-Neural-Network Based Molecular Dynamics," *PRX Energy*, vol. 3, no. 1, p. 013001, Jan. 2024, doi: 10.1103/PRXEnergy.3.013001.

[21] C. Forsberg, G. (Tony) Zheng, R. G. Ballinger, and S. T. Lam, "Fusion Blankets and Fluoride-Salt-Cooled High-Temperature Reactors with Flibe Salt Coolant: Common Challenges, Tritium Control, and Opportunities for Synergistic Development Strategies Between Fission, Fusion, and Solar Salt Technologies," *Nucl. Technol.*, vol. 206, no. 11, pp. 1778–1801, Nov. 2020, doi: 10.1080/00295450.2019.1691400.

[22] B. N. Sorbom *et al.*, "ARC: A compact, high-field, fusion nuclear science facility and demonstration power plant with demountable magnets," *Fusion Eng. Des.*, vol. 100, pp. 378–405, Nov. 2015, doi: 10.1016/j.fusengdes.2015.07.008.

[23] C. Andreades *et al.*, "Design Summary of the Mark-I Pebble-Bed, Fluoride Salt–Cooled, High-Temperature Reactor Commercial Power Plant," *Nucl. Technol.*, vol. 195, no. 3, pp. 223–238, Sep. 2016, doi: 10.13182/NT16-2.

[24] C. F. Baes, "A polymer model for BeF2 and SiO2 melts," *J. Solid State Chem.*, vol. 1, no. 2, pp. 159–169, Jan. 1970, doi: 10.1016/0022-4596(70)90008-3.

[25] A. Rahman, R. H. Fowler, and A. H. Narten, "Structure and Motion in Liquid BeF2, LiBeF3, and LiF from Molecular Dynamics Calculations," *J. Chem. Phys.*, vol. 57, no. 7, pp. 3010–3011, Oct. 1972, doi: 10.1063/1.1678700.

[26] M. Salanne, C. Simon, P. Turq, R. J. Heaton, and P. A. Madden, "A First-Principles Description of Liquid BeF2 and Its Mixtures with LiF: 2. Network Formation in LiF−BeF2," *J. Phys. Chem. B*, vol. 110, no. 23, pp. 11461–11467, Jun. 2006, doi: 10.1021/jp061002u.

[27] A. L. Smith, E. Capelli, R. J. M. Konings, and A. E. Gheribi, "A new approach for coupled modelling of the structural and thermo-physical properties of molten salts. Case of a polymeric liquid LiF-BeF2," *J. Mol. Liq.*, vol. 299, p. 112165, Feb. 2020, doi: 10.1016/j.molliq.2019.112165.

[28] N. Winner, H. Williams, R. O. Scarlat, and M. Asta, "Ab-initio simulation studies of chromium solvation in molten fluoride salts," *J. Mol. Liq.*, vol. 335, p. 116351, Aug. 2021, doi: 10.1016/j.molliq.2021.116351.

[29] J. Dai, H. Han, Q. Li, and P. Huai, “First-principle investigation of the structure and vibrational spectra of the local structures in LiF–BeF2 Molten Salts,” *J. Mol. Liq.*, vol. 213, pp. 17–22, Jan. 2016, doi: 10.1016/j.molliq.2015.10.053.

[30] K. Baral, S. San, R. Sakidja, A. Couet, K. Sridharan, and W.-Y. Ching, “Temperature-Dependent Properties of Molten Li2BeF4 Salt Using Ab Initio Molecular Dynamics,” *ACS Omega*, 2021.

[31] S. Attarian, D. Morgan, and I. Szlufarska, “Thermophysical properties of FLiBe using moment tensor potentials,” *J. Mol. Liq.*, vol. 368, p. 120803, Dec. 2022, doi: 10.1016/j.molliq.2022.120803.

[32] A. Rodriguez, S. Lam, and M. Hu, “Thermodynamic and Transport Properties of LiF and FLiBe Molten Salts with Deep Learning Potentials,” *ACS Appl Mater Interfaces*, 2021.

[33] S. T. Lam, Q.-J. Li, R. Ballinger, C. Forsberg, and J. Li, “Modeling LiF and FLiBe Molten Salts with Robust Neural Network Interatomic Potential,” *ACS Appl. Mater. Interfaces*, vol. 13, no. 21, pp. 24582–24592, Jun. 2021, doi: 10.1021/acsami.1c00604.

[34] F. Vaslow and A. H. Narten, “Diffraction pattern and structure of molten BeF_2–LiF solutions,” *J. Chem. Phys.*, vol. 59, no. 9, pp. 4949–4954, Nov. 1973, doi: 10.1063/1.1680711.

[35] A. S. Quist, J. B. Bates, and G. E. Boyd, “Raman spectra of tetrafluoroberyllate ion in molten sodium fluoride and lithium fluoride to 686.deg.,” *J. Phys. Chem.*, vol. 76, no. 1, pp. 78–83, Jan. 1972, doi: 10.1021/j100645a014.

[36] L. M. Toth, J. B. Bates, and G. E. Boyd, “Raman spectra of Be2F73- and higher polymers of beryllium fluorides in the crystalline and molten state,” *J. Phys. Chem.*, vol. 77, no. 2, pp. 216–221, Jan. 1973, doi: 10.1021/j100621a014.

[37] G. E. Moore, “Chemistry Division Annual Progress Report for Period Ending May 20, 1974,” Oak Ridge National Lab., Tenn. (USA), United States, ORNL-4706, Oct. 1974.

[38] Y. Li, X. Liu, B. Wang, and C. Wang, “Raman and theoretical studies on structural evolution of Li2BeF4 and binary LiF-BeF2 melts,” *J. Mol. Liq.*, vol. 325, p. 115208, Mar. 2021, doi: 10.1016/j.molliq.2020.115208.

[39] W. R. Busing, “Interpretation of the Crystal Structure of Li2BeF4 in Terms of the Born-Mayer-Huggins Model,” *J. Chem. Phys.*, vol. 57, no. 7, pp. 3008–3010, Oct. 1972, doi: 10.1063/1.1678699.

[40] J. H. Burns and E. K. Gordon, “Refinement of the crystal structure of Li_2BeF_4,” *Acta Crystallogr.*, vol. 20, no. 1, pp. 135–138, Jan. 1966, doi: 10.1107/S0365110X66000240.

[41] Seiler, Paul, “Estimation of Ionicity Coefficients in Li2BeF4 Crystals by X-ray Diffraction,” *Acta Cryst*, vol. B49, pp. 223–235, 1993.

[42] D. M. Collins, M. C. Mahar, and F. W. Whitehurst, “Bonding in lithium tetrafluoroberyllate(II),” *Acta Crystallogr. B*, vol. 39, no. 3, pp. 303–306, Jun. 1983, doi: 10.1107/S010876818300244X.

[43] K. Momma and F. Izumi, “VESTA 3 for Three-Dimensional Visualization of Crystal, Volumetric and Morphology Data,” *J. Appl. Crystallogr.*, vol. 44, no. 6, pp. 1272–1276, Dec. 2011, doi: 10.1107/S0021889811038970.

[44] T. Hahn, Ed., *International Tables for Crystallography*, 5th ed., vol. A, Space Group Symmetry. 2001.

[45] D. Zagorac, H. Müller, S. Ruehl, J. Zagorac, and S. Rehme, “Recent developments in the Inorganic Crystal Structure Database: theoretical crystal structure data and related features,” *J. Appl.*

Crystallogr., vol. 52, no. 5, pp. 918–925, Oct. 2019, doi: 10.1107/S160057671900997X.

[46] D. Zagorac, H. Muller, S. Ruehl, J. Zagorac, and S. Rehme, *Inorganic Crystal Structure Database*. (2023). FIZ Karlsruhe GmbH.

[47] R. H. Guymon, "MSRE systems and components performance," ORNL-TM--3039, 4462915, Jun. 1973. doi: 10.2172/4462915.

[48] B. M. Chisholm, S. L. Krahn, and A. G. Sowder, "A unique molten salt reactor feature – The freeze valve system: Design, operating experience, and reliability," *Nucl. Eng. Des.*, vol. 368, p. 110803, Nov. 2020, doi: 10.1016/j.nucengdes.2020.110803.

[49] R. M. Hazen and L. W. Finger, "High-temperature crystal chemistry of phenakite (Be2SiO4) and chrysoberyl (BeAl2O4)," *Phys. Chem. Miner.*, vol. 14, no. 5, pp. 426–434, 1987, doi: 10.1007/BF00628819.

[50] F. A. Hummel, "Observations on the Thermal Expansion of Crystalline and Glassy Substances," *J. Am. Ceram. Soc.*, vol. 33, no. 3, pp. 102–107, Mar. 1950, doi: 10.1111/j.1151-2916.1950.tb12769.x.

[51] R. Vidrio, S. Mastromarino, E. Still, L. Chapdelaine, and R. O. Scarlat, "Density and Thermal Expansivity of Molten 2LiF-BeF2 (FLiBe): Measurements and Uncertainty Quantification," *J. Chem. Eng. Data*, vol. 67, no. 12, pp. 3517–3531, Dec. 2022, doi: 10.1021/acs.jced.2c00212.

[52] F. Carotti, B. Goh, M. Shafer, and R. O. Scarlat, "Datasets for elemental composition of 2LiF-BeF2 (FLiBe) salt purified by hydro-fluorination, analyzed by inductively coupled plasma mass spectrometry (ICP-MS) using two digestion methods," *Data Brief*, vol. 21, pp. 1612–1617, Dec. 2018, doi: 10.1016/j.dib.2018.09.053.

[53] K. Dolan, G. Zheng, K. Sun, D. Carpenter, and L. Hu, "Tritium generation, release, and retention from in-core fluoride salt irradiations," *Prog. Nucl. Energy*, vol. 131, p. 103576, Jan. 2021, doi: 10.1016/j.pnucene.2020.103576.

[54] J. Neuefeind, M. Feygenson, J. Carruth, R. Hoffmann, and K. K. Chipley, "The Nanoscale Ordered MAterials Diffractometer NOMAD at the Spallation Neutron Source SNS," *Nucl. Instrum. Methods Phys. Res. Sect. B Beam Interact. Mater. At.*, vol. 287, pp. 68–75, Sep. 2012, doi: 10.1016/j.nimb.2012.05.037.

[55] H.-R. Wenk, L. Lutterotti, and S. Vogel, "Texture analysis with the new HIPPO TOF diffractometer," *Nucl. Instrum. Methods Phys. Res. Sect. Accel. Spectrometers Detect. Assoc. Equip.*, vol. 515, no. 3, pp. 575–588, 2003.

[56] S. C. Vogel, C. Hartig, L. Lutterotti, R. B. Von Dreele, H.-R. Wenk, and D. J. Williams, "Texture measurements using the new neutron diffractometer HIPPO and their analysis using the Rietveld method," *Powder Diffr.*, vol. 19, no. 1, pp. 65–68, 2004.

[57] P. W. Lisowski and K. F. Schoenberg, "The Los Alamos neutron science center," *Nucl. Instrum. Methods Phys. Res. Sect. Accel. Spectrometers Detect. Assoc. Equip.*, vol. 562, no. 2, pp. 910–914, 2006.

[58] S. Matthies, J. Pehl, H.-R. Wenk, L. Lutterotti, and S. C. Vogel, "Quantitative texture analysis with the HIPPO neutron TOF diffractometer," *J. Appl. Crystallogr.*, vol. 38, no. 3, pp. 462–475, Jun. 2005, doi: 10.1107/S0021889805006187.

[59] K. A. Romberger, J. Braustein, and R. E. Thoma, "New electrochemical measurements of the liquidus in the lithium fluoride-beryllium fluoride system. Congruency of lithium beryllium fluoride (Li2BeF4)," *J. Phys. Chem.*, vol. 76, no. 8, pp. 1154–1159, Apr. 1972, doi: 10.1021/j100652a012.

[60] S. Takajo and S. C. Vogel, "Determination of pole figure coverage for texture

measurements with neutron time-of-flight diffractometers," *J. Appl. Crystallogr.*, vol. 51, no. 3, pp. 895–900, 2018.

[61] A. S. Losko, S. C. Vogel, H. M. Reiche, and H. Nakotte, "A six-axis robotic sample changer for high-throughput neutron powder diffraction and texture measurements," *J. Appl. Crystallogr.*, vol. 47, no. 6, pp. 2109–2112, Dec. 2014, doi: 10.1107/S1600576714021797.

[62] O. Ivashkevych *et al.*, "Hard X-Ray Pair Distribution Function (PDF) Beamline and End-Station Control System," in *17th International Conference on Accelerator and Large Experimental Physics Control Systems (ICALEPCS'19), New York, NY, USA, 05-11 October 2019*, JACOW Publishing, Geneva, Switzerland, Aug. 2020, pp. 1584–1589. doi: 10.18429/JACoW-ICALEPCS2019-THBPP04.

[63] B. H. Toby and R. B. Von Dreele, "*GSAS-II* : the genesis of a modern open-source all purpose crystallography software package," *J. Appl. Crystallogr.*, vol. 46, no. 2, pp. 544–549, Apr. 2013, doi: 10.1107/S0021889813003531.

[64] H. M. Rietveld, "A profile refinement method for nuclear and magnetic structures," *J. Appl. Crystallogr.*, vol. 2, no. 2, pp. 65–71, Jun. 1969, doi: 10.1107/S0021889869006558.

[65] S. C. Vogel, "gsaslanguage: a *GSAS* script language for automated Rietveld refinements of diffraction data," *J. Appl. Crystallogr.*, vol. 44, no. 4, pp. 873–877, Aug. 2011, doi: 10.1107/S0021889811023181.

[66] S. C. Vogel *et al.*, "Crystal Structure Evolution of UCl3 from Room Temperature to Melting," *JOM*, vol. 73, no. 11, pp. 3555–3563, Nov. 2021, doi: 10.1007/s11837-021-04893-7.

[67] H.-R. Wenk, L. Lutterotti, and S. C. Vogel, "Rietveld texture analysis from TOF neutron diffraction data," *Powder Diffr.*, vol. 25, no. 3, pp. 283–296, Sep. 2010, doi: 10.1154/1.3479004.

[68] T. Williams and C. Kelley, *Gnuplot*. (1993, 1998, 2004 1986). Accessed: Jul. 25, 2023. [MS Windows]. Available: http://www.gnuplot.info/

[69] Weber, Steffen, *KrystalShaper*. JCrystalSoft. Accessed: Jul. 26, 2023. [Online]. Available: http://www.jcrystal.com/

[70] N. Gnyra, *nicoco007/Propagation-of-Uncertainty-Calculator*. (May 31, 2024). TypeScript. Accessed: Jun. 27, 2024. [Online]. Available: https://github.com/nicoco007/Propagation-of-Uncertainty-Calculator

[71] C. F. Macrae *et al.*, "*Mercury 4.0* : from visualization to analysis, design and prediction," *J. Appl. Crystallogr.*, vol. 53, no. 1, pp. 226–235, Feb. 2020, doi: 10.1107/S1600576719014092.

[72] C. R. Groom, I. J. Bruno, M. P. Lightfoot, and S. C. Ward, "The Cambridge Structural Database," *Acta Crystallogr. Sect. B Struct. Sci. Cryst. Eng. Mater.*, vol. 72, no. 2, Art. no. 2, Apr. 2016, doi: 10.1107/S2052520616003954.

[73] F. Schoonjans, "MedCalc's Comparison of means calculator," MedCalc. Accessed: Feb. 29, 2024. [Online]. Available: https://www.medcalc.org/calc/comparison_of_means.php

[74] A.-T. Duong, "Temperature Gradient: A Simple Method for Single Crystal Growth," *VNU J. Sci. Math. - Phys.*, vol. 35, no. 1, Mar. 2019, doi: 10.25073/2588-1124/vnumap.4311.

[75] National Research Council and Molten Salt Panel of the Committee on Remediation of Buried and Tank Wastes, *Evaluation of the U.S. Department of Energy's Alternatives for the Removal and Disposition of Molten Salt Reactor Experiment Fluoride Salts*. Washington, D.C.: National Academies Press, 1997. doi: 10.17226/5538.

[76] Y. Liu, S. Che, A. Burak, D. L. Barth, N. Zweibaum, and M. Chen, "Numerical Investigations of Molten Salt Pump Journal Bearings Under Hydrodynamic Lubrication Conditions for

FHRs," *Nucl. Sci. Eng.*, vol. 197, no. 5, pp. 907–919, May 2023, doi: 10.1080/00295639.2022.2103343.

[77] T. J. Price, O. Chvala, and Z. Taylor, "Xenon in molten salt reactors: The effects of solubility, circulating particulate, ionization, and the sensitivity of the circulating void fraction," *Nucl. Eng. Technol.*, vol. 52, no. 6, pp. 1131–1136, Jun. 2020, doi: 10.1016/j.net.2019.11.026.

[78] S. Chiba, Toda ,Saburo, Yuki ,Kazuhisa, and A. and Sagara, "Heat Transfer Enhancement for a Molten Salt FLiBe Channel," *Fusion Technol.*, vol. 39, no. 2P2, pp. 779–783, Mar. 2001, doi: 10.13182/FST01-A11963333.

[79] M. Salanne, C. Simon, P. Turq, and P. A. Madden, "Conductivity−Viscosity−Structure: Unpicking the Relationship in an Ionic Liquid," *J. Phys. Chem. B*, vol. 111, no. 18, pp. 4678–4684, May 2007, doi: 10.1021/jp067073a.

[80] Y. Abe, O. Kosugiyama, and A. Nagashima, "Viscosity of LiF-BeF2 eutectic mixture (XBeF2 = 0.328) and LiF single salt at elevated temperatures," *J. Nucl. Mater.*, vol. 99, no. 2, pp. 173–183, Sep. 1981, doi: 10.1016/0022-3115(81)90186-0.

[81] S. Cantor, W. T. Ward, and C. T. Moynihan, "Viscosity and Density in Molten BeF2–LiF Solutions," *J. Chem. Phys.*, vol. 50, no. 7, pp. 2874–2879, Apr. 1969, doi: 10.1063/1.1671478.

[82] A. V. Merzlyakov and V. V. Ignat'ev, "Measurement of the Kinematic Viscosity of Melted Mixtures of Sodium, Lithium, and Beryllium Fluorides and the Effect of the Eutectic Additive Cerium Trifluoride on the Viscosity," *At. Energy*, vol. 124, no. 4, pp. 251–254, Aug. 2018, doi: 10.1007/s10512-018-0406-5.

[83] X. Zhang *et al.*, "Local structure and thermophysical properties of the molten salt FNaBe through ab initio molecular dynamics and experimental measurements," *Mater. Today Commun.*, vol. 42, p. 111193, Jan. 2025, doi: 10.1016/j.mtcomm.2024.111193.

[84] J. A. Ocádiz-Flores *et al.*, "New insights and coupled modelling of the structural and thermodynamic properties of the LiF-UF4 system," *J. Mol. Liq.*, vol. 331, p. 115820, Jun. 2021, doi: 10.1016/j.molliq.2021.115820.

[85] K. Zheng, N. Marcella, A. L. Smith, and A. I. Frenkel, "Decoding the Pair Distribution Function of Uranium in Molten Fluoride Salts from X-Ray Absorption Spectroscopy Data by Machine Learning," *J. Phys. Chem. C*, vol. 128, no. 18, pp. 7635–7642, May 2024, doi: 10.1021/acs.jpcc.4c01898.

[86] R. Chahal, S. Banerjee, and S. T. Lam, "Short- to Intermediate-Range Structure, Transport, and Thermophysical Properties of LiF–NaF–ZrF4 Molten Salts," *Front. Phys.*, vol. 10, 2022, doi: 10.3389/fphy.2022.830468.

[87] X. Li, "Influence of ZrF4 additive on the local structures and thermophysical properties of molten NaF-BeF2," *J. Mol. Liq.*, vol. 393, p. 123681, Jan. 2024, doi: 10.1016/j.molliq.2023.123681.

[88] "Thermocouple Response Time," https://www.dwyeromega.com/en-us/. Accessed: Apr. 30, 2025. [Online]. Available: https://www.dwyeromega.com/en-us/resources/thermocouples-response-time

[89] G. D. Young, "A Mathematical Technique for Estimating True Temperature Profiles of Data Obtained from Long Time Constant Thermocouples," *DSTO Aeronautical and Maritime Research Laboratory*, Feb. 1998, Accessed: Aug. 08, 2025. [Online]. Available: https://apps.dtic.mil/sti/tr/pdf/ADA348299.pdf

[90] "Linear Thermal Expansion Coefficients of Materials." Accessed: Apr. 16, 2025. [Online]. Available: https://www.engineeringtoolbox.com/linear-expansion-coefficients-d_95.html

[91] S. I. Cohen and T. N. Jones, "VISCOSITY MEASUREMENTS ON MOLTEN FLUORIDE MIXTURES," ORNL-2278, 4803933, Jul. 1957. doi: 10.2172/4803933.

[92] S. Cantor, “PHYSICAL PROPERTIES OF MOLTEN-SALT REACTOR FUEL, COOLANT, AND FLUSH SALTS.,” ORNL-TM--2316, 4492893, Oct. 1968. doi: 10.2172/4492893.

[93] R. R. Romatoski and L. W. Hu, “Fluoride salt coolant properties for nuclear reactor applications: A review,” *Ann. Nucl. Energy*, vol. 109, pp. 635–647, Nov. 2017, doi: 10.1016/j.anucene.2017.05.036.

[94] P. Gierszowski, B. Mikic, and N. Todreas, “Property correlations for lithium, sodium, helium, flibe and water in fusion reactor applications,” Jan. 1980, Accessed: Apr. 15, 2025. [Online]. Available: https://dspace.mit.edu/handle/1721.1/93392

[95] G. J. Janz, G. L. Gardner, U. Krebs, and R. P. T. Tomkins, “Molten Salts: Volume 4, Part 1, Fluorides and Mixtures Electrical Conductance, Density, Viscosity, and Surface Tension Data,” *J. Phys. Chem. Ref. Data*, vol. 3, no. 1, pp. 1–115, Jan. 1974, doi: 10.1063/1.3253134.

[96] J. Park, W. Zhuo, C. Ridder, A. Leong, and J. Zhang, “Thermophysical and thermodynamic properties of NaF-BeF2-UF4-ZrF4 fuel salt,” *Mater. Today Commun.*, vol. 37, p. 107211, Dec. 2023, doi: 10.1016/j.mtcomm.2023.107211.

[97] R. D. Shannon, “Revised effective ionic radii and systematic studies of interatomic distances in halides and chalcogenides,” *Acta Crystallogr. A*, vol. 32, no. 5, pp. 751–767, Sep. 1976, doi: 10.1107/S0567739476001551.

[98] W. R. Grimes, “Reactor Chemistry Division annual progress report for period ending December 31, 1965,” Oak Ridge National Laboratory, Oak Ridge, TN, ORNL-3913, Mar. 1966.

[99] A. V. Krylosov, I. B. Polovov, and O. I. Rebrin, “Density and Electrical Conductivity of Molten Beryllium Fluoride–Alkali-Metal Chloride Salt Mixtures,” *Russ. Metall. Met.*, vol. 2023, no. 2, pp. 229–234, Feb. 2023, doi: 10.1134/S003602952302012X.

[100] A. Birri, R. Chesser, N. Termini, J. C. Numbers, K. Garland, and M. A. Rose, “Reference Correlations for the Density and Viscosity of Molten Alkali and Alkaline Earth Fluoride Salts,” *J. Phys. Chem. Ref. Data*, vol. 54, no. 2, p. 023101, May 2025, doi: 10.1063/5.0264576.

[101] B. Blanke, K. Foster, L. Jones, K. Jordan, R. Joyner, and E. Murphy, “VISCOSITY OF FUSED MIXTURES OF SODIUM FLUORIDE, BERYLLIUM FLUORIDE, AND URANIUM FLUORIDE,” MLM–1079, 4303840, Apr. 1956. doi: 10.2172/4303840.

[102] W. D. Powers, S. I. Cohen, and N. D. Greene, “Physical Properties of Molten Reactor Fuels and Coolants,” *Nucl. Sci. Eng.*, vol. 17, no. 2, pp. 200–211, Oct. 1963, doi: 10.13182/NSE63-5.

[103] Wolfram Research, Inc., *Mathematica*. (2024). Wolfram Research, Inc., Champaign, Illinois. Accessed: Aug. 25, 2025. [Online]. Available: https://www.wolfram.com/mathematica

[104] *Origin(Pro)*. OriginLab Corporation, Northampton, MA, USA. Accessed: Aug. 25, 2025. [Online]. Available: https://www.originlab.com/

[105] B. C. Blanke, E. N. Bousquet, M. L. Curtis, and E. L. Murphy, “DENSITY AND VISCOSITY OF FUSED MIXTURES OF LITHIUM, BERYLLIUM, AND URANIUM FLUORIDES,” MLM–1086, 4274391, Dec. 1956. doi: 10.2172/4274391.

[106] O. Yu. Tkacheva, A. V. Rudenko, A. A. Kataev, P. N. Mushnikov, A. S. Kholkina, and Yu. P. Zaikov, “The Viscosity of Molten Salts Based on the LiF–BeF2 System,” *Russ. J. Non-Ferr. Met.*, vol. 63, no. 3, pp. 276–283, Jun. 2022, doi: 10.3103/S1067821222030117.

[107] C. T. Moynihan and S. Cantor, “Viscosity and Its Temperature Dependence in Molten BeF2,” *J. Chem. Phys.*, vol. 48, no. 1, pp. 115–119, Jan. 1968, doi: 10.1063/1.1664455.

[108] W. R. Grimes, F. F. Blankenship, G. W. Keilholtz, H. F. Poppendiek, and M. T.

Robinson, “Chemical Aspects of Molten Fluoride Reactors,” Oak Ridge National Laboratory (ORNL), Oak Ridge, TN (United States), A/CONF.15/P/448, Jun. 1958. doi: 10.2172/4305506.

[109] X. Fu *et al.*, “Probing the local structure of FLiBe melts and solidified salts by in situ high-temperature NMR,” *Phys. Chem. Chem. Phys.*, vol. 25, no. 29, pp. 19446–19452, 2023, doi: 10.1039/D3CP01096A.

[110] A. Cavagna, “Supercooled liquids for pedestrians,” *Phys. Rep.*, vol. 476, no. 4, pp. 51–124, Jun. 2009, doi: 10.1016/j.physrep.2009.03.003.

[111] Q. Wu, J. Ruan, B. Huang, Z. Zhou, and J. Zou, “Viscoelastic Behavior and Ability of Dissipating Energy of SiO2 Dispersions under Stress Shear,” *Acta Phys.-Chim. Sin.*, vol. 22, no. 9, pp. 1075–1078, Sep. 2006, doi: 10.1016/S1872-1508(06)60047-8.

[112] D. Moneghan, “Technology Insight Brief: Molten Salt Reactors,” Dec. 2020. Accessed: Nov. 15, 2024. [Online]. Available: https://www.epri.com/research/programs/065093/results/3002020066

[113] Z. Mausolff, M. DeHart, and S. Goluoglu, “Design and assessment of a molten chloride fast reactor,” *Nucl. Eng. Des.*, vol. 379, p. 111181, Aug. 2021, doi: 10.1016/j.nucengdes.2021.111181.

[114] M. Branco-Katcher, D. Siefman, R. Araj, T. Cisernos, C. Percher, and T. S. Palmer, “Design Optimization of a Criticality Experiment for the Molten Chloride Reactor Experiment Facility,” *Nucl. Sci. Eng.*, Mar. 2025, doi: 10.1080/00295639.2025.2464459.

[115] E. S. Sooby, A. T. Nelson, J. T. White, and P. M. McIntyre, “Measurements of the liquidus surface and solidus transitions of the NaCl–UCl3 and NaCl–UCl3–CeCl3 phase diagrams,” *J. Nucl. Mater.*, vol. 466, pp. 280–285, Nov. 2015, doi: 10.1016/j.jnucmat.2015.07.050.

[116] J. Shi and M. Fratoni, *Fuel salt compressibility effects in molten salt reactors*. United States: ANS - American Nuclear Society, 2021.

[117] A. Abou-Jaoude *et al.*, “A workflow leveraging MOOSE transient multiphysics simulations to evaluate the impact of thermophysical property uncertainties on molten-salt reactors,” *Ann. Nucl. Energy*, vol. 163, p. 108546, Dec. 2021, doi: 10.1016/j.anucene.2021.108546.

[118] J. Lonergan *et al.*, “Thermodynamic investigation of the NaCl-KCl salt system from 25 to 950 °C,” *J. Mol. Liq.*, vol. 391, no. Part A, Art. no. PNNL-SA--179759, Jul. 2023, doi: 10.1016/j.molliq.2023.122591.

[119] T. Xu, X. Li, Y. Wang, and Z. Tang, “Development of Deep Potentials of Molten MgCl2–NaCl and MgCl2–KCl Salts Driven by Machine Learning,” *ACS Appl. Mater. Interfaces*, vol. 15, no. 11, pp. 14184–14195, Mar. 2023, doi: 10.1021/acsami.2c19272.

[120] K. Arndt and A. Geßler, “Dichte und Äquivalentleitfähigkeit einiger geschmolzener Salze,” *Z. Für Elektrochem. Angew. Phys. Chem.*, vol. 14, no. 39, pp. 665–667, 1908, doi: 10.1002/bbpc.19080143904.

[121] E. Brunner, “Die Dichten geschmolzener Salze und das chemische Gleichgewicht ihrer Mischungen,” *Z. Für Anorg. Chem.*, vol. 38, no. 1, pp. 350–376, 1904, doi: 10.1002/zaac.19040380128.

[122] K. Honda and H. Endo, “Die Volumenänderung von Gußeisen beim Erstarren, nebst einer Kritik des Doppeldiagramms des Systemes Eisen-Kohlenstoff,” *Z. Für Anorg. Allg. Chem.*, vol. 154, no. 1, pp. 238–252, 1926, doi: 10.1002/zaac.19261540123.

[123] F. M. Jaeger, “Über die Temperaturabhängigkeit der molekularen freien Oberflächenenergie von Flüssigkeiten im Temperaturbereich von − 80 bis + 1650° C,” *Z. Für Anorg. Allg. Chem.*, vol. 101, no. 1, pp. 1–214, 1917, doi: 10.1002/zaac.19171010102.

[124] A. D. Kirshenbaum, J. A. Cahill, P. J. McGonigal, and A. V. Grosse, “The density of

liquid NaCl and KCl and an estimate of their critical constants together with those of the other alkali halides," *J. Inorg. Nucl. Chem.*, vol. 24, no. 10, pp. 1287–1296, Dec. 1962, doi: 10.1016/0022-1902(62)80205-X.

[125] B. Lorenz, H. Frei, and A. Jabs, "Dichten einiger geschmolzener Salze und deren Mischungen bei verschiedenen Temperaturen," *Z. Für Phys. Chem.*, vol. 61U, no. 1, pp. 468–474, Oct. 1908, doi: 10.1515/zpch-1908-6135.

[126] J. N. Reding, "Densities and Molal Volumes of Molten Magnesium Chloride, Potassium Chloride, and Barium Chloride Mixtures.," *J. Chem. Eng. Data*, vol. 10, no. 1, pp. 1–4, Jan. 1965, doi: 10.1021/je60024a001.

[127] N. S. Kurnakow and S. F. Żmczużnyj, "Isomorphismus der Kalium- und Natriumverbindungen," *Z. Für Anorg. Chem.*, vol. 52, no. 1, pp. 186–201, 1907, doi: 10.1002/zaac.19070520118.

[128] D. F. Williams, "Assessment of Candidate Molten Salt Coolants for the NGNP/NHI Heat-Transfer Loop," Oak Ridge National Lab. (ORNL), Oak Ridge, TN (United States), ORNL/TM-2006/69, Jun. 2006. doi: 10.2172/1360677.

[129] V. N. Desyatnik, S. F. Katyshev, S. P. Raspopin, and Yu. F. Chervinskii, "Density, surface tension, and viscosity of uranium trichloride-sodium chloride melts," *Sov. At. Energy*, vol. 39, no. 1, pp. 649–651, Jul. 1975, doi: 10.1007/BF01121527.

[130] G. I. L. van Oudenaren, J. A. Ocadiz-Flores, and A. L. Smith, "Coupled structural-thermodynamic modelling of the molten salt system NaCl-UCl3," *J. Mol. Liq.*, vol. 342, p. 117470, Nov. 2021, doi: 10.1016/j.molliq.2021.117470.

[131] M. Simoes Santos, M. Salanne, T. Kooyman, and D. Lambertin, "Structural and transport properties of the molten salt NaCl-KCl-UCl3 using the polarizable ion model," *J. Nucl. Mater.*, vol. 597, p. 155125, Aug. 2024, doi: 10.1016/j.jnucmat.2024.155125.

[132] B. Li, S. Dai, and D. Jiang, "First-Principles Molecular Dynamics Simulations of UCln–NaCl (n = 3, 4) Molten Salts," *ACS Appl. Energy Mater.*, vol. 2, no. 3, pp. 2122–2128, Mar. 2019, doi: 10.1021/acsaem.8b02157.

[133] D. A. Andersson and B. W. Beeler, "Ab initio molecular dynamics (AIMD) simulations of NaCl, UCl 3 and NaCl-UCl 3 molten salts," *J. Nucl. Mater.*, vol. 568, p. 153836, Sep. 2022, doi: 10.1016/j.jnucmat.2022.153836.

[134] D. N. Gardner, M. Denis, M. Borrello, C. Sclafani, and R. O. Scarlat, "The Effect of Complex Forming Cations on the Thermophysical Properties of Beryllium and Uranium Fluoride Salts for Nuclear Reactor Applications," *ACS Phys. Chem. Au*, Oct. 2025, doi: 10.1021/acsphyschemau.5c00043.

[135] R. Takagi and M. Tomita, "Structure of the Molten NaCl-MgCl2," *Z. Für Naturforschung A*, vol. 48, no. 12, pp. 1239–1242, Dec. 1993, doi: 10.1515/zna-1993-1216.

[136] Q.-J. Li *et al.*, "Complex Structure of Molten NaCl–CrCl3 Salt: Cr–Cl Octahedral Network and Intermediate-Range Order," *ACS Appl. Energy Mater.*, vol. 4, no. 4, pp. 3044–3056, Apr. 2021, doi: 10.1021/acsaem.0c02678.

[137] A. Y. Galashev and K. A. Ivanichkina, "Unraveling local structure of molten salt KF-KCl-KI via molecular dynamics simulation," *Chem. Phys.*, vol. 555, p. 111455, Mar. 2022, doi: 10.1016/j.chemphys.2022.111455.

[138] C. Agca and J. W. McMurray, "Empirical estimation of densities in NaCl-KCl-UCl3 and NaCl-KCl-YCl3 molten salts using Redlich-Kister expansion," *Chem. Eng. Sci.*, vol. 247, p. 117086, Jan.

2022, doi: 10.1016/j.ces.2021.117086.

[139] G. J. Janz *et al.*, “Molten salts: Volume 4, part 2, chlorides and mixtures—electrical conductance, density, viscosity, and surface tension data,” *J. Phys. Chem. Ref. Data*, vol. 4, no. 4, pp. 871–1178, Oct. 1975, doi: 10.1063/1.555527.

[140] E. R. Buckle and P. E. Tsaoussoglou, “Molar Volumes in Molten KCl, RbCl, TlCl, KCl-TlCl, and RbCl-TlCl,” *Z. Für Naturforschung A*, vol. 27, no. 12, pp. 1759–1764, Dec. 1972, doi: 10.1515/zna-1972-1210.

[141] A. Bleise, P. R. Danesi, and W. Burkart, “Properties, use and health effects of depleted uranium (DU): a general overview,” *J. Environ. Radioact.*, vol. 64, no. 2, pp. 93–112, Jan. 2003, doi: 10.1016/S0265-931X(02)00041-3.

[142] N. O. of D. and Informatics, “Welcome to the NIST WebBook.” Accessed: May 27, 2025. [Online]. Available: https://webbook.nist.gov/

[143] T. Munro *et al.*, “Round Robin Measurements of Molten Salt Properties for LiF-NaF-KF (FLiNaK) and NaCl-KCl Mixtures,” *J. Chem. Eng. Data*, Oct. 2025, doi: 10.1021/acs.jced.5c00421.

[144] D. Sergeev, D. Kobertz, and M. Müller, “Thermodynamics of the NaCl–KCl system,” *Thermochim. Acta*, vol. 606, pp. 25–33, Apr. 2015, doi: 10.1016/j.tca.2015.03.003.

[145] K. Grjotheim, J. L. Holm, M. Røtnes, U. Rudén, and Å. Pilotti, “The Phase Diagrams of the Systems NaCl-MgCl2 and KCl-MgCl2.,” *Acta Chem. Scand.*, vol. 26, pp. 3802–3803, 1972, doi: 10.3891/acta.chem.scand.26-3802.

[146] D. C. Alders, B. A. S. Rooijakkers, R. J. M. Konings, and A. L. Smith, “Experimental Investigation and Thermodynamic Modeling Assessment of the NaCl–NaI–MgCl2–MgI2 Quaternary System,” *J. Phys. Chem. C*, vol. 129, no. 5, pp. 2726–2738, Feb. 2025, doi: 10.1021/acs.jpcc.4c07788.

[147] J. Mochinaga, H. Ohtani, and K. Igarashi, “Phase Diagram of Ternary DyCl3-KCl-NaCl System,” *Denki Kagaku Oyobi Kogyo Butsuri Kagaku*, vol. 49, no. 1, pp. 19–21, 1981, doi: 10.5796/kogyobutsurikagaku.49.19.

[148] G. Mohan, M. Venkataraman, J. Gomez-Vidal, and J. Coventry, “Assessment of a novel ternary eutectic chloride salt for next generation high-temperature sensible heat storage,” *Energy Convers. Manag.*, vol. 167, pp. 156–164, Jul. 2018, doi: 10.1016/j.enconman.2018.04.100.

[149] A. P. Armangdabriel, “Liquidus Measurements and Coupled Thermodynamic-Phase-diagram Analysis of the NaC1-KCl System”.

[150] S. S. Parker, A. Long, C. Lhermitte, S. Vogel, M. Monreal, and J. M. Jackson, “Thermophysical properties of liquid chlorides from 600 to 1600 K: Melt point, enthalpy of fusion, and volumetric expansion,” *J. Mol. Liq.*, vol. 346, p. 118147, Jan. 2022, doi: 10.1016/j.molliq.2021.118147.

[151] C. Kraus, “Phase Diagram of Some Complex Salts of Uranium with Halides of the Alkali and Alkaline Earth Metals,” This report was produced in 1943, well before there was an Atomic Energy Commission, M–251, Jul. 1943. doi: 10.2172/12687930.

[152] R. E. Thoma, *Phase Diagrams of Nuclear Reactor Materials*. Oak Ridge National Laboratory, 1962.

[153] M. A. Rose, L. D. Gardner, T. T. Lichtenstein, S. A. Thomas, and E. Wu, “Property Measurements of NaCl-UCl3 and NaCl-KCl-UCl3 Molten Salts (Rev.1),” Argonne National Laboratory (ANL), Argonne, IL (United States), ANL/CFCT-22/45-Rev.1, May 2023. doi: 10.2172/1985295.

[154] P. D. Myers and D. Y. Goswami, “Thermal energy storage using chloride salts and their eutectics,” *Appl. Therm. Eng.*, vol. 109, pp. 889–900, Oct. 2016, doi:

10.1016/j.applthermaleng.2016.07.046.

[155] D. F. Williams, “Assessment of Candidate Molten Salt Coolants for the Advanced High Temperature Reactor (AHTR),” ORNL/TM-2006/12, 885975, Mar. 2006. doi: 10.2172/885975.

[156] B. Cárdenas and N. León, “High temperature latent heat thermal energy storage: Phase change materials, design considerations and performance enhancement techniques,” *Renew. Sustain. Energy Rev.*, vol. 27, pp. 724–737, Nov. 2013, doi: 10.1016/j.rser.2013.07.028.

[157] T. Xu, X. Li, L. Guo, F. Wang, and Z. Tang, “Powerful predictability of FPMD simulations for the phase transition behavior of NaCl-MgCl2 eutectic salt,” *Sol. Energy*, vol. 209, pp. 568–575, Oct. 2020, doi: 10.1016/j.solener.2020.09.038.

[158] D. S. Coleman and P. D. A. Lacy, “The phase equilibrium diagram for the KCl-NaCl system,” *Mater. Res. Bull.*, vol. 2, no. 10, pp. 935–938, Oct. 1967, doi: 10.1016/0025-5408(67)90149-3.

[159] A. D. Pelton, A. Gabriel, and J. Sangster, “Liquidus measurements and coupled thermodynamic–phase-diagram analysis of the NaCl–KCl system,” *J. Chem. Soc. Faraday Trans. 1 Phys. Chem. Condens. Phases*, vol. 81, no. 5, pp. 1167–1172, Jan. 1985, doi: 10.1039/F19858101167.

[160] J. Moon *et al.*, “Density Measurements of Various Molten Sodium, Magnesium, Potassium, and Uranium Chloride Salt Compositions Using Neutron Imaging,” *Ind. Eng. Chem. Res.*, vol. 61, no. 48, pp. 17665–17673, Dec. 2022, doi: 10.1021/acs.iecr.2c02967.

[161] E. R. Van Artsdalen and I. S. Yaffe, “Electrical Conductance and Density of Molten Salt Systems: KCl–LiCl, KCl–NaCl and KCl–KI,” *J. Phys. Chem.*, vol. 59, no. 2, pp. 118–127, Feb. 1955, doi: 10.1021/j150524a007.

[162] J. Ye and Y. Sahai, “Surface Tension and Density of Molten Salts Based on Equimolar NaCl–KCl with Addition of Fluorides,” *Mater. Trans. JIM*, vol. 37, no. 2, pp. 170–174, 1996, doi: 10.2320/matertrans1989.37.170.

[163] K, Cho, T. Kuroda, J. Mochinaga, R. Takagi, and K. Denki, “Densities and equivalent conductivities of molten uranium trichloride and uranium trichloride-potassium chloride systems,” *J Electrochem Soc Jpn.*, vol. 37, no. 9, pp. 654–658, 1969.

[164] N. Termini *et al.*, “FY24 Progress Report on Viscosity and Thermal Conductivity Measurements of Nuclear Industry Relevant Chloride Salts: An Experimental and Computational Study,” ORNL/TM--2024/3650, 2477502, Oct. 2024. doi: 10.2172/2477502.

[165] A. Birri, N. Termini, P. Rose, S. Chapel, H. Andrews, and N. D. Bull Ezell, “Development and demonstration of a rolling ball viscometer for molten salts with near-minimum liquidus NaCl–KCl,” *Therm. Sci. Eng. Prog.*, vol. 44, p. 102029, Sep. 2023, doi: 10.1016/j.tsep.2023.102029.

[166] “Common Techniques to Calibrate Thermocouples,” https://www.dwyeromega.com/en-us/. Accessed: Jun. 04, 2025. [Online]. Available: https://www.dwyeromega.com/en-us/resources/calibrating-thermocouples

[167] A. Kruizenga, “Corrosion mechanisms in chloride and carbonate salts.,” SAND2012-7594, 1051732, Sep. 2012. doi: 10.2172/1051732.

[168] H. Kim, C. Kwon, S. Ham, J. Lee, S. J. Kim, and S. Kim, “Physical properties of KCl-UCl3 molten salts as potential fuels for molten salt reactors,” *J. Nucl. Mater.*, vol. 577, p. 154329, Apr. 2023, doi: 10.1016/j.jnucmat.2023.154329.

[169] H. Zhang, M. L. Newton, D. E. Hamilton, and M. F. Simpson, “High temperature UCl3 synthesis in molten salt mixtures via reaction of U metal with iron chlorides,” *J. Radioanal. Nucl. Chem.*, vol. 331, no. 1, pp. 383–390, Jan. 2022, doi: 10.1007/s10967-021-08060-9.

[170] J. A. Yingling *et al.*, “Thermodynamic Assessment of CrCl2 with NaCl–KCl–MgCl2–UCl3–UCl4 for Molten Chloride Reactor Corrosion Modeling,” *ACS Appl. Energy Mater.*, vol. 6, no. 11, pp. 5868–5882, Jun. 2023, doi: 10.1021/acsaem.3c00306.

[171] M. L. Newton, D. E. Hamilton, and M. F. Simpson, “Methods of Redox Control and Measurement in Molten NaCl-CaCl2-UCl3,” *ECS Trans.*, vol. 98, no. 10, p. 19, Sep. 2020, doi: 10.1149/09810.0019ecst.

[172] J. Yankey, M. Monreal, M. Jackson, and M. Simpson, “Electrochemical Activity Measurements of UCl3 in Molten NaCl-MgCl2-UCl3,” *J. Nucl. Eng. Radiat. Sci.*, vol. 10, no. 030906, Mar. 2024, doi: 10.1115/1.4064598.

[173] N. Ullah *et al.*, *MCRE Design Description in Support of External Model Development*. 2023.

[174] M. S. Walls and K. D. Y. Spencer, “Molten Chloride Reactor Experiment,” vol. INL/MIS-23-73611-Revision-0, Jul. 2023.

[175] D. Olander, “Redox condition in molten fluoride salts,” *J. Nucl. Mater.*, vol. 300, no. 2–3, pp. 270–272, Feb. 2002, doi: 10.1016/S0022-3115(01)00742-5.

[176] H. Moriyama, S. Maeda, T. Ohmura, K. Moritani, and J. Oishi, “Chemical Behaviors of Tritium Formed in a LiF-BeF2 Mixture,” *J. Nucl. Mater.*, vol. 148, no. 2, pp. 211–216, Apr. 1987, doi: 10.1016/0022-3115(87)90115-2.

[177] F. Carotti, E. Liu, D. D. Macdonald, and R. O. Scarlat, “An electrochemical study of hydrogen in molten 2LiF-BeF2 (FLiBe) with addition of LiH,” *Electrochimica Acta*, vol. 367, p. 137114, Jan. 2021, doi: 10.1016/j.electacta.2020.137114.

[178] “ICSD - Details on Search Result.” Accessed: Dec. 04, 2023. [Online]. Available: https://icsd.fiz-karlsruhe.de/display/details.xhtml

[179] L. Lutterotti, S. Matthies, and H. Wenk, “MAUD: a friendly Java program for material analysis using diffraction,” 1999. Accessed: Apr. 27, 2026. [Online]. Available: https://www.semanticscholar.org/paper/MAUD%3A-a-friendly-Java-program-for-material-analysis-Lutterotti-Matthies/dfa20de1ce947fa432915ee9fcc9113b3736b59d

[180] G. S. Smith *et al.*, “The crystal and molecular structure of beryllium hydride,” *Solid State Commun.*, vol. 67, no. 5, pp. 491–494, Aug. 1988, doi: 10.1016/0038-1098(84)90168-6.

[181] G. Vidal-Valat, J.-P. Vidal, K. Kurki-Suonio, and R. Kurki-Suonio, “Evidence on the breakdown of the Born-Oppenheimer approximation in the charge density of crystalline 7LiH/D,” *Acta Crystallogr. A*, vol. 48, no. 1, pp. 46–60, Jan. 1992, doi: 10.1107/S0108767391008796.

[182] T. Mezger, *Applied Rheology: with Joe Flow on Rheology Road*, 8th edition. Graz: Anton Paar GmbH, 2021.

[183] D. Zhao, L. Yan, T. Jiang, S. Peng, and B. Yue, “On the viscosity of molten salts and molten salt mixtures and its temperature dependence,” *J. Energy Storage*, vol. 61, p. 106707, May 2023, doi: 10.1016/j.est.2023.106707.

[184] A. C. Wright, A. G. Clare, G. Etherington, R. N. Sinclair, S. A. Brawer, and M. J. Weber, “A neutron diffraction and molecular dynamics investigation of the structure of vitreous beryllium fluoride,” *J. Non-Cryst. Solids*, vol. 111, no. 2–3, pp. 139–152, Nov. 1989, doi: 10.1016/0022-3093(89)90275-5.

[185] L. G. Van Uitert, “Relations between melting point, glass transition temperature, and thermal expansion for inorganic crystals and glasses,” *J. Appl. Phys.*, vol. 50, no. 12, pp. 8052–8061, Dec. 1979, doi: 10.1063/1.325941.

[186] S. Li, Q. Huang, L. Wang, and K. Fan, “Research on viscoelastic properties of water in waxy crude oil emulsion gels with the effect of droplet size and distribution,” *Can. J. Chem. Eng.*, vol. 93, no. 12, pp. 2233–2244, 2015, doi: 10.1002/cjce.22324.

[187] D. Zhou, R. Liang, and Y. Kang, “A review of chemo-rheological and thermo-rheological investigations on epoxy asphalt cementitious materials,” *Constr. Build. Mater.*, vol. 395, p. 132309, Sep. 2023, doi: 10.1016/j.conbuildmat.2023.132309.

[188] V. Genovés, L. Maini, C. Roman, C. Hierold, and N. Cesarovic, “Variation in the viscoelastic properties of polydimethylsiloxane (PDMS) with the temperature at ultrasonic frequencies,” *Polym. Test.*, vol. 124, p. 108067, Jul. 2023, doi: 10.1016/j.polymertesting.2023.108067.